# Interactions between Fluorescent Molecules and Plasmonic Nanoparticles: A Super-Resolution Study

by

Bing Fu

**A dissertation submitted in partial fulfillment**
**of the requirements for the degree of**
**Doctor of Philosophy**
**(Chemistry)**
**in the University of Michigan**
**2017**

Doctoral Committee:

Assistant Professor Julie S. Biteen, Chair
Professor Zhan Chen
Associate Professor Stephen S. Maldonado
Associate Professor Vanessa Sih

Bing Fu

bingf@umich.edu

ORCID iD: 0000-0001-9952-2244

# DEDICATION

*This dissertation is dedicated to my family, who always gave me strength and happiness despite the distance; to my friends, who helped me in every way.*

# ACKNOWLEDGMENT

I would like to acknowledge all the support, help and valuable advices I got, both for career and for life, from the people around me. You have made the past five years so rewarding and fun for me.

I would like to first thank my advisor Julie Biteen for her consistent guidance and encouragement in my PhD years. As a young woman who decides to pursue a scientific career, I never realized how important and inspiring it is to have someone you can look up to closely until I joined the lab.You have been my role model since then because of your enthusiasm for science, great dedication for perfection and an optimistic personality. You always provide constructive suggestions when I encounter difficulties in experiments; you also give me full freedom and encouragement to explore challenging problems, which is so valuable for my future career. Thank you for giving me confidence, teaching me how to think about science and making me a better, more dedicated scientist.

Then I would like to thank all my committee members, Zhan Chen, Vanessa Sih, Stephen Maldonado and Julie Biteen. Thank you for offering me valuable advices on pushing my projects to further depth and providing supports for my every progress during the past years.

Also I want to thank all the colleagues in my lab. Thank you, Jessica Flynn, for your patience as a mentor and for being a great friend to share passion for science and happiness in life. Thank you, Beth Haas, for your detailed help ranging from Matlab commands to teaching preparations. Thank you, Esther Wertz, you have shown me the creativity and perseverance a scientist should have. Thank you, Hannah Tuson, for all the time you spent teaching me every biochemistry technique I now have and for being a great climbing buddy. Thank you, Yi Liao and David Rowland, for all your Matlab wisdom and the jokes which made my days, and without you two I wouldn't be able to get the very first car in my life. Thank you, Ben Isaacoff, for so many collaborations we had, for your brilliant ideas on both science and policies and all the insightful discussions we ever had. Thank you, Stephen Lee, for all the fun we had in LNF with those "bunny suits" on. Thank you, Chanrith Siv, for the help with my proteins which sometimes didn't go as expected and for your friendship throughout the years. Thank you, Mou-Chi Cheng, for all the reagents and instruments you always timely provided and the experiences you gave me. I would also like to thank Yilai Li, Josh Karslake and Tiancheng Zuo for being great labmates and adding so much fun for my time in Michigan.

Last but not least, I would like to thank my parents, who always supported me and cheered me up through good and hard times. You encouraged me to pursue my dream but also made me feel absolutely safe when I need it. And Feifan Wang, my fiancé, you are passionate about work, life and me; you are the best friend and partner I could ask for and the past a few years would be so much harder without your love and understanding.

# TABLE OF CONTENTS

# LIST OF FIGURES

# LIST OF APPENDICES

# Abstract

Single-molecule super-resolution imaging techniques play an increasingly important role in studying complex fine structures, dynamics and interactions in nanoscale confined spaces. The resolution is closely related to the photophysical properties of the fluorescent probes used, and it is desirable to enhance the brightness and photostability of various probes applicable to super-resolution imaging, including organic dyes and genetic encodable fluorescent proteins. Noble metal nanoparticles support plasmon resonances that create a very strong, localized electromagnetic field surrounding the surface of the particles. This enhanced field will engineer the decay pathways of nearby fluorescent molecules and potentially increase the fluorescence intensities.

In the present Thesis, I investigate the interactions between fluorescent molecules and gold plasmonic nanoparticles of various structures using three different single-molecule imaging techniques with the overarching goal of understanding different aspects of this phenomenon. Chapter I thoroughly introduces the general principles of single-molecule super-resolution fluorescence microscopy and explains the limitations of dimmer probes. Plasmonic nanoparticles and how they can be used in plasmon-enhanced single-molecule fluorescence microscopy are also introduced. The interactions between the nanoparticles and fluorescent molecules are complicated and it is essential to understand this interaction at the single-particle/single-

molecule level. Open questions including what is the distance-dependence of fluorescence enhancement and how is the dye emission mislocalized by a plasmonic nanoantenna are also introduced here. Gold nanorods (NRs) are good plasmonic substrates for the purpose of fluorescence enhancement as they are biocompatible and tunable in the visible range. The separation distance between the gold NR and the fluorescent molecules, however, will drastically influence the effective enhancement as the electromagnetic field is a very sensitive function of distance.

To explore this distance-dependence, in Chapter II, I use the single-molecule technique of PAINT (Points Accumulation for Imaging in Nanoscale Topography) to image the interactions between single fluorescent molecules and a single gold NR. This work demonstrates the great potential of plasmonic nanoparticles to be used in single-molecule super-resolution imaging and indicates that a spacer layer of optimized thickness (about 10 nm) is necessary for best enhancement. This distance-dependent enhancement effect is generally applicable to different kinds of probes including cyanine dye molecules and fluorescent proteins, and to both polymer and inorganic silica spacers. This optimal thickness provides experimental evidence that fluorescent probes labeling membrane proteins which are naturally located within 20 nm from the outer boundary of cells can be enhanced when coupled to an extracellular nanoparticle substrate. Plasmon-enhanced fluorescence would be a promising new approach for increasing the resolution for cellular imaging, especially for the widely used, but relatively dim, fluorescent proteins.

We would like to understand this distance-dependent fluorescent enhancement in a more deliberately designed structure where the distance between the nanoparticle and the fluorophore is uniform and more precisely controlled. In Chapter III, photoactivatable fluorescent proteins—one of the most popular categories of fluorescent protein probes for single-molecule imaging and tracking—are chemically conjugated to silica shell spacers on the surface of gold nanoparticles, and their plasmon-enhanced fluorescence properties are carefully studied in terms of separation distance by using PALM (Photoactivated Localization Microscopy). This structure completely avoids the ambiguity in distances existing in PAINT experiments and provides direct evidence for distance-dependent fluorescence enhancement.

In addition to fluorescence enhancement, plasmonic nanoparticles also influence other optical properties of nearby fluorescent molecules due to the increased local density of states (LDOS) about a plasmonic nanoantenna, such as the far-field emission positions. Chapter IV describes a recently discovered phenomenon that has been attracting more and more attention in the single-molecule imaging and nanophotonics fields: the far-field emission detected from a fluorescent molecule coupled to a plasmonic nanoparticle, deviates significantly from the actual emitter position. This deviation, which we call fluorescence apparent emission mislocalization, is ubiquitous in various plasmonic nanostructures and different fluorophores. This effect creates an obstacle for studies of nanoparticle/fluorophore interactions, including hot spot mapping, nanostructure morphology reconstruction, and for our purpose, it compromises the accuracy of super-resolution imaging in plasmon-enhanced fluorescence microscopy. Previous studies indicated that the mislocalization can be up to tens of nanometers in magnitude, and in this Chapter, we use a single-molecule study to investigate this effect quantitatively as a function of distance. By developing a new statistical analysis tool, we can resolve the actual emitter positions even from 2D projected images and quantify the mislocalization distance with resolution better than the localization precision.

# CHAPTER I

# Introduction

## 1.1 Single-molecule super-resolution fluorescence microscopy

Optical microscopy is a very powerful technique for observing small objects at the micron- and nanometer scale, and fluorescence microscopy is in particular extensively used for imaging both chemical and biological samples. Due to the Stokes' shift, fluorescence emission occurs at longer wavelengths than fluorescence excitation, so that the excitation and emission can be spectrally separated. Therefore fluorescence microscopy has the advantages of low background, high signal to noise ratio, a wide selection of imaging probes and minimal perturbation to the investigated systems. Though they are able to resolve reasonably fine structures, all optical microscopies, including fluorescence microscopy, have fundamentally limited spatial resolutions due to the wave nature of light. Because of the diffraction of light, the image of even an infinitesimally small point source through an objective is not an infinitesimally small single point; instead this image appears as a diffraction-limited spot and the PSF (Point Spread Function) can be described by an Airy disk function with finite width (Figure 1.1.1 A). [1] This PSF width determines the theoretical resolution as described by the Abbe diffraction limit equation:

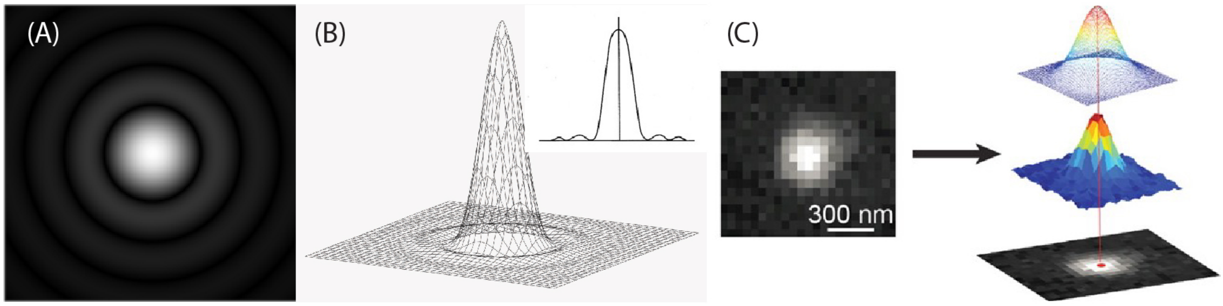

Figure 1.1.1: (A) Image of a point source on the object plane through a lens. (B) The PSF (Point Spread Function) of a point source can be described by an Airy disk function (inset: cross section of the 3D geometry). (C) In usual single-molecule imaging conditions, the PSF can be sufficiently approximated by a 2D Gaussian function. By fitting the single-molecule image to the function, the center position of the diffraction-limited spot is localized with nanometer precision. [2]

$$d = \frac{\lambda}{2NA} \tag{1.1.1}$$

where $d$ is the radius of the diffraction-limited spot, $\lambda$ is the emission wavelength and $NA$ is the numerical aperture of the objective. $NA$ is defined as $nsin\theta$, where $n$ is the refractive index of the media between objective and sample, and $\theta$ is the maximal half-angle of the cone of collected light. Using immersion oil that has high $n$, the $NA$ can be up to 1.4. For fluorescence microscopy, probes in the visible to near-infrared range are used, therefore the resolution in Equation 1.1.1 is about 200 - 300 nm, and any structure smaller than this size can not be resolved directly.

In comparison, Scanning Electron Microscope (SEM), Transmission Electron Microscope (TEM), Scanning Tunneling Microscope (STM), cryo-Electron Microscope (cryo-EM) and other electron-based and near-field scanning probe microscopies have much shorter wavelengths and can achieve resolutions lower than 1 nm. [3] Yet these non-optical approaches usually require sophisticated instruments, complicated sample preparation procedures, ultraclean samples, high vacuum and other conditions that are difficult to attain, which are not ideal in many applications. Fluorescence microscopy has great advantages in studying biological systems due to its low background, easy sample preparation, genetically encodable fluorescent protein probes and the ability to be used *in vivo* without introducing harsh perturbations to the organism. However, given the intrinsic diffraction limit of up to hundreds of nanometers, it is hard to directly uncover subcellular structures such as mitochondria, endoplasmic reticulum and nucleus; or observe the formation of functional protein complexes inside cells. Furthermore, fluorescence microscopy has also seen numerous applications in studying nanoparticle optical properties, catalysis and nanophotonics; [4–8] as in cellular imaging, the diffraction limit prevents any spatial resolution better than a few hundreds of nanometers, thus many localized interactions, chemical reactions are not easily or directly probed with conventional fluorescence imaging.

Fortunately, in the last two decades, researchers have made sub-diffraction resolutions possible by engineering excitation processes, optimizing emission collections and applying novel image analysis algorithms. For example, confocal scanning microscopy excludes the out-of-focus emission light through a pinhole at the confocal plane, [9] and therefore better resolution is achieved. Even more, in Stimulated Emission Depletion (STED) microscopy, [10, 11] an excitation laser is depleted with a second, donut-shaped high power laser, and the molecules inside the region where the depletion power are high enough will be forced to stimulated emission so that fluorescence is suppressed here. Fluorescence will only come from the very center region of the beam and therefore even better resolution than confocal microscopy is achieved. By scanning the STED beam across the whole sample, an entire picture with much higher resolution can be reconstructed.

Furthermore, various single-molecule super-resolution techniques have tremendously contributed to different fields by pushing the resolution even further. The general principle of single-molecule super-resolution techniques (Figure 1.1.1) is to be able to turn on single molecules one at a time so that their PSFs do not overlap, enabling position determination of each molecule sequentially. This can be achieved through several different approaches: 1) Only one labeling molecule is activated at the same time so they can be separated in time and localized individually, either through stochastic blinking (induced by an appropriate buffer, high power laser, or energy transfer fluorophore pairs) or photoactivatable fluorescent proteins, which are only fluorescent when activated by ultra-violet light. Techniques based on this principle include Photoactivated Localization Microscopy (PALM) [12] or Fluorescence Photoactivation Localization Microscopy (fPALM) [13] —photoactivatable fluorescent proteins are the labeling probes, which are only fluorescent when activated by ultra-violet light; Stochastic Optical Reconstruction Microscopy (STORM) [14] —with a pair of dye molecules, donor and acceptor, the molecules can be switched on and off stochastically; Direct Stochastic Optical Reconstruction Microscopy (dSTORM) [15,16] or Ground State Depletion (GSD) Microscopy [17,18]—where molecules are switched to a dark triplet state stochastically either by appropriate buffer or high power laser. 2) Molecules diffusing in solutions will randomly adsorb on a surface and be transiently immobilized. With proper concentrations, the adsorbed molecules are spatially separated and imaged on camera. This technique is very useful in mapping subdiffraction structures and nanoscale hotspots in high throughput. Points Accumulation for Imaging in Nanoscale Topography (PAINT) [19] is based on this principle and many other related techniques are also developed including Quantitative Points Accumulation for Imaging in Nanoscale Topography (qPAINT) [20] and

Universal Points Accumulation for Imaging in Nanoscale Topography (uPAINT) [21].

With the above mentioned techniques, previously overlapping PSFs from multiple emitters can now be imaged individually. As shown in Figure 1.1.1 B, the Airy disk function can be approximated as a 2D Gaussian function for computational simplicity. In single-molecule analysis, the PSF of a single emitter is usually fit to a symmetric 2D Gaussian (Figure 1.1.1 C) and the center of the Gaussian function can be precisely located, theoretically with infinite precision. [22–25] However, in reality, the intensity of each emitter is not infinitely high and various noise sources exist, including background noise, electronic shot noise. The optical objective system also has a limited photon collection efficiency. Considering all the above factors, the experimental two-dimensional localization precision can be calculated as: [25]

$$\Delta x = \sqrt{\frac{s^2 + a^2/12}{N} + \frac{8\pi s^4 b^2}{a^2 N^2}} \tag{1.1.2}$$

where $\Delta x$ is the error in localization, $s$ is the standard deviation of the PSF, which is related to objective $NA$ and emission wavelength, $a$ is the size of the pixel, $N$ is the number of photons detected and $b$ is the background noise. In usual experiment conditions, $a^2/12$ is much smaller than $s^2$, and $N^2$ is a large number, therefore the equation is regularly simplified to the following form:

$$\Delta x \propto \frac{1}{\sqrt{N}} \tag{1.1.3}$$

Many engineering efforts have been put into further increasing the resolution of the super-resolution techniques. To eliminate undesired background fluorescence, Total Internal Reflection Fluorescence (TIRF) microscopy uses evanescent wave excitation, [26–28] which decays exponentially in the direction vertical to the sample surface, to excite only $\sim 100$ nm depth into the sample; similarly, confocal microscopy excludes the emission light not from the focal plane by introducing small pin holes in the emission pathway; [9] light sheet fluorescence microscopy, including Highly Inclined and Laminated Optical (HILO) sheet microscopy, [29] uses a thin sheet of excitation light to minimize the illumination volume and achieves a high signal-to-noise (S/N) ratio as well as fast 3D imaging by optical sectioning. [30] As shown by equation 1.1.3, more collected photons are desirable. Therefore, a two-objective setup around the sample, which is able to collect both the top and bottom half of the emitted photons, theoretically increases the resolution by a factor of $\frac{1}{\sqrt{2}}$, as implemented by 4pi microscopy. [31–33]

Besides improving resolution, other imaging functionalities are also being incorporated into these techniques. One important aspect is that 3D imaging, which enables super-resolution localizations in $z$-dimension, is developing rapidly and contributing new science to different areas. [34]. For 3D imaging, techniques relating to astigmatism, [35] double-helix PSF [36] or iPALM [37] have been able to image super-resolved structures in 3D in real time or in very thick cell samples. On the other hand, camera technology also contributes to improving the capability of single-molecule imaging, for example, the recent complementary metal-oxide semiconductor (CMOS) camera allows a larger field of view and faster image acquisition than EMCCD camera. [38]

Because of the extensive progress in super-resolution imaging techniques, nowadays it is possible to use these tools to explore subdiffraction-limited structures with tens of nanometers resolution. For example, as shown in Figure 1.1.2, important information about sub-

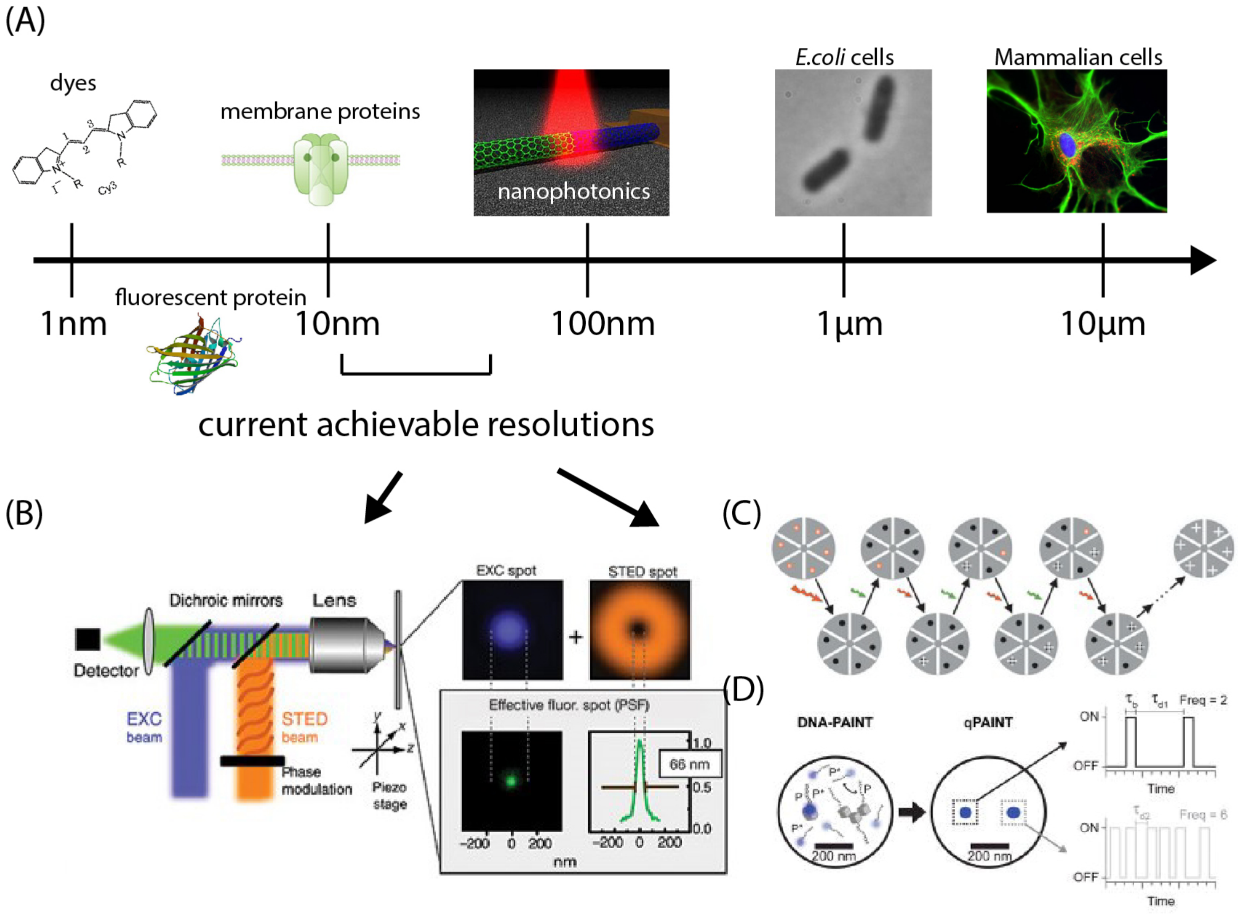

Figure 1.1.2: (A) Length scales of different structures widely investigated and current resolutions of single-molecule super-resolution imaging techniques. (B) Principle of Stimulated Emission Depletion (STED) microscopy. [39] (C) Principle of Stochastic Optical Reconstruction Microscopy (STORM). [14] (D) Quantitative Points Accumulation for Imaging in Nanoscale Topography (qPAINT) technique. [20]

cellular structures, such as membrane composition and protein dynamics and functionalities, [40–42] as well as information about interesting interactions between light and top-down/bottom-up synthesized nanostructures can be revealed, which are hidden behind the diffraction limit.

In our lab, a traditional single-molecule epi-fluorescence optical setup (Figure 1.1.3) has been used to solve various mysteries in the nanoscale regime at the single molecule level, including protein movements in bacterial cells, [42–44] dye molecule behavior in porous metal-organic framework materials [45] and interactions between single molecules and plasmonic nanoparticles, [46–49] which will be the focus of this thesis. Here, an excitation laser is focused at the back of an objective to excite samples on a substrate; emission light collected through the same objective are separated from excitation light by dichroic mirrors and emission filters. An EMCCD (Electron multiplying charge coupled device) camera detects the fluorescence from single molecules; these images can be further analyzed using customized Matlab algorithms. A 406 nm activation pulse is used in combination with the excitation laser to activate photoactivatable fluorophores, such as PAmCherry, PAGFP, etc. Other functionalities including dark-field scattering spectroscopy, fluorescence spectroscopy, and 3D imaging can also be readily incorporated into this custom-built setup; for instance, here we use a cylindrical lens to resolve the axial position of single fluorescent emitters.

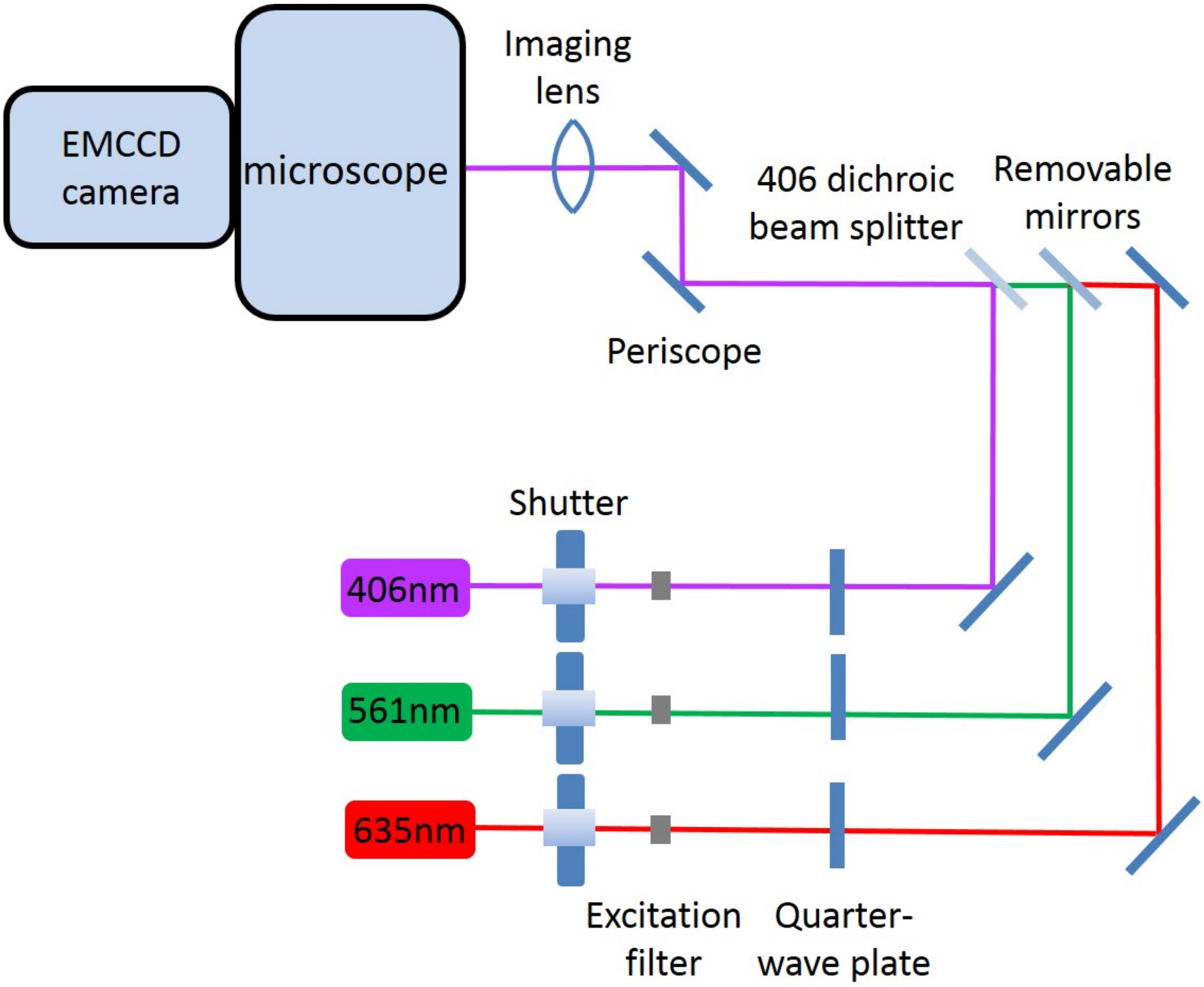

Figure 1.1.3: Optical setup for epi-fluorescence imaging. Linearly polarized laser beams (cleaned up by excitation filters) of different wavelengths are converted to circularly polarized by quarter-wave plates. The laser is focused at the back of the objective and after the objective, the collimated beam excites the sample on the microscope stage. On the emission side, the longer-wavelength fluorescence signal is separated from excitation light by long-pass dichroic filter and emission filter, and detected on an EMCCD camera. A cylindrical lens can be incorporated in the emission pathway if 3D imaging is needed.

## 1.2 Fluorescent probes for single-molecule super-resolution imaging

Based on the intended purposes, there are numerous kinds of fluorescent probes available in single-molecule imaging. The most popular categories include: 1) organic dye molecules, such as Rhodamine dyes, cyanine dyes, Alexa dyes, and Atto dyes. They are mostly small molecules with conjugated ring systems (Figure 1.2.1 A) whose emission wavelengths span from 400 nm to 800 nm. These dye molecules are usually relatively bright, having fast radiative decay rates, high extinction coefficients and quantum yields, [50] and they are widely used for both probing chemical reactions and labeling biological samples. [4] One disadvantage of fluorescent dyes is that they have to be chemically linked to the target, which commonly requires extra steps of reactions and tedious washing procedures. High labeling yields may not be achievable as a result. 2) Inorganic quantum dots (QDs, Figure 1.2.1 B). [51, 52] QDs are small ($< 5$ nm), very bright nanocrystals which usually have high quantum yield (up to 90%) [53, 54]. Their wavelengths are readily tunable by changing the size and element composition (or through doping) which makes them good candidates for multicolor imaging. However, QDs need surfactant molecules on the surface to be stable in the media, making them much bulkier in size, and some chemical elements like cadmium in QDs are toxic to cells and this limits their applications in living systems. [55, 56] Selective labeling of QDs to a specific target is another issue to consider. [57] 3) Fluorescent proteins (FPs, Figure 1.2.1 C). These are cylinder-shaped proteins about 2 - 4 nm in size, which consist of a chromophore in the center of a $\beta$ barrel structure. [58] FPs emit in a wide wavelength range from 450 nm (blue FPs) to 650 nm (red FPs) with more and more new FPs still being developed and their optical properties being optimized and engineered. [59]

Though usually relatively dimmer than dye molecules or QDs, the unique advantage of FPs is that they can be genetically encoded to the target protein makes the labeling procedure easier and more quantified. FPs also avoid the long, floppy linkers sometimes necessary for chemical linkage. Even though the influence of FP labels on biological processes is not fully understood, [60] it is believed that they are more biocompatible and rarely cause photodynamic toxicity compared to organic dyes. [59, 61] Therefore, FPs play an important role in biological fluorescence imaging, and pushing their resolution with single-molecule imaging has great significance in solving many currently unanswered questions.

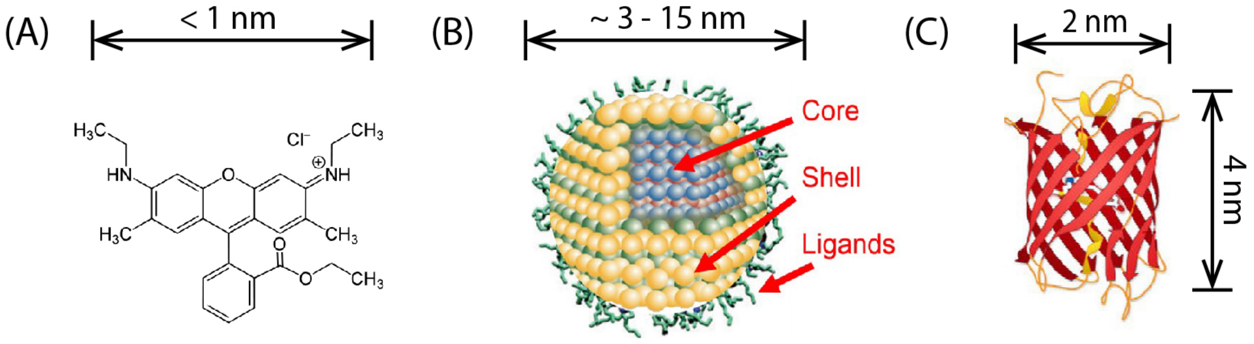

Figure 1.2.1: (A) Rhodamine 6G molecule structure. (B) Illustration of QDs (Quantum Dots) structure. (C) mCherry fluorescent protein crystal structure. [62]

As shown by equation 1.1.3, the resolution is inversely proportional to the total detected photon number, and a brighter fluorophore is beneficial for obtaining a better resolution. Different approaches have been investigated to solve this challenge. Various organic dye molecules with optimized optical properties have been synthesized; [63, 64] adjusting the environment surrounding the fluorescent probes may potentially increase the photon yield—example, researchers found that a heavy water environment led to the FPs probes to be 1.5-fold brighter; [65] reductive caging helps to create ultrabright photoactivatable fluorophore. [66] On the other hand, plasmonic metal nanostructures engineer the optical properties of nearby fluorophores and coupling to these nanoparticles is an easy, efficient and versatile method to tackle this problem, which is the main focus of the research presented in this Thesis.

## 1.3 Plasmonic nanoparticles and LSPR

Noble metal nanoparticles, such as Au, Ag, and Pt, as well as some other materials including Al and Ti, have natural plasmon resonances and when the excitation light wavelength matches the natural plasmon frequency, a collective oscillation of surface electrons is generated, which is called localized surface plasmon resonance (LSPR, Figure 1.3.1 A). [67] This creates a very localized, high density electromagnetic field near the surface of the nanoparticle, and it decays rapidly with distance from the surface within 100 nm (Figure 1.3.1 B). [46] Due to the enhanced electromagnetic field, excited electron decay pathways of molecules located within this field will be influenced significantly, and this coupling leads to many plasmon-enhanced spectroscopies.

Plasmonic nanostructures of all kinds of materials and geometries have been constructed for different purposes, using both top-down and bottom-up methods. For example, electron-beam lithography has been extensively used to design customized nanostructures of Au, Ag, Al and other materials, for use as waveguides, [68] high quality optical pixels, [69], metasurfaces applications [70, 71] and localized imaging and sensing, [72, 73] to name a few. In comparison, chemically synthesized and assembled bottom-up colloidal plasmonic particles have the advantages of high throughput, capability of diverse surface modifications and conjugation, wide selection and easy control of material compositions, and more tunability in 3D geometry, but these nanoparticles have the disadvantage that their assemblies are not as

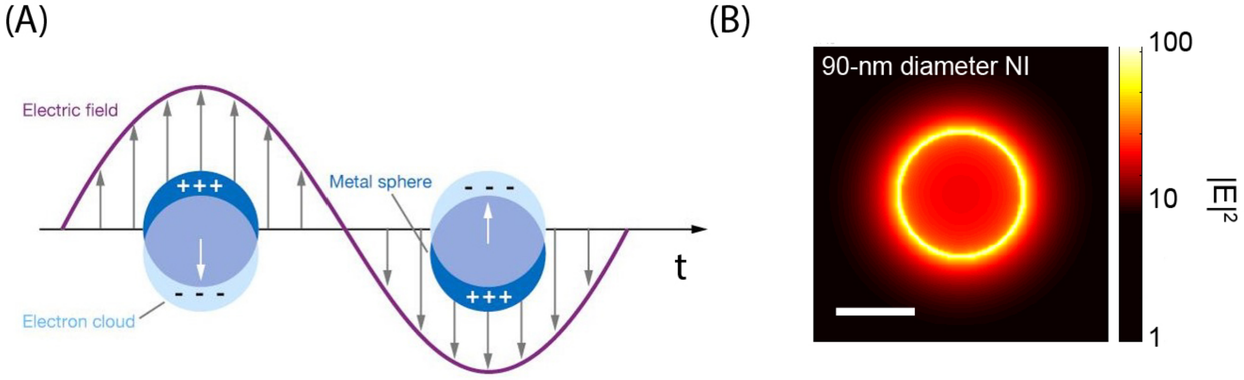

Figure 1.3.1: (A) Localized surface plasmon resonance (LSPR) of nanoparticles, adapted from [67]. Upon excited by laser light of a certain frequency, collective surface electron oscillation (white arrow) generates a strong, localized electromagnetic field (purple line) near the nanoparticle surface. (B) FDTD (Finite-difference time-domain) calculation of local field intensity at 640 nm around a 90-nm diameter gold nanoisland excited by a plane wave. Scale bar: 50 nm. [46] The field intensity drops rapidly away from the edge of the nanoisland.

precisely controlled in size and shape therefore bottom-up structures are more heterogeneous than those made by the lithography approach. Nevertheless, colloidal plasmonic nanoparticles, such as nanospheres, nanorods, nanowires, nanocubes or more complicated structures of gold, silver, aluminum and other materials [74–78] are widely used in plasmon-enhanced spectroscopies. Other techniques such as nanosphere lithography combine the two methods and gain higher homogeneity as well as high throughput. [79, 80]

## 1.4 Plasmon-enhanced fluorescence: applications and challenges

Many applications are based on LSPR of plasmonic nanoparticles, including Surface Enhanced Raman Spectroscopy (SERS), [83] enhanced photon absorption for solar cell light harvesting [84–86] and also enhanced fluorescence. [87–89] When a fluorescent molecule is ex-

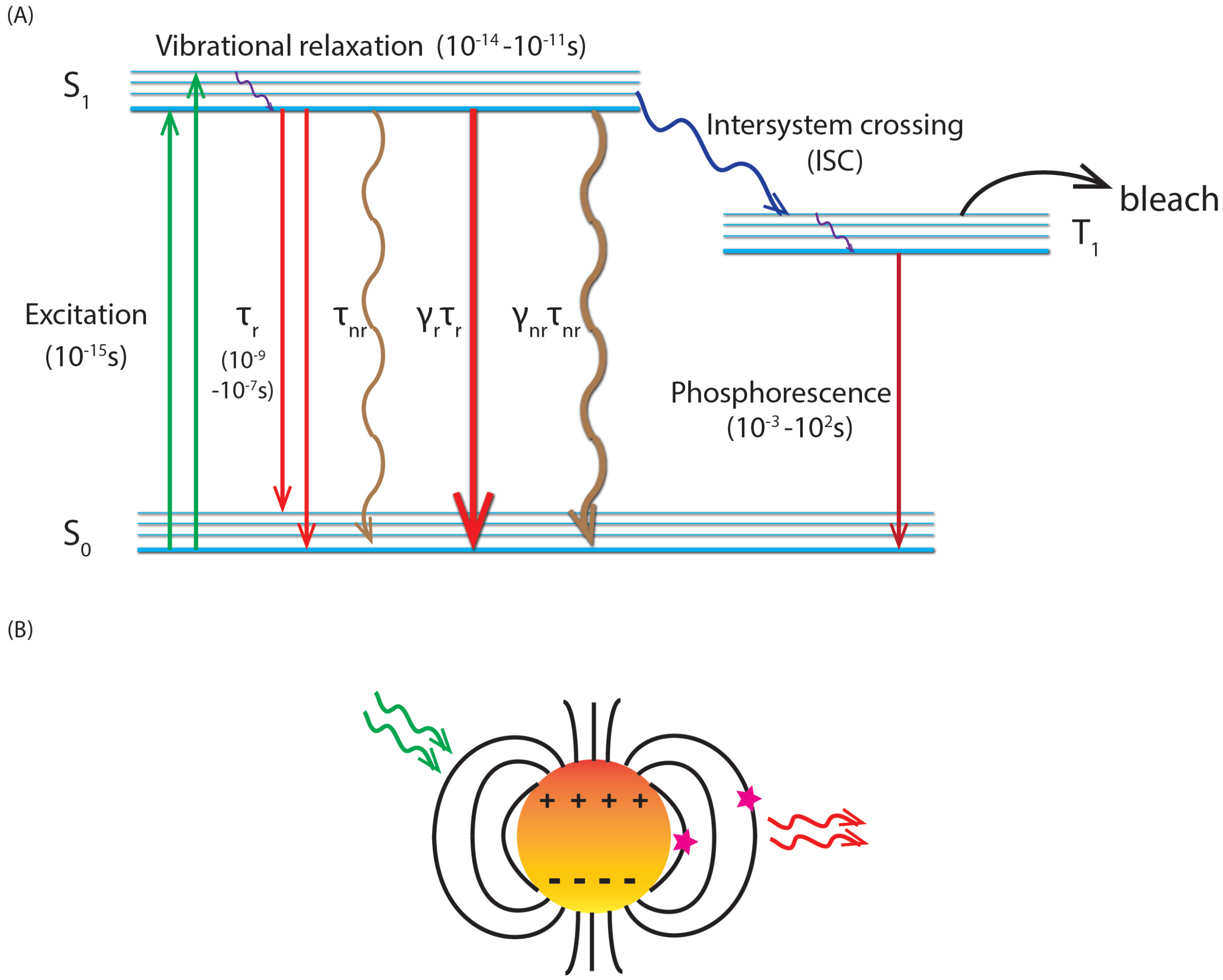

Figure 1.4.1: (A) Jablonski diagram of the electronic states of a fluorescent molecule. Different decay pathways and the corresponding decay rates are labeled as described in the text. [81] (B) Resonant laser light (green) generates an LSPR on a metal nanoparticle and a very localized, enhanced electromagnetic field is produced near the surface, figure adapted from [82]. Fluorescent molecules (pink stars) located adjacently are influenced by the enhanced field as a function of distance from the nanoparticle.

cited by a laser light (green line in Figure 1.4.1), it can be excited into any excited electronic states and based on Kasha's rule, it will quickly relax to the lowest electronic state ($S_1$) and then vibrationally relaxes to the lowest vibration state (purple line), after which it can decay in many different pathways. [81] It can decay radiatively to the ground state ($S_0$, red line) by emitting a photon, which corresponds to fluorescence; based on Franck-Condon principle, fluorescence emission always has longer wavelength than the excitation, which enables it to be easily separated in wavelength. The excited molecule can also decay non-radiatively through internal conversion (IC, brown line)—energy converted to heat, energy transfer such as FRET (Förster resonance energy transfer), or undergo intersystem crossing (blue line)to an triplet state ($T_1$), during which the spin state of the molecule changes from singlet to triplet. From the excited triplet state, the molecule can either decay radiatively to ground state (phosphorescence, dark red line) or react with molecules in the environment, which causes permanent structural modification and as a result the molecule is irreversibly photobleached (black line). Once the molecule is back in the ground state, it can be excited again and the process can repeat thousands of cycles before the molecule is photobleached and loses the ability to fluoresce. [81] All the processes have different decay rates, as indicated in Figure 1.4.1, and the triplet state has much longer lifetime than the singlet state and therefore electrons may be trapped in the dark triplet state for a relatively long period. This long-lived dark state contributes to an important property of fluorescent molecule, blinking, which is disadvantage for continuous tracking of a target but also beneficial for some super-resolution methods such as STORM and dSTORM. The fluorescence quantum yield is related to both the radiative and non-radiative decay rates:

$$\Phi = \frac{\tau_r}{\tau_r + \tau_{nr}} \tag{1.4.1}$$

where $\Phi$ is the quantum yield, $\tau_r$ is the radiative decay rate, and $\tau_{nr}$ is the non-radiative decay rate. By engineering the decay rates, optimized optical properties of fluorophores, i.e. higher photostability, prolonged fluorescence emission, higher fluorescence intensity and total emitted photons, or suppressed or deliberately introduced blinking based on the applications, can be realized. For example, oxygen scavenging systems in imaging buffer can help to capture $O_2$ molecules, which are responsible for bleaching and hence this buffer increase the duration time of fluorescence. Furthermore, triplet state quenchers ($\beta$-mercaptoethanol: BME, mercaptoethylamine: MEA, etc.) which deplete the triplet state can suppress millisecond blinking. [90, 91]

The enhanced electromagnetic field due to the LSPR of plasmonic nanoparticles increases both the radiative and non-radiative decay rate of an excited fluorophore, as shown in the following equation: [88, 92]

$$\Phi = \frac{\gamma_r \tau_r}{\gamma_r \tau_r + \gamma_{nr} \tau_{nr}} \tag{1.4.2}$$

where $\tau_r$ is the radiative decay rate, $\tau_{nr}$ is the non-radiative decay rate, and $\gamma_r$ and $\gamma_{nr}$ are the enhancement factors because of the plasmon-enhanced field for the two decay rates, respectively. The intersystem crossing probability is very low (involves forbidden spin transition) and is assumed to be unaffected by the enhanced field. Therefore the effective influence of a plasmonic nanoparticle on fluorescence is in how it affects the competition between the radiative and non-radiative decay rates. The net enhancement is closely dependent on the intensity of the electromagnetic field, which changes rapidly as a function of distance from the plasmonic nanoparticle surface. Furthermore, the two decay rates are differently influenced by the electromagnetic field—the non-radiative rate is more sensitive to distance than the radiative decay—as a result, the final effect is not purely monotonic and the fluorescence enhancement is a quite complicated function of distance.

Since the electromagnetic (EM) field can be enhanced hundreds of thousands of fold when the nanoparticle is ideally designed, up to thousands of fold fluorescence enhancement has been reported. Fluorescence of a weak emitter, crystal violate can be enhanced more than 1000-fold near colloidal gold nanorod in solution [93] and Cy5 molecules can be enhanced up to 30,000-fold in silver cubes/Au film gap hotspot. [94] This significant enhancement has been widely used in ultrasensitive detection, such as performing ultra low concentration biomolecule analysis, [95] and measuring dynamics and structure changing of protein/DNA molecules based on fluorescence detection. [96] We aim to use this enhancement in single-molecule super-resolution imaging, incorporating designed plasmonic substrates for imaging single molecule with higher resolution. As discussed above, unlike SERS, where the signal is best enhanced when the probe is located as close to the metal surface as possible, fluorescence enhancement has a more complicated distance dependence. Previous studies about the distance-dependence fluorescence enhancement are mostly done in bulk, either in solution or on a dense film, where heterogeneous information is hidden. As we intend to apply plasmonic enhancement to single-molecule applications, it is important for us to fully investigate and understand the interaction between only one molecule and one plasmonic nanoparticle, thus uncovering the heterogeneity. Furthermore, most previous work focuses on the enhancement of organic dye molecules and only recently have studies been done on plasmon-enhanced fluorescent proteins, [47, 48] which are very important in biological imaging. In this thesis, both dye molecules and fluorescent proteins will be studied, expanding the scope for enhanced fluorescence imaging. This distance-dependent study will be important for designing optimal plasmonic substrate with an ideal spacer layer thickness for best fluorescence enhancement.

On the other hand, interactions between fluorescent molecules and plasmonic nanoparticles are complicated. Not only is the intensity of the fluorophore changed, but other optical properties like emission position, polarization, and PSF shape, are also affected by coupling to a nanoparticle. Particularly, researchers have recently realized that, the super-resolved emission position of a single emitter is significantly influenced by the presence of a plasmonic nanoparticle, a phenomenon we call emission mislocalization. [46, 49, 97–100] As discussed above, upon excitation, LSPR created on plasmonic nanoparticles generates a strong, localized electromagnetic field near the surface. With the plasmonic nanoparticle acting as a nano-antenna, the local density of state (LDOS, states that can be occupied by a photon) near the nanoparticle is significantly increased. Therefore, it is not surprising that the behavior of the emitted photons from a nearby fluorescent molecule will be affected. Specifically, the super-resolved apparent position of the molecule is shifted toward the nanoparticle, where high LDOS exists. This position distortion can be up to tens of nanometers which is significant compared to the resolution of super-resolution techniques. Yet this effect is only visible using single-molecule super-resolution techniques and have been hidden in many previous ensemble experiments. It is crucial for us to explore this phenomenon in depth to gain more insights about the interaction between nanoparticles and fluorescent molecules, and also to develop better single-molecule localization analysis for plasmon-enhanced fluorescence imaging, where actual molecule positions can be recovered.

## 1.5 Thesis outline

In Chapter II, gold nanorods are explored as a potential substrate for single-molecule super-resolution imaging due to its resonance tunability, facile synthesis and good biocompatibility. PAINT experiments are conducted to investigate the interactions between single Cy3.5 dye molecules, mCherry FP molecules and single gold nanorods, with an emphasis on fluorescence enhancement. We carefully tune the thickness of the nanoscale spacer surrounding the gold nanorod, which separates the nanoparticle from the fluorophore by a certain distance, and we observe the enhancement change as a function of the spacer thickness. We find that plasmonic enhancement is generalizable for different kinds of fluorescent molecules—both dye and fluorescent proteins—and both fluorophore types exhibit a non-monotonic trend of enhancement with the optical spacer thickness being about 10 nm for both. This study shows the capability of single-molecule techniques, where information from each molecule can be obtained to yield more complete statistics than just the ensemble average. This result dictates the ideal separation distance for plasmon-enhanced fluorescence, indicating that enhanced membrane protein imaging [101] is promising since the cell membrane naturally positions the fluorophores about 10 nm away if the cells are immobilized on a plasmonic substrate.

In Chapter III, the focus is on the photoactivatable fluorescent proteins, PAmCherry and PAGFP, which are important in PALM imaging and single-molecule tracking experiments. To explore the distance-dependence in a more precise way, silica-shell coated gold nanospheres are synthesized and further functionalized with biotin end group. In order to bind the fluorescent proteins under study, a FP-streptavidin fusion protein is constructed through cloning, protein expression and purification in *E.coli* cells. In the end, the FPs are tightly linked to the nanoparticle surface, separated by the silica shell. In PALM experiments, by tuning the silica shell thickness, we observed 2-fold enhancement for 20 nm spacer and no enhancement for 80 nm spacer. The experiments in Chapter III more carefully quantify the maximal enhancement distance and also prove that plasmon-enhanced fluorescence is also applicable in photoactivatable fluorescent proteins.

In Chapter IV, a different aspect of the nanoparticle/fluorescent molecule interaction is explored, namely the emission mislocalization. Dye molecules near a spherical gold nanoparticles are super-localized one by one, and their apparent emission positions—which differ on the nanometer scale from the actual dye positions due to the coupling—are uncovered through a new analysis algorithm. By comparing for each dye the apparent emission positions with the actual physical positions, the mislocalization effect due the increased local density of states is carefully studied as a function of distance. We find that mislocalization up to 60 nm happens at different separation distances from 10 nm to 30 nm, and we find that the mislocalization is also distance dependent: smaller separation distances lead to stronger coupling and larger mislocalizations. Electromagnetic simulations are also done to support and provide theoretical explanations for the experimental results. Chapter V summarizes all the above research about the distance-dependent interactions between plasmonic nanoparticles and fluorescent molecules, and future directions and questions in this field are also discussed.

# CHAPTER II

# Distance-dependent fluorescence enhancement of single molecules coupled to gold NR

*The work presented in this Chapter was published in the following paper:*

Bing Fu, Jessica D. Flynn, Benjamin P. Isaacoff, David J. Rowland, and Julie S. Biteen*, "Super-Resolving the Distance-Dependent Plasmon-Enhanced Fluorescence of Single Dye and Fluorescent Protein Molecules", *J. Phys. Chem. C.*, **2015**, *119*, 19350-19358

As co-authors, JDF helped to design the experiments; BPI conducted the Finite Difference Time Domain simulations; DJR established the geometric framework for simulating the substrate three-dimensional shape. All authors participated in the discussion and revision of the manuscript.

## 2.1 Abstract

Coupling to metal nanoparticles can increase the fluorescence intensity and photostability of fluorescent probes, and this plasmon-enhanced fluorescence is particularly promising for the dimmer fluorescent proteins common in biological imaging. Here, we measure the intensity

distribution of single Cy3.5 dye molecules and mCherry fluorescent proteins one at a time as they adsorb on a conformal surface 4.8 - 61.0 nm thick over a gold nanorod (NR). The emission intensities for both types of fluorophores depend non-monotonically on the spacer thickness, and an optimal spacer thickness of ∼10 nm is observed for both fluorophores using two different spacer layer materials. Emission from fluorophores coupled to metal nanoparticles is affected by two competing processes: an enhanced spontaneous decay rate and quenching via non-radiative antenna modes. After averaging over a conformal surface, the product of the simulated enhanced local electric field intensity and the quantum efficiency quenching reproduces the experimental 10-nm ideal spacer thickness. Overall, up to a 3.4-fold average enhancement in fluorescence intensity was achieved despite the simple geometry, based on bio-compatible, tunable and economic colloidal gold NRs. This study of the distance dependence of single-molecule plasmon-enhanced fluorescence shows promise for super-resolving cellular membrane proteins naturally positioned above an extracellular substrate.

## 2.2 Introduction and motivation

Fluorescence microscopy is a ubiquitous and impactful tool in biology, [102] and single-molecule detection enables super-resolution fluorescence imaging. [22] This collection of sensitive and non-invasive techniques has overcome the diffraction limit of traditional light microscopy to inform on molecular assemblies, dynamics and interactions in real time and on the nanometer scale, even in live cells. [2,103] In a typical single-molecule tracking, Photoactivation Localization Microscopy (PALM), or Stochastic Optical Reconstruction Microscopy (STORM) experiment, molecules labeled with an organic dye or fluorescent protein (FP) are imaged one at a time. [2, 12, 14] Fitting the diffraction-limited emission profile (point spread function) of each isolated molecule enables super-localization of that label with a precision much higher than the diffraction limit of light. Though the localization precision of this method can theoretically be as small as the size of the molecule itself, [104] the label brightness typically dictates the upper bound. Because the precision of single-molecule microscopy increases with the square root of the number of detected photons, [25] improving the brightness of fluorescent probes is a highly desirable goal. Additionally, our ability to detect rare events or low copy number biomolecules in cells depends on the experimental signal-to-noise, which improves as the label brightness increases relative to the background. Coupling to metal nanoparticles has been shown to enhance the brightness of nearby fluorescent dyes [94, 105] and FPs, [47] and here we investigate the distance-dependence of this plasmonic enhancement by a direct measurement of the relevant quantity: the single-molecule fluorescence intensity of individual dyes and FPs.

Upon resonant excitation, a collective oscillation of electrons on the surface of noble metal nanostructures will establish a local surface plasmon resonance (LSPR), which generates a strong, localized electric field near the nanostructure surface. This enhanced electromagnetic field can improve Raman and fluorescence signals by increasing the local density of photonic states. [83,106,107] The LSPR frequency and strength depends on the nanoparticle material and geometry, [67,108] and improved spectroscopy has been demonstrated across the visible spectrum based on a variety of gold, silver, platinum and aluminum nanostructures and thermally evaporated nanostructured gold and silver films. [93,105,109–113] Though the LSPR properties can be well understood and modeled for arbitrary geometries with electromagnetic simulations, the fluorescence of single fluorescent probes near plasmonic nanostructures is still not fully characterized. Most previous studies have explored plasmon-enhanced fluorescence in dense films or in high-concentration solutions, where ensemble measurements mask heterogeneities. [114] To understand the potential for plasmon-enhanced super-resolution imaging, it is therefore critical to measure plasmon-enhanced fluorescence directly using the same single-molecule assay for which it is intended.

Enhanced fluorescence has been observed from single dye molecules, [46, 109, 113] and we have recently demonstrated enhanced fluorescence brightness and photostability from isolated intrinsically fluorescent proteins, with important implications for increased sensitivity, tracking and resolution in biological imaging. Importantly, this enhancement was realized based on coupling to bio-compatible, nontoxic gold nanoparticles. [115, 116] To implement plasmon-enhanced single-molecule cellular imaging using extracellular nanoparticles to maintain the benefits of non-invasive fluorescence microscopy, [117] some separation between the nanoparticle and the fluorescent label will be unavoidable. However, the fluorescent emission in a coupled system depends strongly on the separation distance because the coupling between a fluorescent emitter (fluorophore) and a metal particle gives rise to two separation-distance-dependent effects: enhanced spontaneous decay rate due to local field enhancement and quenching via non-radiative antenna modes. [118–120]

Here, we directly measure the effect of spacer layer thickness on the emission intensity of single organic dye and FP molecules separated from colloidal gold nanorods by bio-compatible polyelectrolyte (PE) or silica spacer layers. Importantly, while quenching and enhancement have been reported by different groups under various experimental conditions, [121–124] very few distance-resolved studies have observed plasmon-enhanced emission from single molecules. [94, 125, 126] In this chapter, we measure the coupling between single fluorophores and metal nanorods as a function of spacer thickness in a practical geometry that can be directly implemented for cellular imaging. [2, 117] Our approach accounts for the emission from each molecule in a distribution of all accessible molecular orientations, positions, and separations. We show that single-molecule plasmon-enhanced fluorescence is a robust effect that can be attained for traditional fluorescent labels with quantum yields of 20%. In particular, we apply plasmon-enhanced fluorescence to a typical red FP, mCherry (average 3.4-fold brightness enhancement) and for a relatively bright cyanine dye, Cy3.5 (average 1.5-fold brightness enhancement), and we observe that the competition between quenching at short distances and distance-dependent enhancement gives rise to an optimal spacer thickness of approximately 10 nm for both of these very different probes. Furthermore, we understand the mechanism that gives rise to this observed fluorescence enhancement in the context of finite difference time domain (FDTD) electromagnetic simulations of the real sample geometries. Overall, we achieve enhanced fluorescence from single-molecule emitters using a simple, bio-compatible platform.

## 2.3 Experimental methods

### 2.3.1 Substrate preparation and characterization

Glass microscope coverslips were cleaned in an $O_2$ plasma etcher at 200 mTorr for 10 min (PE-50, Plasma Etch Inc.). Polyelectrolyte (PE) solutions of poly(sodium 4-styrene) (PSS, Sigma-Aldrich, average MW $\sim$ 70,000, 30 wt% in $H_2O$) and poly-(diallyldimethylammonium chloride) (PDADMAC, Sigma-Aldrich, average MW $\sim$ 200,000 - 350,000, 20 wt% in $H_2O$) were diluted in phosphate buffered saline (PBS) to 20 mM. 50-nm diameter gold nanorods (A12-50-600 NRs) were purchased from Nanopartz Inc. (Loveland, CO) and used as received. NR substrates were prepared by a spin-assisted layer-by-layer technique: [127] NRs were immobilized to the coverslip surface by films of positively charged PDADMAC and negatively charged PSS. First, 20 mM PDADMAC solution was spun onto the cleaned coverslips (300 $\mu$L, 15 s, 4000 rpm) to form a base layer and then washed three times with DDI water. A mixture of NRs and 20 mM PSS (100 $\mu$L of NRs and 200 $\mu$L of PSS; $1.5 \times 10^{10}$ NRs/mL) was then spun onto the PDADMAC-coated coverslip (15 s, 4000 rpm), followed by three DDI water washes. This process produced a sparse distribution of NRs immobilized in PSS on the PDADMAC base layer. [47] Additional spacer thicknesses were formed from 1 - 8 alternating layers of 300 $\mu$L PSS and 300 $\mu$L PDADMAC spin coated one at a time on top of the first two layers (Figure 2.4.1 C). Alternatively, a silica spacer layer was sputtered on top of the NRs immobilized in PSS (Lab 18-1, Kurt J. Lesker).

To study distance-dependence, we need to make sure the spin coated polymers and the sputtered silica indeed formed nanometer thick layers and also were able to be controlled easily (by tuning the number of deposited layers or controlling the sputtering time). To confirm, PE and silica spacer layer thicknesses were determined by spectral ellipsometry (Woollam M-2000DI) as described below (Figure 2.4.2). In all experiments, the spacer layer thickness was considered to be the sum of the cetrimonium bromide (CTAB) ligand molecules on the NR surface (thickness: 2.9 nm), [128] the thickness of the immobilizing PSS layer (1.9 nm), and the thickness of any additional PE layers (2.6 nm - 39.0 nm) or of the sputtered silica (4.7 nm - 56.2 nm). Specifically, the measurements were done by variable angle spectral ellipsometry at 55°, 65° and 75° of samples similar to those prepared on glass coverslips for microscopy experiments, but prepared on silicon wafers and without NRs (Figure 2.4.2). Silicon wafers were etched three times in piranha solution (3:1 concentrated sulfuric acid to 30% hydrogen peroxide) and immersed in 4.9 % hydrofluoric acid aqueous solution for 10 min, followed by an $O_2$ plasma etch at 200 mTorr for 10 min (PE-50, Plasma Etch Inc.)

to create a reliable surface oxide. The PE layer thicknesses were determined by measuring alternating PDADMAC and PSS layers that were spin coated (300 $\mu$L, 15 s, 4000 rpm) directly onto the cleaned and oxidized silicon. The silica spacer thickness was calibrated by sputtering $SiO_2$ onto the cleaned and oxidized silicon (Lab 18-1, Kurt J. Lesker). Because the optical properties of PDADMAC and PSS are very similar, both the alternating PE layer samples and the sputtered silica samples were treated as a single, continuous layer.

### 2.3.2 Dark-field scattering spectroscopy

NRs were immobilized in PSS on PDADMAC-coated glass coverslips as described above, with no additional spacer layers. These NR substrates were immersed in water and covered by a second clean microscope slide. A broadband halogen white light source excited the sample through a dark-field oil-immersion condenser, and scattered light was collected in an Olympus IX71 inverted microscope equipped with a dark-field oil-immersion objective (NA = 0.6). The diffraction-limited image of a single NR was aligned to the entrance slit of an imaging spectrograph (Acton 2300, Princeton Instruments), and spectral data were collected on an EMCCD (2 s integration time; Andor iXon). Background spectra collected from nearby positions with no NR on the spectrograph entrance slit were subtracted from measured spectra, and all data were divided by the broadband spectrum of the halogen light source and any additional neutral density filters to correct for the system spectral efficiency. Dark-field scattering spectra were also obtained for individual NRs immobilized in PSS on PDADMAC-coated coverslips coated with 4 additional PE layers, as well as NRs spin cast directly from suspension with no PE (Figure 2.3.1).

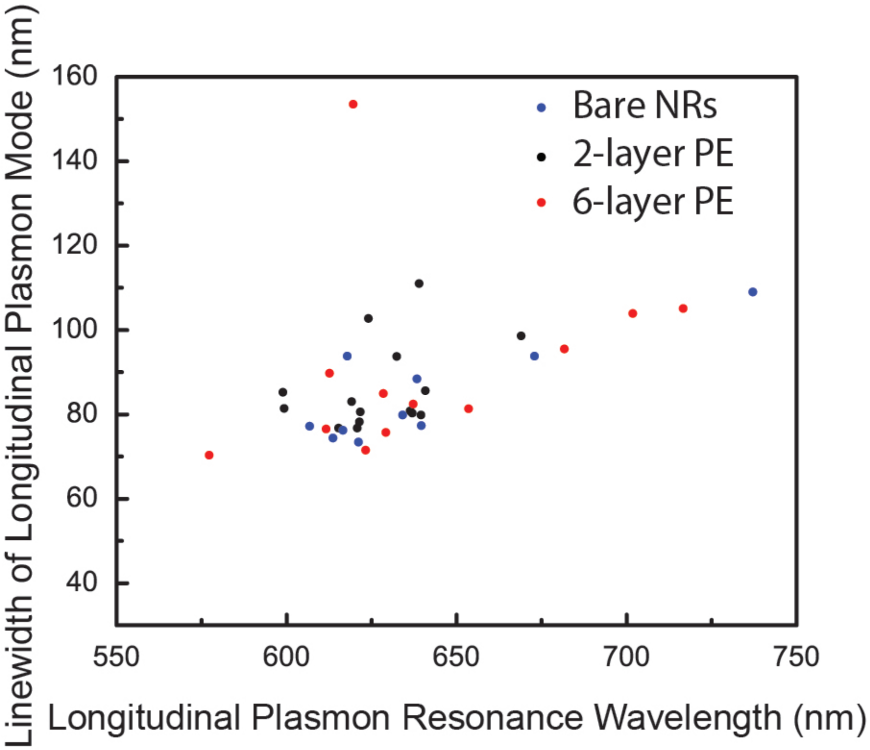

Figure 2.3.1: Linewidths of the longitudinal plasmon mode for each gold NR single-particle dark-field scattering spectrum, showing no significant correlation between PE layer thickness and linewidth. The scattering spectra of 15 gold NRs with 2 layers of PE, 12 gold NRs with 6 layers of PE and 10 bare immobilized gold NRs were measured here. Average linewidths: bare gold NRs: 84.3 ± 11.6 nm; 2 - layer PE: 86.3 ± 10.4 nm; 6 - layer PE: 90.9 ± 22.9 nm.

### 2.3.3 Single-molecule epifluorescnece microscopy and PAINT experiments

Wide-field epifluorescence microscopy was performed on spacer-coated gold NR substrates imaged with a 100× 1.40 NA oil-immersion objective in an Olympus IX71 inverted microscope (Figure 2.4.1 A). To perform PAINT (Points Accumulation for Imaging in Nanoscale Topography) experiments, 75 - 100 $\mu$L of 7 nM mCherry FP (BioVision, Inc.) in PBS or 22

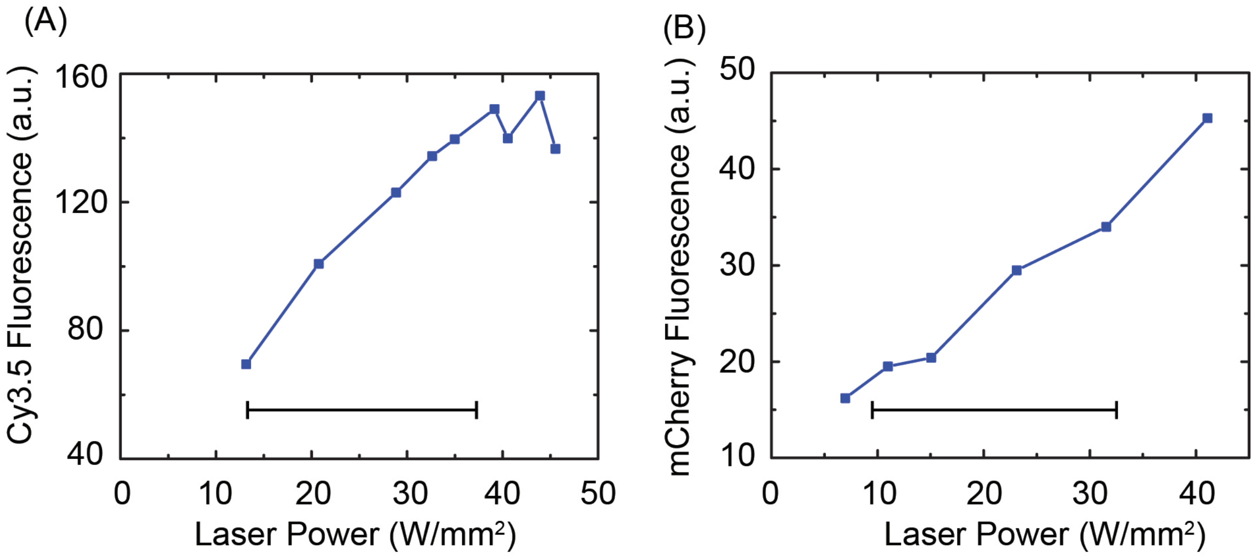

Figure 2.3.2: Power-dependent fluorescence intensity of (A) Cy3.5 and (B) mCherry. Laser wavelength: 561 nm. All measurements were done on single adsorbed fluorophore molecules as described in the main text. The inset black lines indicate the range of laser powers used in the experiments: all laser powers were in the non-saturating regime.

nM Cy3.5 dye (Lumiprobe Corporation) in water was placed on top of the NR substrates in a rubber O-ring that had been cleaned by sonication in acetone (Figure 2.4.1 A). Single mCherry or Cy3.5 molecules were excited with circularly polarized 561 nm laser light (Coherent Sapphire 561-50 and Tower Optical .250-556 quarter waveplate). Excitation intensities were 9.8 - 37.6 W/mm$^2$ (Figure 2.3.2). Fluorescence emission was filtered appropriately (Semrock Di01-R561/BLP01-561R) to maximize signal and minimize scattered laser light and then imaged on a 512 pixel × 512 pixel Andor iXon EMCCD (1 camera pixel = 49 nm in the imaging plane) at 40 ms/frame for 200 s.

### 2.3.4 Image processing and data analysis

The single-molecule fluorescence data was analyzed using custom-written MATLAB code. Before analyzing each image, the constant gold photoluminescence (Figure 2.4.4 B) was removed by subtracting the average of the surrounding 50 imaging frames from each image. This background subtraction left only the fluorescence from adsorbing Cy3.5 or mCherry molecules. Because the molecule can adsorb or desorb at any time during the imaging frame (typical adsorption times: 40 - 200 ms, Figure 2.4.4 C), the first and last frame of each adsorption event were excluded from our analysis to assure that every measurement correctly represents the brightness of a fluorescent molecule over 40 ms. Each diffraction-limited spot was fit to a 2D Gaussian function by least-squares fitting with the MATLAB routine *nlinfit* [129] to determine the center position and intensity. The NR position was determined from the fit to the NR photoluminescence pattern, and any molecule whose fit position was located within the 7 pixel × 7 pixel (343nm × 343nm) area about the gold NR center position was considered "on-NR" (Figure 2.4.4 A); any molecule outside of this box was considered "off-NR". The distribution of fluorescence intensities of each population (on-NR and off-NR) are shown in Figures 2.4.6 and 2.4.7, and the average fluorescence enhancements are plotted in Figures 2.4.5 B and D for Cy3.5 and mCherry, respectively. Error bars on the average fluorescence enhancement were calculated by bootstrapping the data from more than ten 5000-frame movies using resampling with replacement.

### 2.3.5 Finite Difference Time Domain (FDTD) simulations

Electromagnetic simulations were performed using the Lumerical FDTD software package. For each computation, a single NR was placed at the center of a 6.8 $\mu m^3$ simulation volume;

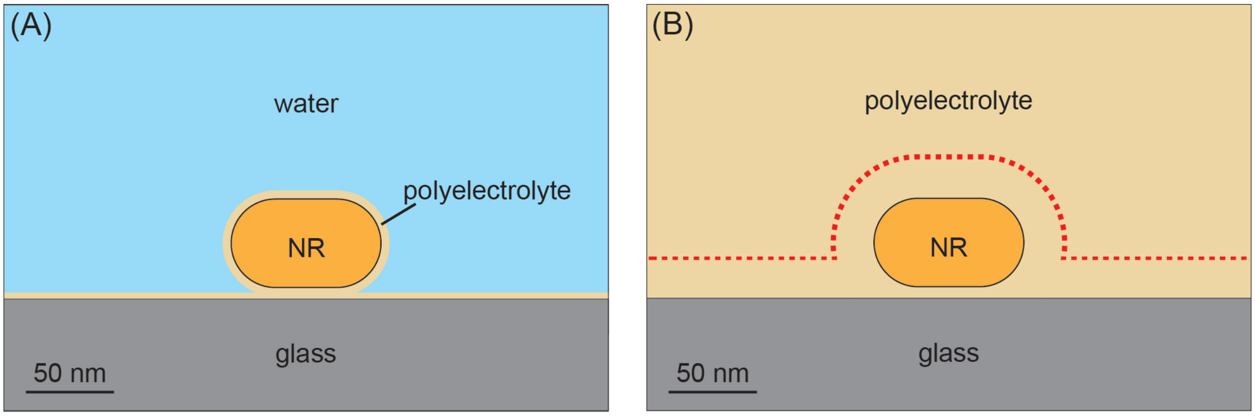

Figure 2.3.3: 2D cross section of the geometry for simulations of the electric field about a gold nanorod (NR). (A) The simulated dark-field scattering spectrum was obtained on an 85 nm × 50 nm NR immobilized in a dielectric layer and immersed in water. (B) The 3D electric field intensity along a conformal layer (red dashed line) about an isolated NR excited at 610 nm was calculated using finite-difference time domain simulations, and then averaging over the conformal surface sample, consistent with experiments.

near the NR, a fine-mesh grid with 0.614-nm$^3$ cells was used. Perfectly matched layer (PML) absorbing boundary conditions were used. The NR was excited from below at normal incidence with a broadband plane wave, and all results are the average of two orthogonal polarizations. The NRs were modeled as 50-nm diameter gold cylinders with hemispherical end caps and an end-to-end length of 85 nm (Figure 2.3.3 A). This NR size was chosen based on simulations of 50-nm diameter NRs in water (constant refractive index: $n = 1.333, k = 0$). The NR length was adjusted until the calculated extinction spectrum peak wavelengths matched the peaks in the experimentally measured UV-vis extinction spectrum of NRs in water (Figure 2.4.9 A).

To understand our microscopy fluorescence and scattering experiments, the full experimental geometry was simulated, including a glass coverslip and a dielectric medium. The single-particle dark-field scattering spectrum of an NR coated by 2.9 nm CTAB, enveloped in a 1.9-nm PSS conformal layer and deposited on top of a 1.5-nm PDADMAC film was simulated by calculating the scattering cross-section (blue line in Figures 2.4.9 B-G). The frequency-dependent complex permittivities of the NR and the glass coverslip were obtained from an analytical fit to experimental data from the literature for Au [130] and for glass. [131] New ellipsometry data for the PE layers (Figure 2.4.2 A, Figure 2.3.4) was used for assembled CTAB and PE or silica layers, which were all optically similar and therefore considered to be a uniform material.

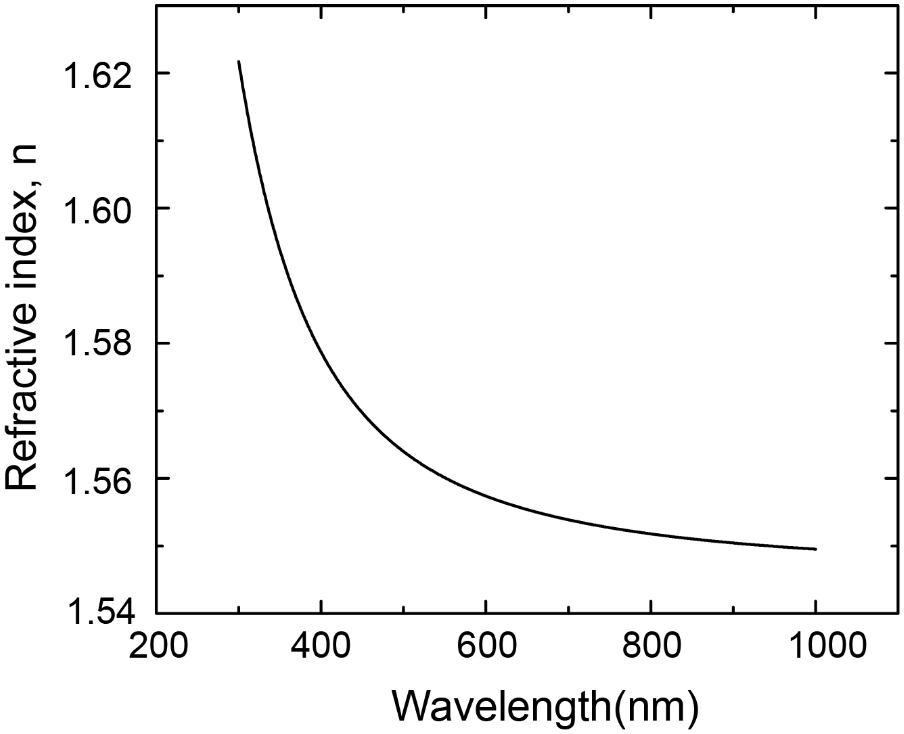

Figure 2.3.4: Refractive index, $n$, as a function of wavelength from the ellipsometry measurement of PE layers (Figure 2.4.2 A).

To match the experimental design, the electric field intensity, $|E|^2$, was calculated for a NR located 6.3 nm above a glass slab (consistent with the thickness of the base PDADMAC layer plus the PSS layer and CTAB coating [128] in which the NRs were immobilized in experiments), and embedded in a dielectric medium (Figure 2.3.3 B). The average local environment experienced by molecules adsorbing at random positions on top of the spacer layers was determined by recording the average electric field intensity, $|E|^2$, around the spacer-layer coated NR and above the PE-coated glass within a 343 nm × 343 nm area about the NR center based on a conformal surface (Figure 2.4.8 B). Since the 3D simulation does not uniformly sample this curved conformal surface, a weighted average was used to simulate the experimental uniform surface sampling. This enhanced average $|E(\lambda)|^2$ was considered specifically at the dye and FP emission maximum wavelength, $\lambda_{max} = 610$ nm (black curve in Figure 2.4.8 C). To account for quenching of dyes near nanoparticles, the fluorescence intensity at each position $(x, y, z)$ was considered proportional to $\eta(x, y, z)|E(x, y, z)|^2$, where the quantum efficiency modification, $\eta$, was defined as a function of nearest separation distance from the nanoparticle by an analytical fit to published data: [118] $\eta(d) = 1 - (\frac{d}{68.33+1})^{-6}$. Averaging $\eta$ over the surface gives the average quantum efficiency modification (red curve in Figure 2.4.8 C). To predict the average fluorescence enhancement from molecules adsorbing at random positions on top of spacer layers, multiplying $|E(\lambda)|^2$ with $\eta$ at each position and averaging the product values over the conformal surface within a 343 nm × 343 nm area about the NR center gives the average fluorescence enhancement (green curve in Figure 2.4.8 C), corresponding to our experimental region of interest.

## 2.4 Results and Discussions

### 2.4.1 Gold NR immobilization and substrate structure.

Single-molecule fluorescence microscopy was used to study the coupling to gold NRs of two types of fluorophores: the organic dye Cy3.5 and the FP mCherry. For these imaging experiments, the NR substrate was immersed in a fluorophore solution, from which fluorescent molecules stochastically adsorbed on and desorbed from the surface over time [113] for detection in an epifluorescence microscope (Figure 2.4.1 A). To prepare the NR substrate, gold nanorods were dispersed on a glass microscope coverslip (Figure 2.4.1 B) by spin coating a suspension of CTAB-coated gold nanorods in PSS. These immobilized NR substrates were then either used as such (spacer thickness 4.8 nm); coated further with 1 - 8 additional PE layers alternating the positive PDADMAC and the negative PSS to ensure monolayer deposition due to electrostatic forces (Figure 2.4.1 C), [127] or coated by a sputtered $SiO_2$ layer.

The final spacer layer thicknesses were determined by ellipsometry, as described in experimental section 2.3.1 (Figure 2.4.2). Spacer layer thicknesses were derived by fitting the spectral ellipsometry data to a Cauchy model, assuming a 1 nm native oxide thickness. For the polyelectrolyte films, the first four layers were found to be thinner than the later ones; the calibration data are therefore fit to a non-linear polynomial (Figure 2.4.2 A). The silica layer thicknesses were fit to a straight line (Figure 2.4.2 B). The error bars on PE thicknesses (Figures 2.4.5 B and D) reflect the polynomial fitting error, while the error bars on silica thicknesses (too small to be visible) come only from the instrumental error of ellipsometer since $R^2 = 0.99943$ for the fit.

### 2.4.2 Spectral properties of gold nanorods and fluorescent molecules.

The dark-field scattering spectrum of an isolated gold NR immobilized on a microscope coverslip as described above and immersed in water was measured (red line, Figure 2.4.3) and the maximum in the scattering spectrum, corresponding to the longitudinal plasmon mode

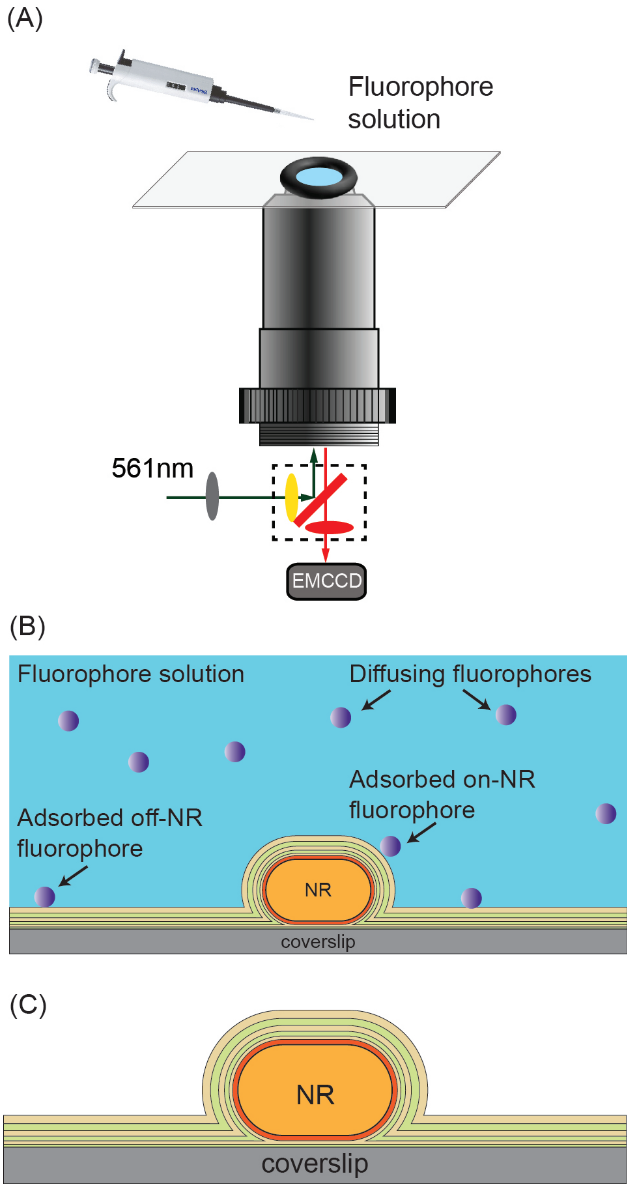

Figure 2.4.1: (A) Microscopy setup for PAINT experiments. A low-concentration fluorophore solution is excited by circularly polarized 561 nm laser illumination. The image of each fluorophore that adsorbs on the coverslip is detected by an EMCCD camera. (B) PAINT experiment sample geometry. A gold nanorod (NR) is immobilized in polyelectrolyte (PE) layers and immersed in a fluorophore solution (purple circles: single fluorophore molecules in the solution). (C) Structure of alternating PE layers deposited onto the NR. Dark red: CTAB bilayer surfactant; green: PDADMAC; beige: PSS.

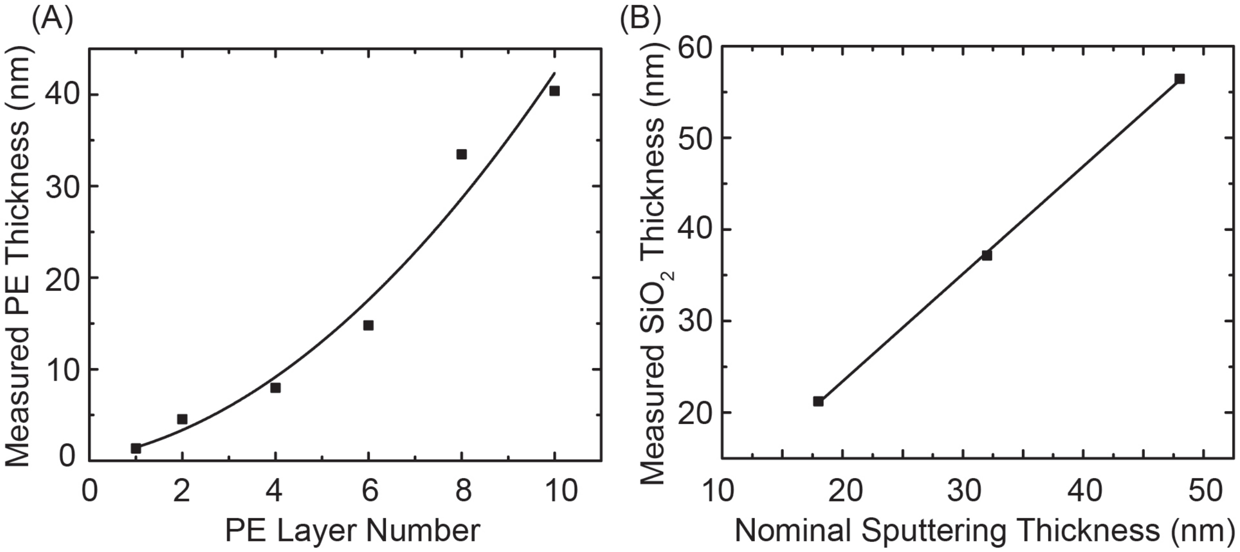

Figure 2.4.2: (A) Ellipsometry measurements of polyelectrolyte layer thicknesses. Squares: thicknesses of experimental samples from fits to a Cauchy model. Black line: second-order polynomial fit of data: $y = 0.21695 + 0.91471x + 0.32987x^2$. $R^2 = 0.95199$. (B) Ellipsometry measurement of sputtered SiO2 film thicknesses as a function of nominal thickness from the instrument quartz crystal balance. Squares: sample thicknesses from fits to a Cauchy model. Black line: linear fit of data: $y = 1.1738x - 0.06571$. $R^2 = 0.99943$. The spacer layer thicknesses in (A) and (B) are determined from the fit equations; the error bars on PE spacer thicknesses indicate the fitting accuracy; for the silica spacer thicknesses, these error bars represents the instrument error of the ellipsometer (too small to be visible in the plot).

resonance, was detected at 625 nm. The effect of the PE films on the NR plasmon resonance was evaluated by comparing the scattering spectrum of single gold NRs immobilized as described above, single gold NRs immobilized with 4 additional layers of PE on top and single gold NRs drop cast directly onto the glass (Figure 2.3.1). The longitudinal resonance peaks could all be well fit by a single Lorentzian function [132] allowing a linewidth to be defined. No significant differences in the linewidths were detected, indicating that the PE does not significantly influence the nature of the plasmon resonance.

Optimal fluorescence enhancement occurs when there is significant spectral overlap be-

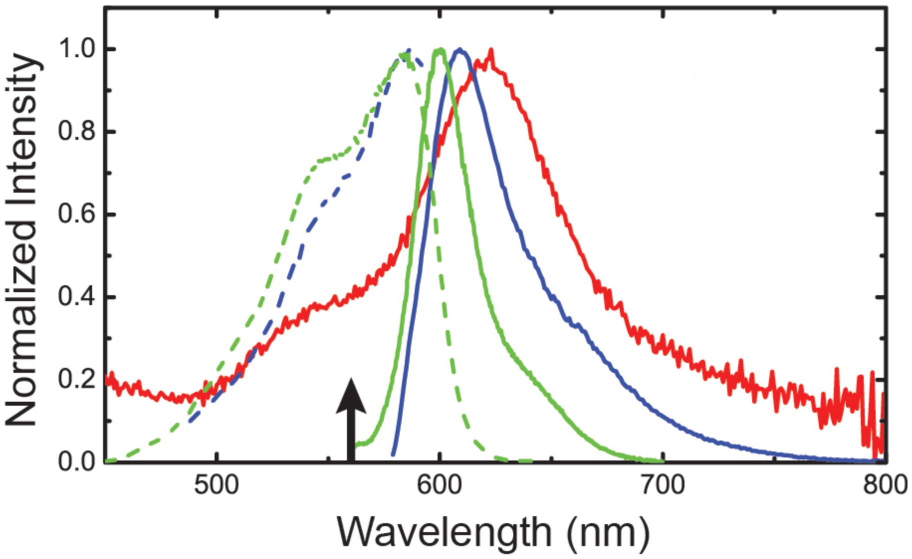

Figure 2.4.3: Dark-field scattering spectrum of an isolated NR immobilized on a coverslip in PE layers (red line); Cy3.5 fluorescence excitation and emission spectra (green dashed and solid lines, respectively); mCherry fluorescence excitation and emission spectra (blue dashed and solid lines, respectively). Excitation wavelength (561 nm) is indicated by a black arrow.

tween the plasmon resonance and fluorophore excitation or emission peaks. [105, 133] The organic dye Cy3.5 and the fluorescent protein mCherry were chosen for the overlap of their emission spectra with the measured NR longitudinal plasmon mode. The green dashed and solid lines in Figure 2.4.3 show the fluorescence excitation and emission spectra, respectively, of an 11 $\mu$M Cy3.5 aqueous solution (RF-5301PC Spectrofluorophotometer, Shimadzu Corporation). The blue dashed and solid lines in Figure 2.4.3 show the fluorescence excitation and emission spectrum of a 350 nM solution of mCherry in PBS. The excitation wavelength for both fluorescence emission measurements was 561 nm. The fluorescence emission maxima for the two fluorophores are 600 nm and 610 nm, respectively: both overlap well with the NR longitudinal resonance. We therefore expect NR coupling to lead to a modification of the spontaneous decay rate from both of these fluorophores. Though both the radiative and non-radiative decay rates will be affected, the quenching non-radiative interaction is more close-ranged than the enhancing radiative interaction, [134,135] so we expect to find a range of ideal spacer thicknesses at which the spontaneous decay rate increase will outweigh the non-radiative quenching to yield the net enhanced fluorescence that has previously been observed for organic dyes [94] and more recently, for intrinsic FPs. [47]

### 2.4.3 Single-molecule detection of fluorophores on spacer layers over gold NRs.

The fluorophore-NR coupling was studied with PAINT (Points Accumulation for Imaging in Nanoscale Topography) super-resolution imaging. [19,47] In these microscopy experiments, fluorophores stochastically adsorb to the NR substrate from the fluorophore solution above. The adsorbed fluorophores were visualized on the EMCCD detector as discrete punctate spots (Figure 2.4.1), whereas free molecules in solution (i.e., molecules not adsorbed on the substrate surface) were not detected because their Brownian motion was too rapid to be resolved by the EMCCD at a 25 Hz frame rate. [136] Maintaining a low concentration of fluorophores in solution (7 nM for mCherry and 22 nM for Cy3.5) ensured spatially isolated single-molecule adsorption events. The representative image in Figure 2.4.4 A shows five well-separated Cy3.5 molecules simultaneously adsorbed to an area of the substrate containing a single NR (white square). The gold NR photoluminescence emission pattern was averaged over 50 surrounding imaging frames in time domain, and the NR position was determined from the center of this average image (Figure 2.4.4 B inset). The constant gold NR photoluminescence (Figure 2.4.4 B) was subtracted from the raw data to yield a background-subtracted image of single fluorophores (Figure 2.4.4 C).

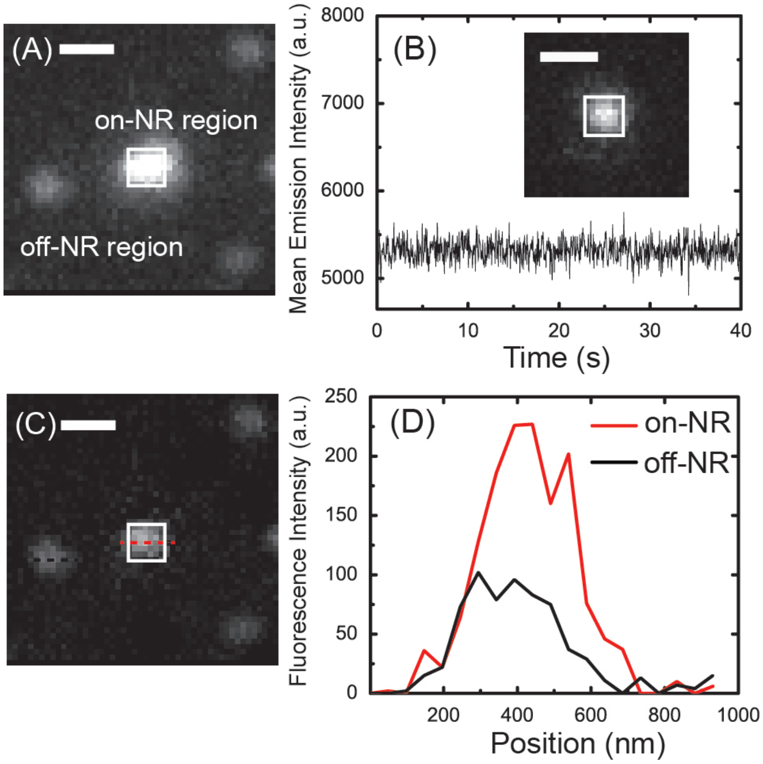

Figure 2.4.4: (A) Representative fluorescence image of adsorbed Cy3.5 molecules in an area with one NR. The imaging rate is 25 frames/s and the "on-NR" region is the area inside the 7 pixel × 7 pixel white square. (B) The mean photoluminescence intensity from an immobilized NR is constant over time (image shown in inset; the mean intensity is the average intensity value of the 49 pixels in the white square in the inset). (C) Fluorescence image corresponding to (A) after background subtraction; (A) and (C) are on the same greyscale. (D) Fluorescence intensity profiles along a cross section of the diffraction limited image of each of the two fluorophores indicated by dashed lines in (C). All scale bars in (A) - (C): 500 nm.

The fluorescent molecules were observed until they photobleached or desorbed from the surface. [46, 47] The center positions of these diffraction-limited single-molecule emission patterns were determined by fitting to a 2D Gaussian function (Experimental methods section). [25] Because the fluorescence emission pattern of a single molecule is affected by the presence of a proximal metal nanorod, the actual position of a single molecule cannot be precisely resolved in this system. [46] Instead, all fluorophores with positions inside the 7 pixel × 7 pixel (343 nm × 343 nm) area about the gold NR center position were designated "on-NR". [47] Here, we compare the emission intensity from on-NR fluorophores (adsorbed in the NR near field) to the emission intensity from off-NR fluorophores, which are unaffected by the presence of NRs. A profile of the fluorescence emission intensity along a line cut across the center of the emission pattern of an off-NR molecule (black dashed line in Figure 2.4.4 C) is compared to the fluorescence profile of an on-NR molecule (red dashed line in Figure 2.4.4 C) in Figure 2.4.4 D. Importantly, the emission intensity is increased in these representative traces, demonstrating plasmon-enhanced fluorescence.

### 2.4.4 Plasmon-enhanced fluorescence of single Cy3.5 dye molecules.

For each spacer thickness, the NR sample was immersed in Cy3.5 solution (22 nM in water), and the fluorescence intensities of each of $\sim$ 24,000 adsorbed Cy3.5 molecules were obtained from a Gaussian fit to background-subtracted movie frames such as the image shown in Figure 2.4.4 C. [129] The resulting localizations were divided into on-NR and off-NR populations (Figure 2.4.4 A), and all the fits from the two populations were binned by molecule brightness (counts detected per 40-ms imaging frame). Figure 2.4.5 A shows the distribution of emission brightnesses for Cy3.5 molecules adsorbing on top of a 14.2-nm silica spacer layer above the NRs; here, there is a significantly broader and brighter distribution for Cy3.5 molecules in the on-NR region (red) than in the off-NR region (grey). With this separation layer, the average brightness for Cy3.5 molecules on-NR is 195 counts and 131 counts for off-NR molecules; this ratio corresponds to a 1.5-fold average fluorescence enhancement, though several well-positioned and highly enhanced Cy3.5 molecules show up to 12-fold enhancement.

Plasmon-enhanced fluorescence depends on the tradeoff between quenching and spontaneous decay rate enhancement. This coupling is therefore very sensitive to the fluorophore-nanoparticle separation distance, which in our geometry is a function of the spacer layer thickness. To evaluate the effect of spacer thickness on single-molecule plasmon-enhanced fluorescence, the PAINT experiments described above were repeated for 11 different spacer thicknesses. The histograms for each of these geometries are presented in Figure 2.4.6. For each sample, the average fluorescence enhancement was calculated as the ratio between the mean fluorescence intensity on-NR and the mean fluorescence intensity off-NR. These average fluorescence enhancements are plotted as a function of spacer thickness in Figure 2.4.5 B. Here, we observe a non-monotonic trend: the average fluorescence enhancement increases from $\sim 1$ (no enhancement) at the smallest spacer thickness to a maximum 1.5-fold average enhancement at 14.2 nm spacer thickness (circled point in Figure 2.4.5 B) and then returns to $\sim 1$ at larger spacer thicknesses (the red line is a guide to the eye).

The average Cy3.5 fluorescence intensity is significantly enhanced for 9.4 nm - 14.2 nm spacer thicknesses; this region is highlighted with a beige stripe in Figure 2.4.5 B. We never observe significant quenching (i.e., average fluorescence enhancement $\ll 1$) because the thinnest spacer layer used in this experiment is 4.8 nm (a CTAB bilayer about the NR plus a PSS polyelectrolyte layer for immobilization). Still, the non-monotonic trend in Figure 2.4.5 B demonstrates the tradeoff between non-radiative quenching and plasmonic enhancement and indicates that a spacer layer thickness of $\sim$10 nm is ideal for increasing

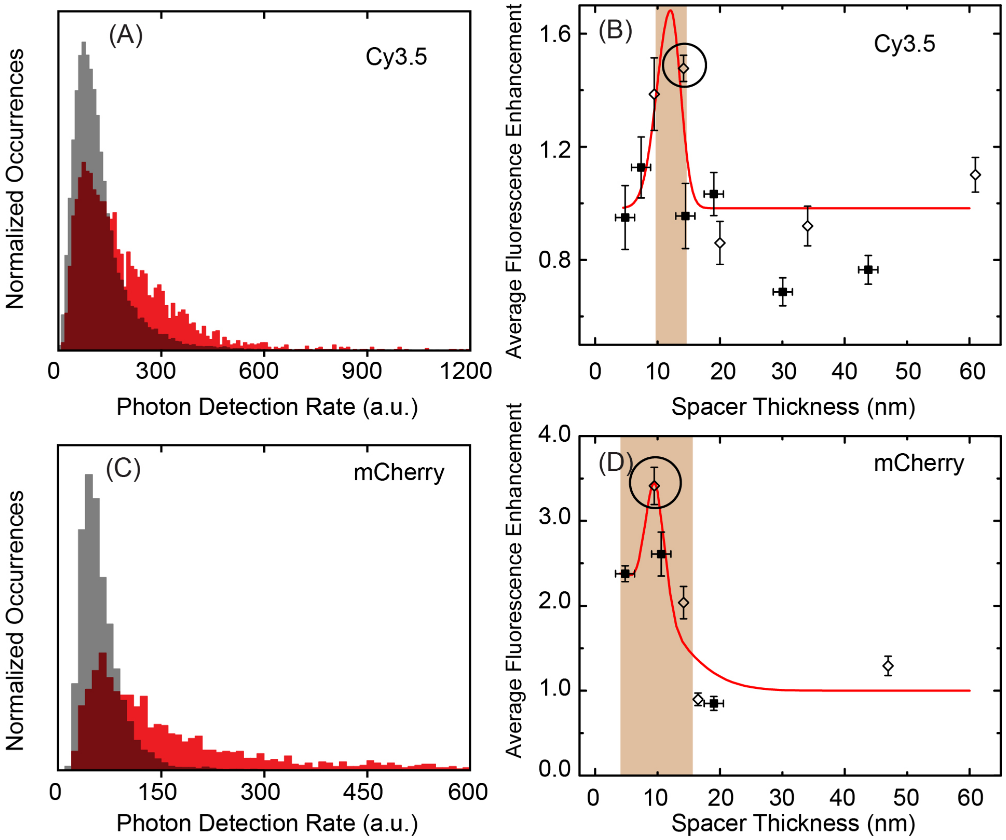

Figure 2.4.5: (A) Normalized distribution of single-molecule fluorescence intensities (counts detected per 40-ms imaging frame) of Cy3.5 molecules adsorbing on top of a 14.2 nm spacer layer (red: on-NR; grey: off-NR). (B) Cy3.5 average fluorescence enhancement vs. spacer layer thickness. Enhancement factor is defined as the ratio of the mean intensities of on-NR molecules and the mean intensities of off-NR molecules, calculated from histograms like (A). Beige stripe: region of significant average enhancement. Circled point: data derived from the histogram in (a). Open diamonds: samples with silica spacer layers; squares: samples with PE spacer layers. Red line: guide to the eye. (C) Normalized distribution of single-molecule fluorescence intensities of mCherry molecules adsorbing on top of a 9.5 nm spacer layer (red: on-NR; black: off-NR). (D) mCherry average fluorescence enhancement vs. spacer layer thickness. Enhancement factor is calculated as in (B). Beige stripe: region of average significant enhancement. Circled point: data derived from the histogram in (C). Open diamonds: samples with silica spacer layers; squares: samples with PE spacer layers. Red line: guide to the eye.

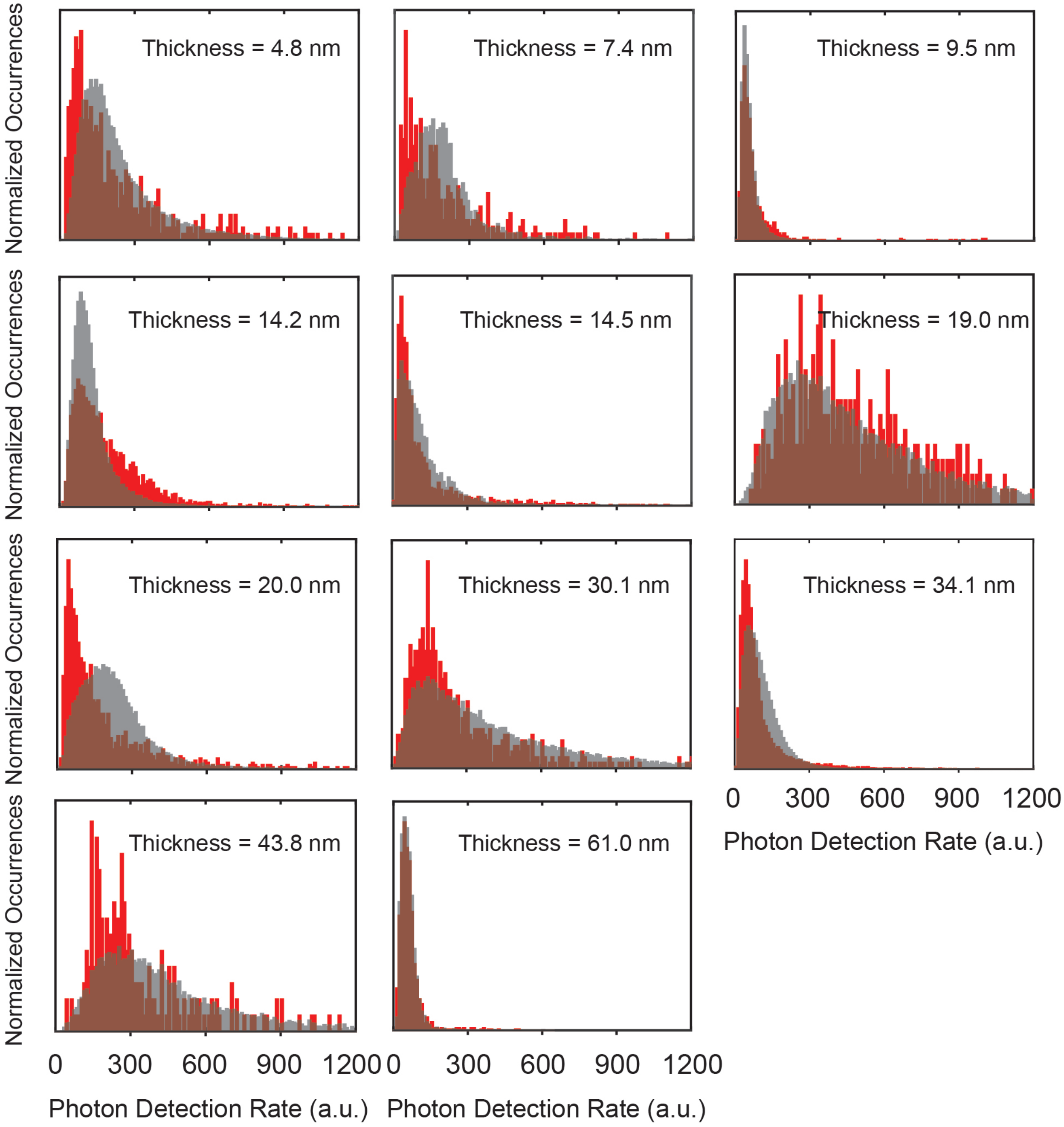

Figure 2.4.6: Histograms (normalized by area) of fluorescence intensities (counts detected per 40-ms imaging frame) for single Cy3.5 molecules adsorbing on top of all spacer layer thicknesses above the NRs in a Cy3.5 PAINT experiment, in the order of the data points in Figure 2.4.5 B. Red: on-NR; grey: off-NR.

Cy3.5 fluorescence emission in this geometry. Additionally, the spacer layers in the samples in Figure 2.4.5 B contain either silica (open diamonds) or PE (squares); since the optical properties of silica [131] and PE are quite similar (Figure 2.3.4), we don't expect to see different influence of the two materials, and indeed we observe that they form a pretty smooth trend here even though the PE layers can only have certain discrete thicknesses. We note that in these experiments, imperfect background subtraction of the NR photoluminescence can produce noise that registers as single adsorbed molecules. These false data points are consistently dimmer than the real on-NR or off-NR molecules and lead to an underestimation of the average fluorescence intensity on-NR. We therefore measure apparent average fluorescence enhancements $< 1$ at large separation distances in Figures 2.4.5 B and 2.4.5 D.

### 2.4.5 Plasmon-enhanced fluorescence of single mCherry fluorescent protein molecules.

To investigate the spacer thickness dependence of plasmon-enhanced fluorescence from single intrinsically fluorescent proteins, we examined the fluorescence intensity from the red FP mCherry on immobilized gold NR substrates immersed in an mCherry solution (7 nM in PBS). For every spacer layer thickness, the fluorescence intensity (counts detected per 40-ms imaging frame) of mCherry molecules adsorbing to the surface was recorded for $\sim$14,000 molecules, and the resulting distributions for on-NR and off-NR molecules are shown in Figure 2.4.5 C and Figure 2.4.7. The average fluorescence enhancement again observes a non-monotonic trend with spacer layer thickness (Figure 2.4.5 D). The enhancements increase with spacer layer thickness to a maximum at 9.5 nm and then decrease to $\sim 1$ (no enhancement) at longer distances $\geq 16.5$ nm. This region of significant enhancement is highlighted with a beige stripe in Figure 2.4.5 D. For mCherry as for Cy3.5, the nature of the spacer layer, i.e., silica (open diamonds) vs. PE (squares), does not affect the measured fluorescence enhancement. Our optimal spacer layer thicknesses also correspond very well with recently reported plasmon-enhanced fluorescence measurements for a bulk ensemble experiment of infrared dye molecules on similar gold nanorods. Indeed, because on-NR in our experiments accounts for the fluorescence emission from all molecules adsorbing over the entire 343 nm $\times$ 343 nm conformal surface, our optimal spacer thickness of $\sim$10 nm is consistent with the reported 17-nm optimal shell thickness in reference [134].

Interestingly, the mCherry fluorescence is significantly enhanced even at the smallest (4.8 nm) spacer layers thickness whereas these thin spacer thicknesses led to no enhancement of Cy3.5 fluorescence. This difference may be attributed to the fact that the 2-nm thick FP beta barrel isolates the chromophore from its surroundings, [137] providing an additional effective spacer thickness to prevent quenching. Also we expect the two fluorophores to have the same distance dependence since the enhancement depends no local electromagnetic field, not on the fluorophore properties, and indeed they peak at about the same distance, $\sim$ 10 nm. The subtle closer optimal distance for mCherry (compare Figures 2.4.5 B and 2.4.5 D) is consistent with the thickness of beta barrel. Furthermore, we observe a much larger maximum average fluorescence enhancement for mCherry than for Cy3.5 (3.4-fold vs. 1.5-fold). The smaller intrinsic radiative rate for the mCherry FP (0.15 $\mathrm{ns}^{-1}$) [138,139] relative to Cy3.5 dyes ($> 0.5$ $\mathrm{ns}^{-1}$) may make mCherry more sensitive to spontaneous decay rate enhancement in the near-field of the gold NR.

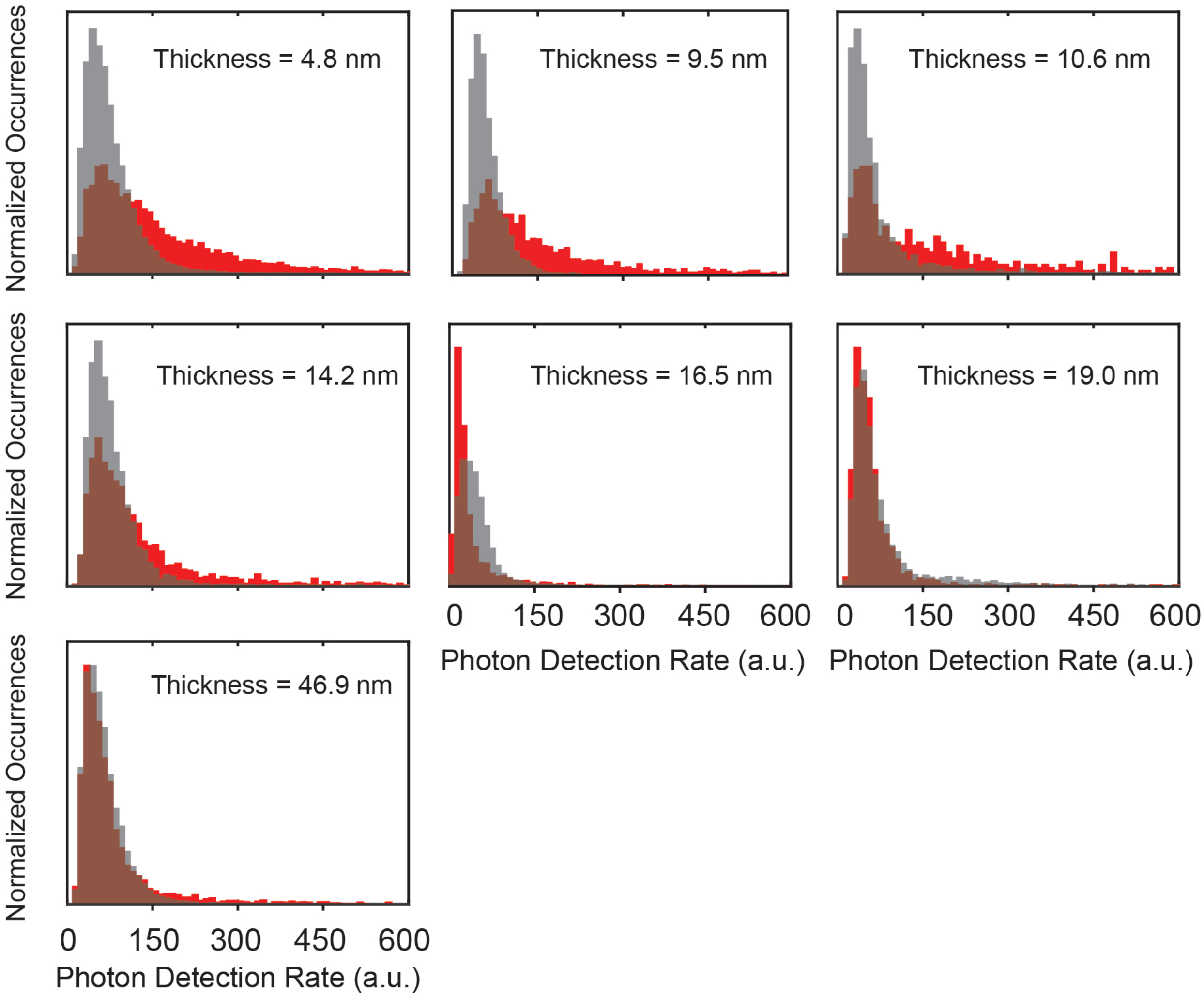

Figure 2.4.7: Histograms (normalized by area) of fluorescence intensities (counts detected per 40-ms imaging frame) for single mCherry molecules adsorbing on top of all spacer layer thicknesses above the NRs in an mCherry PAINT experiment, in the order of the data points in Figure 2.4.5 D. Red: on-NR; grey: off-NR.

### 2.4.6 Modeling a tradeoff between a local electric field intensity enhancement and quantum efficiency quenching reproduces the experimental spacer layer thickness dependence.

Figure 2.4.5 shows experimentally that the fluorescence emission from both single organic fluorophores and single fluorescent proteins can be enhanced in the simple geometry investigated (Figure 2.4.1), and that this enhancement is greatest at a spacer thickness of $\sim 10$ nm. Of note, this spacer thickness is not the average fluorophore/NR separation distance; rather, for every spacer thickness, our "on-NR" measurements include the emission intensities from dyes adsorbing over the entire 343 nm × 343 nm diffraction-limited region (Figure 2.4.8 B). We aggregate information from all possible fluorophore dipole orientations, as well as from fluorophore-NR separation distances up to $\sim 150$ nm. Thus, though a net average enhancement is observed in Figure 2.4.5, the broad on-NR distributions in Figure 2.4.6 and 2.4.7 reflect the fact that more distal fluorophores will maintain the fluorescence intensity of the off-NR case, while optimally positioned fluorophores will show maximal enhancement. To understand the plasmon enhancement for such a distribution, we used electromagnetic simulations that take the real experimental geometry into account. Here, we simulate the appropriate geometry by approximating fluorescence enhancement with a simple model: the plasmon-coupled fluorescence intensity is related to the product of the quantum efficiency modification [118] and the electric field intensity enhancement.

The dark-field scattering spectrum of a single gold NR immobilized in PE on a glass microscope coverslip and immersed in water was predicted with FDTD simulations of the same geometry; the experimental spectrum (red curve, Figure 2.4.8 A) matched the simulation of an 85 nm × 50 nm cylindrical NR with hemispherical caps (blue curve, 2.4.8 A). More

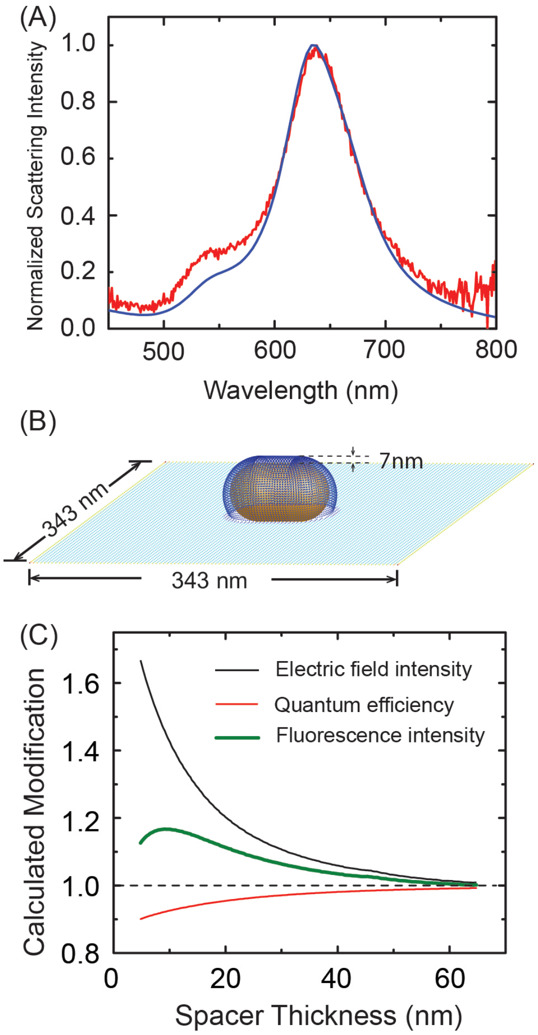

Figure 2.4.8: (A) Comparison of the experimental and calculated scattering spectra for a single 85 nm × 50 nm gold NR immobilized in PE on a glass coverslip (red: experimental dark-field scattering measurement; blue: FDTD simulation). (B) Representative geometry (spacer thickness = 7 nm) over which the 3D electric field intensity calculation is sampled to calculate the predicted fluorescence intensity enhancement for each spacer thickness. To be consistent with the experimental on-NR area, the conformal surface includes a curved surface (dark blue) and a flat surface (light blue) which extends to 343 nm × 343 nm. (C) Calculated average electric field intensity, $|E|^2$ (black), average quantum efficiency modification, $\eta$ (red), and total predicted fluorescence enhancement (green) on the conformal surface as a function of spacer thickness.

simulated UV-Vis spectra of NR solutions and scattering spectra are shown in Figure 2.4.9, and these spectra all match the experimental data very well, confirming the validity of this simulation. Subsequently, a three-dimensional map of the enhanced electric field intensity, $|E(x, y, z, \lambda)|^2$, which is directly proportional to the spontaneous decay rate enhancement, was calculated at the dye and FP emission maximum wavelength of $\lambda_{max} = 610$ nm at all dye positions $(x, y, z)$ about this NR. The simulated average enhanced electric field intensity on NR was determined by averaging the calculated field intensity over a conformal surface spanning the 343 nm × 343 nm box; Figure 2.4.8 B shows the conformal surface for a 7-nm spacer thickness. Each spacer thickness gives a different conformal surface, and the resulting average field intensity enhancement decays with increasing spacer thickness (black curve in 2.4.8 C).

Dye quenching near gold nanoparticles results in a decreased quantum yield: the ratio of the quantum yield of the nanoparticle-coupled dye and the isolated dye is less than 1. This relative quantum efficiency modification, $\eta(x, y, z)$, was defined at the closest dye-NR separation distance for each dye position, $(x, y, z)$, from an analytical fit to published non-radiative quenching data. [118] This $\eta(x, y, z)$ was averaged over the conformal surface, and because quenching is most severe at small separation distances, the relative quantum efficiency increased with increasing spacer thickness (red curve in 2.4.8 C).

The fluorescence enhancement occurs despite a tradeoff between spontaneous decay rate enhancement and quantum efficiency decrease, and our experimental average fluorescence enhancement should therefore follow the same trend as the product of the enhanced electromagnetic field intensity and the quantum efficiency decrease. This predicted dependence of fluorescence enhancement on spacer thickness (green curve in Figure 2.4.8 C) follows the same trend as the experimental measurements (Figures 2.4.5 B and 2.4.5 D): the calcu-

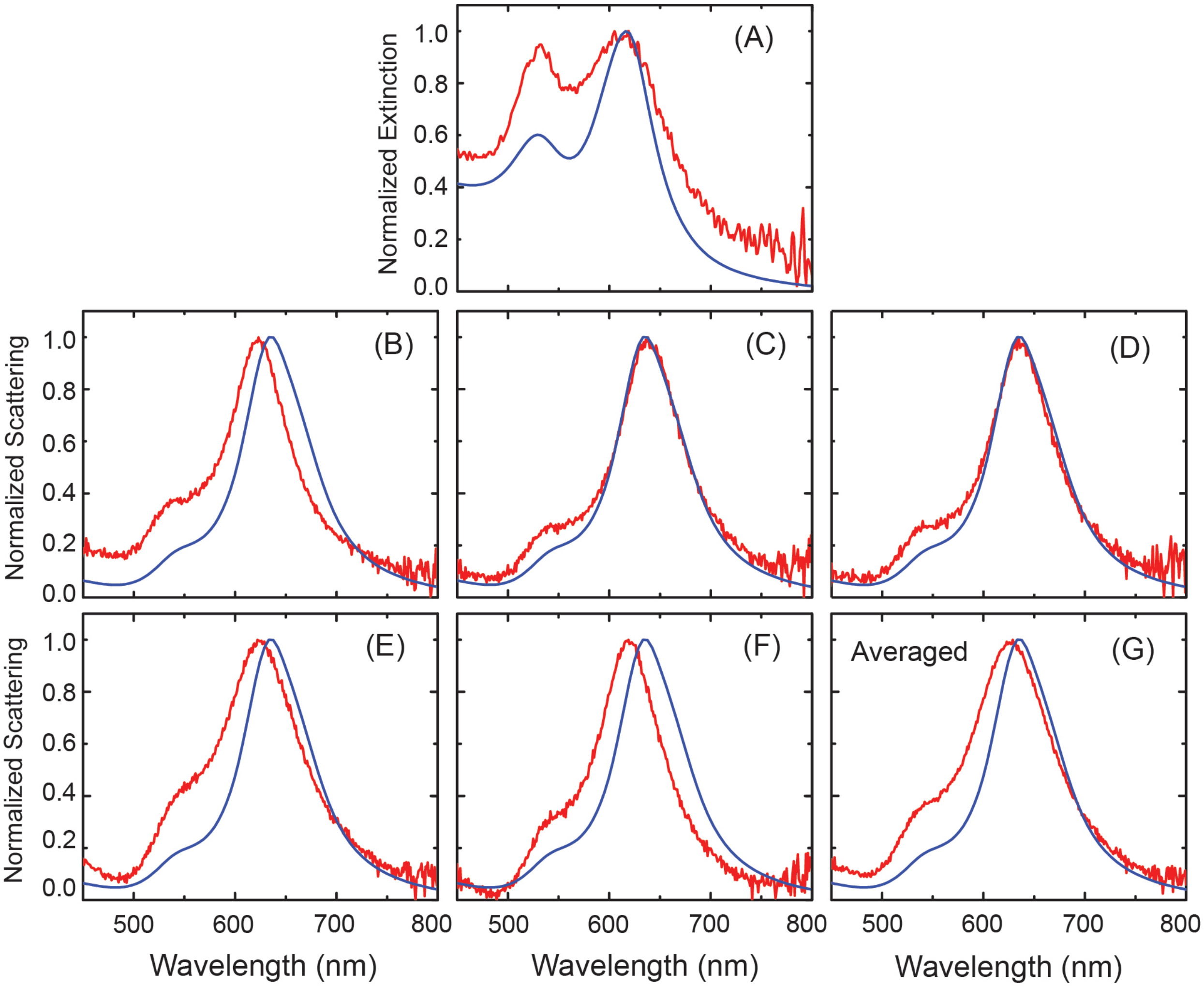

Figure 2.4.9: (A) Experimentally measured UV-vis absorption spectrum of bulk gold NR solution (red) and FDTD simulation of the extinction of a free 85 nm × 50 nm gold NR in water (blue). (B-F) Red: Five representative experimental dark-field scattering spectra for single gold NRs used in PAINT experiments. (G) Red: Average of 15 measured single-NR dark-field scattering spectra. Blue curve in (B-G): FDTD simulation of an 85 nm × 50 nm gold NR immobilized in polyelectrolyte (Figure 2.3.3).

lated total fluorescence enhancement curve is maximal at 9.1 nm and the experimental and computational curves have similar shapes, thus validating our understanding of the tradeoff between enhancement and quenching.

## 2.5 Conclusions and future directions

We have investigated the distance dependence of fluorescence emission from both organic dyes and fluorescent proteins at the single-molecule level. We find that both types of fluorophores can be enhanced by interactions with single colloidal gold NRs prepared in a simple geometry. The enhancement is improved upon the introduction of thin spacer layers to prevent non-radiative quenching at small separation distances. Both Cy3.5 and mCherry are maximally enhanced for spacer thicknesses of 10 nm, and the enhancement is observed for sputtered silica spacer layers, as well as for spin-cast alternating polyelectrolyte layers. We observe a larger maximum enhanced fluorescence for mCherry than for Cy3.5, which is attributed to the smaller intrinsic radiative rate of mCherry. Our observations are consistent with a model that considers fluorescence enhancement to be a tradeoff between spontaneous decay rate enhancement from the enhanced electric field about the NR (predicted by FDTD simulations) and the quenching that was previously calculated by Anger et al. [118]

Super-resolution images can be obtained based on single-molecule fluorescence, [140,141] with important consequences for biological imaging. However, the single-molecule imaging resolution depends on the brightness and photostability of the fluorescent probes, and the most widely used fluorescent labels in biological imaging are fluorescent proteins, which have particularly low quantum yields and photostabilities. [142] Plasmon-enhanced fluorescence therefore holds great promise for improved super-resolution imaging. Here, we have used single-molecule detection to study this improvement in the same single-molecule microscope for which the system is intended. We observe enhancement of conventional labels in a simple experimental design that involves a geometry that can readily be extended to imaging single fluorophores in the membranes of live cells. [117] However, the large distance distribution existing in this PAINT experimental design does not truthfully reflect the distance-dependence. This problem will be further studied in the following Chapter 3. One other issue that will require further study is that, due to the presence of nanostructure, the apparent fluorescence emission position of a single dye molecule may get shifted toward the metal, which contributes a new term to the super-resolution uncertainty. This point has recently been addressed by several groups [46, 100], including Chapter 4 of this Thesis and will eventually resolve this mislocalization issue. At that time, these in vitro structures can be readily extended to cellular imaging experiments in which the spacer layer would be replaced by the cellular envelope; this experiment is therefore a first step toward plasmon-enhanced imaging in living cells. Thus, by improving the photon yield of single-molecule emitters without sacrificing the bio-compatible and non-invasive nature of far-field optical microscopy, the resolution and sensitivity of single-molecule biological imaging can be improved.

# CHAPTER III

# Plasmon-enhanced fluorescent proteins coupled to gold NP with precise distance control

## 3.1 Abstract

Fluorescent proteins (FPs) are arguably the most important and unique fluorescent probes in biological fluorescence imaging. The special advantage of FPs is that they can be genetically encoded to the target protein. As a result, the labeling procedure is very quantitative: each target is bound to a single label. Furthermore, there are no free labeling probes in the systems, and thus background is tremendously decreased. Finally, FPs don't usually contain any toxic element and introduce minimal perturbations to living cells. However, compared to organic dye molecules, FPs usually have lower quantum yield and are generally dimmer. Recently, plasmon-enhanced fluorescence has been applied to single-molecule super-resolution imaging. This approach shows great potential for plasmonic substrates to increase the average probe intensity by at least 2-fold. Here, we further explore this distance-dependent phenomenon with a focus on photoactivatable FPs. FPs are carefully placed near gold nanoparticles (NPs) with nanometer-scale silica shell spacers. Two different FPs—the

red PAmCherry and the green PAGFP—are coupled to the NPs, separated by different spacer layers so that the distance dependence and spectral properties are accessible for investigation. This study provides an approach to understanding the plasmon enhancement of FPs in a system that allows precise control of the separation distance between plasmonic NPs and FPs without large heterogeneity. Overall, by looking at fluorescence from single molecules one at a time, it is found that, different from the previous result that no enhancement observed with a 20 nm spacer layer, [48] here 20 nm silica shell (corresponds to a uniform 20 nm distance separation) actually gives a 2-fold enhancement, which was hidden by large distance distribution before. Larger distance (i.e. 80 nm) shows no enhancement as expected due to weak plasmonic coupling.

## 3.2 Introduction and motivation

To solve mysteries about how living organisms function, scientists are always looking for appropriate probes to image proteins in cells. Among all the probes, fluorescent proteins (FPs) have received continuous interest since the discovery of green fluorescent protein (GFP) in the 1960s, and numerous FPs of different emission wavelengths, quantum efficiencies or other optical properties have been developed since. [58] FPs are very important labeling tools since they can be genetically fused to target proteins and exert minimal perturbation to the targets. Recently, cellular imaging based on FPs has been taken to the next level by single-molecule super-resolution fluorescence imaging. In contrast to traditional microscopy, which is generally limited to hundreds of nanometers by the wave nature of light, single-molecule super-resolution imaging achieves a much improved spatial resolution (down to tens of nanometers). [25] Imaging FPs with this resolution is very useful for understanding subcellular structures and protein dynamics in cells. When imaging single fluorescent molecules, the resolution improves with the label brightness and stability. Theoretically, the resolution is inversely proportional to the total number of collected photons in each imaging frame. [25] Therefore a brighter probe, which emits more photons, will provide better resolution. Unfortunately, FPs are at a disadvantage in this regard: their low quantum yields make them less bright than organic dyes or quantum dots, and their short photobleaching lifetimes mean that they turn off relatively fast during imaging. [142] These drawbacks limit the application of FPs in single-molecule fluorescence imaging by decreasing the resolution and the track lengths that can be observed in biological processes.

Noble metal nanoparticles (e.g., silver, gold and platinum) support resonant electron oscillations, termed localized surface plasmon resonances (LSPRs), upon excitation at the wavelength matching the natural frequency of the nanoparticle. [67] This interaction generates a significantly enhanced electromagnetic (EM) field closely localized to the nanoparticle surface. Due to this increased EM field, plasmonic nanoparticles have a long history of being used in enhanced spectroscopies, including surface enhanced Raman spectroscopy (SERS) and enhanced fluorescence. If the excitation and/or emission spectra of a fluorescent molecule in the enhanced plasmonic field overlaps with the LSPR frequency, resonant coupling is expected to happen between the molecule and the metal nanoparticle. [133] This coupling will lead to an increased spontaneous decay rate, for both radiative (fluorescence) and non-radiative decay processes. When the right balance is achieved, the fluorescence intensity is increased due to faster radiative decay rate, and the molecule photostability is enhanced as well since the electrons spend less time in the excited state, and thus fluorescence is less likely to be quenched after going through inter-system crossing (Figure 3.2.1). Furthermore, this effect is most significant for lower quantum yield fluorophores like most fluorescent pro-

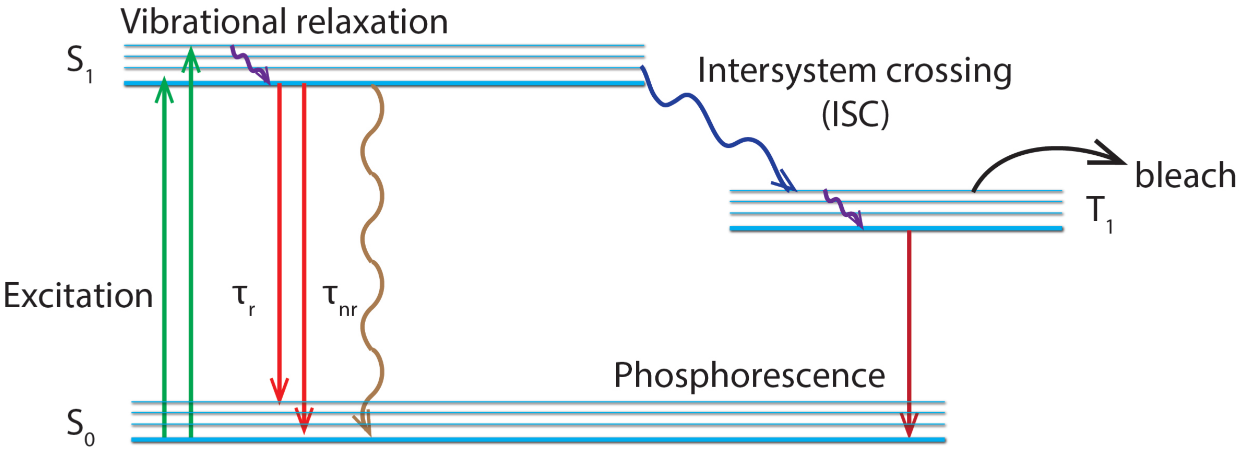

Figure 3.2.1: Jablonski diagram of an excited fluorescent molecule. Due to plasmon-enhanced decay rates, the excited electrons spend less time in $S_1$ therefore ISC and further quenching is less likely to happen, i.e. the photo stability of the molecule is increased.

teins. Gold nanoparticles, which have LSPR frequencies in the visible range and which are non-toxic to living organisms, are a good candidate for plasmon-enhancing FPs.

However, the interactions between nanoparticles and fluorophores are complex because both radiative and non-radiative decay pathways are affected by the enhanced EM field, and this field intensity varies with position. When the fluorophore is located too close to the nanoparticle surface or touches it, non-radiative electron decay dominates, which leads to a quenching effect that outweighs enhancement. Indeed, many groups have reported dye quenching by metal nanoparticles. [48, 114, 123] On the other hand, we and others have observed plasmon-enhanced fluorescence for single fluorescent dyes and FPs molecules in different geometries. [47, 134] The balance between the two competing processes of radiative and non-radiative enhancement determines the overall brightness and stability of the fluorophore in the presence of a plasmonic nano-antenna, and this balance is sensitively distance-dependent. To best utilize this plasmonic fluorescence enhancement, the distance-dependence needs to be studied in further detail for both mechanistic understanding and practical application. The interactions of FPs with nano-antennas are particularly poorly understood. Furthermore, studies on the single molecule level are essential for revealing the heterogeneity hidden under the ensemble average. Therefore, this Chapter seeks to enhance FP fluorescence based on close coupling to noble metal nanoparticles, and to understand the distance-dependence of this enhancement effect free from heterogeneous average using single-molecule imaging and symmetric single-particle assemblies.

Here, we construct an assembly consisting of FPs separated from a gold NP via a finely tuned silica shell spacer layer for nanometer-scale distance control. The homogeneous NP-FP separation distance truthfully reflects the distance-dependent plasmon-enhancement effect. Red photoactivatable FP, PAmCherry, is observed to be enhanced 2-fold when coupled to gold NPs with a 20 nm spacer. This result differs from our previous study, where no enhancement was observed for FPs adsorbing to the surface about a gold nanorod coated by a 20 nm polymer spacer. This discrepancy is explained by the fact that the current study has a more precise distance control therefore is not the average of a large distance distribution; moreover, it contains information from every single molecules and reveals the intrinsic heterogeneity of FPs. Furthermore, from the single molecule information, we can clearly see that some population of molecules are actually enhanced up to 100-fold, which is consistent with the theoretical limit. This study bridges the gap between 1) our previous measurements, where fluorophores were allowed to adsorb and de-adsorb on a spacer coated nano-antenna therefore there was large distribution of separation distance; [48] and 2) other papers that showed enormous enhancement for one optimally placed emitter. [94]

## 3.3 Methods and Results

### 3.3.1 Synthesis of silica-coated gold NP

Synthesis of gold nanoparticle and the coating of silica shell was carried out through collaboration with Dr. Catherine Murphy's lab. Synthesis of gold NP and silica coating were modified from previously published work. [143, 144]

### 3.3.2 Cloning of streptavidin-PAmCherry/PAGFP fusion

Streptavidin plasmid was purchased from Addgene (pET21a-Streptavidin-Alive was a gift from Alice Ting, Addgene plasmid# 20860). [145] The plasmid was extracted from cells and linearized and amplified by PCR (Table 3.1 primers 1 and 2). In the meantime, PAmCherry sequence [146] was amplified through PCR as well (Table 3.1 primers 3 and 4 ) to obtain complimentary overhang with the streptavidin plasmid PCR product. The two parts were combined together by Gibson assembly (Figure 3.3.1 Step1). [147] The assembly product transformed into competent *E. coli* cells through electroporation.

Transformed cells were incubated for 1 hr to recover full viability before selected on Agar/LB/Ampicillin plate overnight (Figure 3.3.1 Step 2). After selection, the recombinant colonies were verified by sequencing. First the plasmid DNA was isolated from the overnight culture and then Sanger sequencing was used to confirm the correct orientation of the inserted PAmCherry gene (Figure 3.3.1 Step 3).

Similarly, streptavidin-PAGFP was also constructed from the Gibson assembly approach (Table 3.1 primer 5 and 6). PAGFP plasmid was purchased from Addgene (pRSETA-PAGFP was a gift from Jennifer Lippincott-Schwartz, Addgene plasmid # 11911). [148]

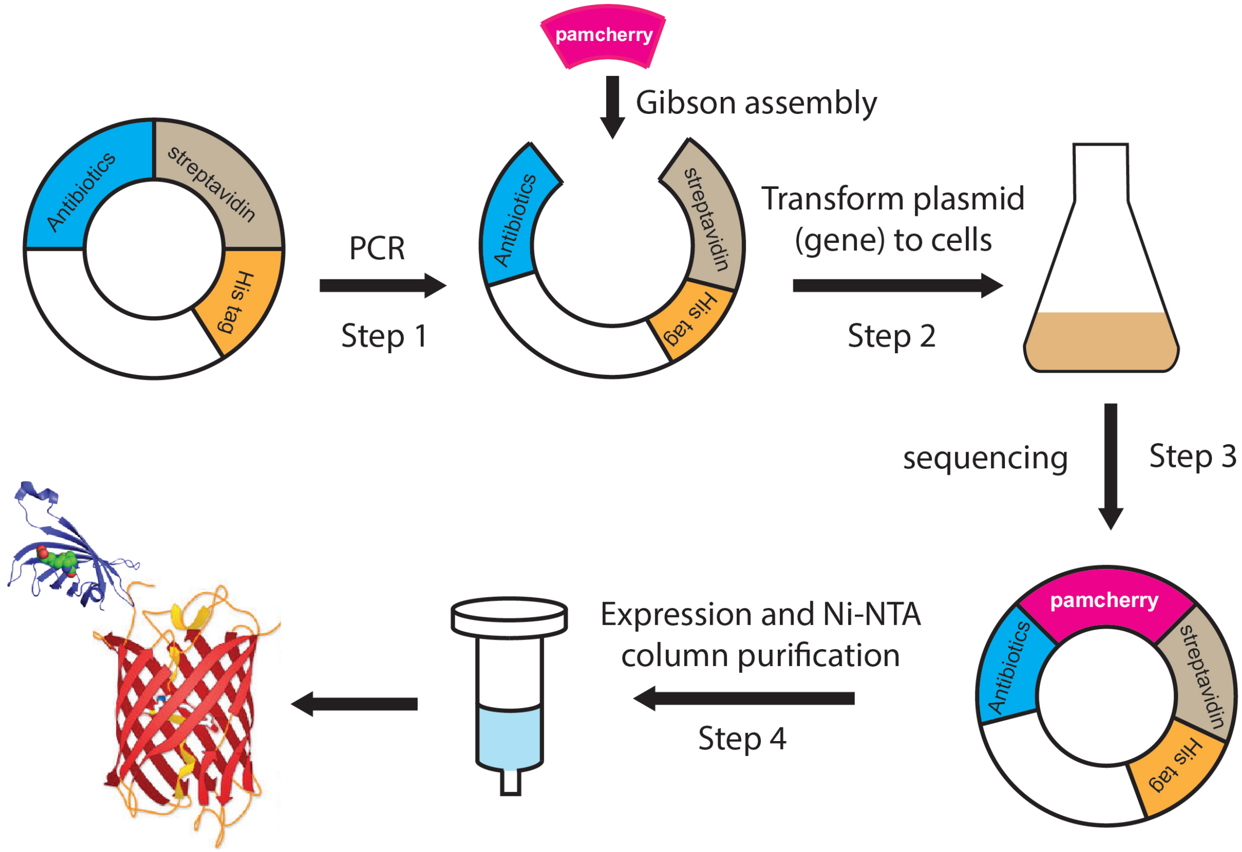

Figure 3.3.1: Step 1: The streptavidin plasmid and the PAmCherry sequence were linearized and amplified by PCR. Step 2: The PCR products from the two sequence were assembled by Gibson assembly and transformed into competent *E. coli* cells by electroporation. Step 3: The correctly assembled plasmid was selected through sequencing, and cells were harvested for purification. Step 4: The PAmCherry-streptavidin fusion protein was extracted and purified from cell cultures by Ni-NTA chromatography through His-tag affinity.

| Primer number | Sequence |
|---|---|
| 1 | GCT GAA GCT GGT ATC ACC |
| 2 | ATG TAT ATC TCC TTC TTA AAG TTA AAC |
| 3 | TTT AAG AAG GAG ATA TAC ATA TGG TGA GCA AGG GCG AG |
| 4 | TGA TAC CAG CTT CAG CCT TGT ACA GCT CGT CCA TGC |
| 5 | TTT AAG AAG GAG ATA TAC ATA TGG TGA GCA AGG GCG AG |
| 6 | CCG GTG ATA CCA GCT TCA GCC TTG TAC AGC TCG TCC ATG C |

Table 3.1: Summary of all the primers used for cloning. Primers 1 and 2: forward and reverse primers for streptavidin PCR; primers 3 and 4: forward and reverse primers for PAmCherry PCR; primers 5 and 6: forward and reverse primers for PAGFP PCR.

### 3.3.3 Expression and purification of streptavidin-PAmCherry/PAGFP fusion protein

The fusion protein streptavidin-PAmCherry was expressed and purified from *E. coli* bacterial cells. *E. coli* cells containing recombinant streptavidin-PAmCherry plasmid was first grown overnight. 1 mL overnight culture was then diluted into 100 mL fresh LB with Ampicillin at 37°C with shaking. The culture was induced with 0.1 mM IPTG (Isopropyl $\beta$-D-1-thiogalactopyranoside) at $OD_{600}$ of 0.5 - 0.7 and was grown for another 2 hours before harvested. Pre- and post-induction cell samples were boiled at 95°C for 5 min and characterized by PAGE (polyacrylamide gel electrophoresis) to confirm the success of induction (Figure 3.3.2). We observed a new dominant band at 40 kDa after IPTG induction, which was consistent with the size of the recombinant protein (PAmCherry: 26 kDa; monomeric streptavidin: 14 kDa). This band indicated that the recombinant protein was successfully constructed and over-expressed in *E. coli* bacterial cells.

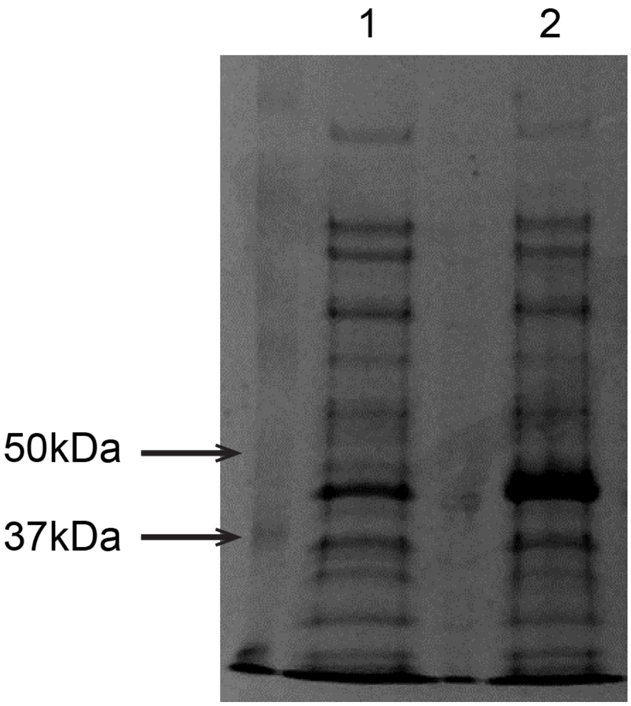

Figure 3.3.2: PAGE analysis of *E. coli* cells containing streptavidin-PAmCherry before (lane 1) and after IPTG induction (lane 2). The same amount of cells were loaded in each lane based on $OD_{600}$.

100 mL of induced cells were harvested and spin down at 5000 rpm for 10 min. Cell lysis was done in B-PER (Bacterial Protein Extraction Reagent, ThermoFisher Scientific) with 10$\mu$g/mL DNaseI, 0.1mg/mL lysozyme and 1 mM PMSF at room temperature for 15 min. The lysate was centrifuged at 15000 g for 5 min, and the supernatant was separated for further purification. The over-expressed proteins were likely to form inclusion bodies and go into insoluble precipitates, [149] but nevertheless, some portion of the protein was still found in the supernatant. For $\sim$ 5 mL lysate supernatant, 1 mL Ni-NTA affinity matrix (Ni-NTA Agarose, QIAGEN) was loaded to a column for gravity-flow chromatography. The column was first equilibrated with 0.5 mL lysis buffer (50 mM $NaH_2PO_4$, 300 mM NaCl, 10 mM imidazole) three times, then the protein supernatant was applied to the column; the column

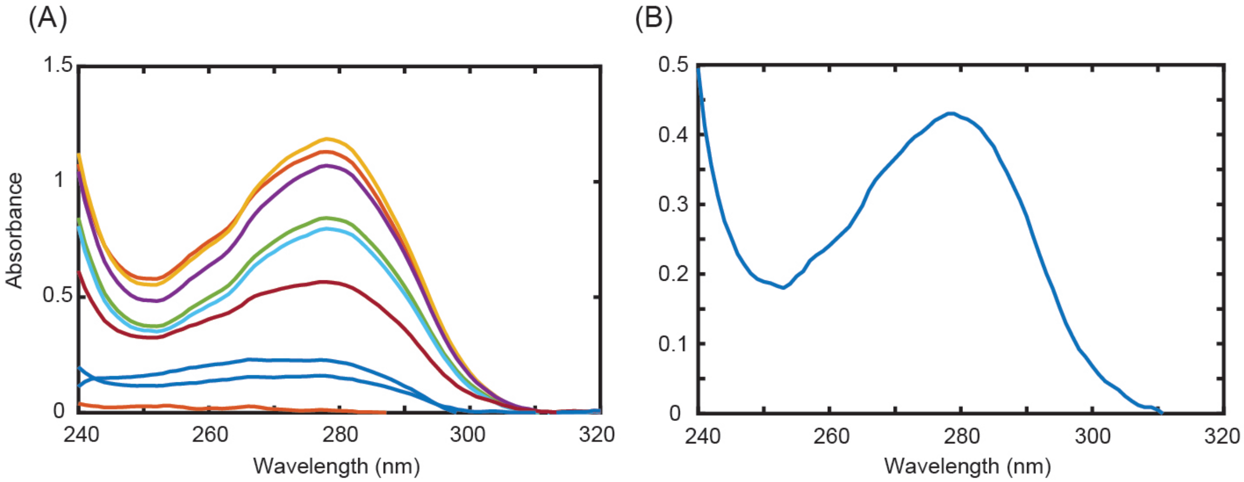

Figure 3.3.3: (A) UV absorption spectra of eluted streptavidin-PAmCherry fusion protein from Ni-NTA column. From top to bottom: elution fractions No. 3, 2, 4, 5, 6, 7, 8, 1, 9. (B) Absorption spectrum of dialyzed protein from combined eluted fractions No. 2 - 8.

was washed with 0.5 mL washing buffer (50 mM $NaH_2PO_4$, 300 mM NaCl, 30 mM imidazole) multiple times until all the non-specific proteins were washed out (monitored by A280) of the column, and the fusion protein was then eluted with elution buffer (50 mM $NaH_2PO_4$, 300 mM NaCl, 250 mM imidazole) into 0.2 mL fractions. UV absorption (NanoDrop 2000 UV-vis Spectrophotometer, Thermo Scientific, Figure 3.3.3A) showed that the eluted protein started to appear in the second elution fraction, which indicated the protein was indeed specifically bound to the column due to His-tag affinity. PAGE analysis of some of the washing fractions and the elution fractions showed that the eluted protein was pure and had the expected size of 40 kDa (Figure 3.3.4).

Elution fractions No. 2 to No. 8 were combined and dialyzed against 900 mL PBS at 4°C overnight. The absorption spectrum of the dialyzed protein was also measured (Figure 3.3.3B). The single peak at 280 nm indicates the purity of the final protein product. The photoactivity of the purified fusion protein were also shown to remain intact by fluorescence

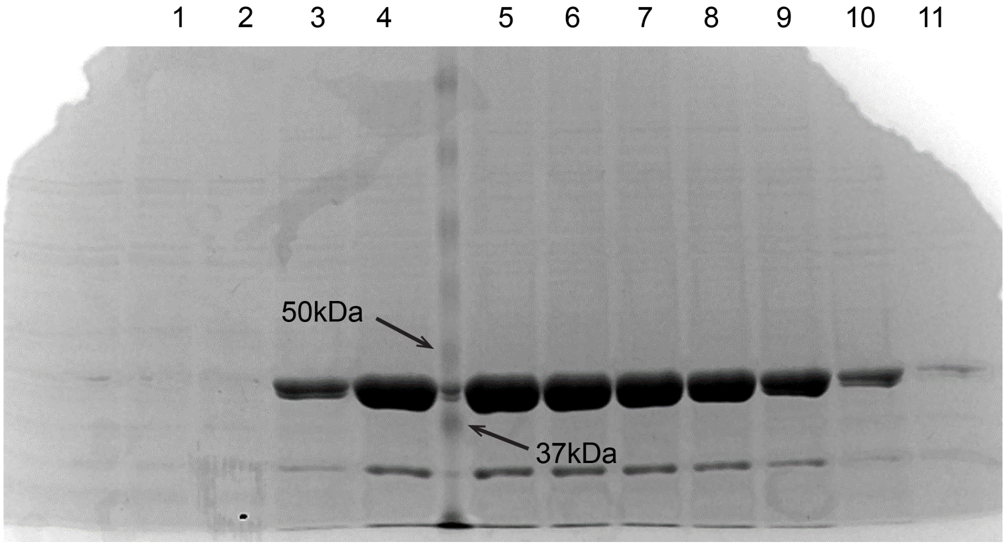

Figure 3.3.4: PAGE analysis of washed and eluted streptavidin-PAmCherry fusion protein fractions. Lanes 1 - 2: 5th and 6th fractions that washed off non-specific bound proteins; lanes 3 - 11: eluted fractions of fusion protein No. 1 - 9. The dominant band represents the eluted fusion protein band.

imaging on the microscope. Furthermore, to make sure that the fusion protein still kept the ability to bind biotin molecules with high affinity, gel electrophoresis was performed as follows: 2 $\mu$L 50 $\mu$M DNA strands (5'- CG TTA AAG GTA TGC AGG TAT CGC GGC ATG ATA GCC GTG TAC TTT CAG TCA GTG CCA TGT ACT AGC GAT GGC AAG -3') with or without a biotin molecule modified at the 5' end were mixed with 8 $\mu$L streptavidin-PAmCherry fusion protein and incubated at room temperature for 15 min for complete conjugation. The two mixtures were then applied to a 1% agarose gel for electrophoresis. As illustrated in Figure 3.3.5A, if the protein can indeed bind biotin molecules, the biotinylated DNA will be slowed down by the conjugated protein and appear at a higher position; as a reference, DNA without biotin modification will run faster and appear at a lower position. The experimental data (Figure 3.3.5B) confirmed that the fusion protein can bind biotin: we observed a slow, broad new band (in lane 1) which corresponded to a conjugation of the

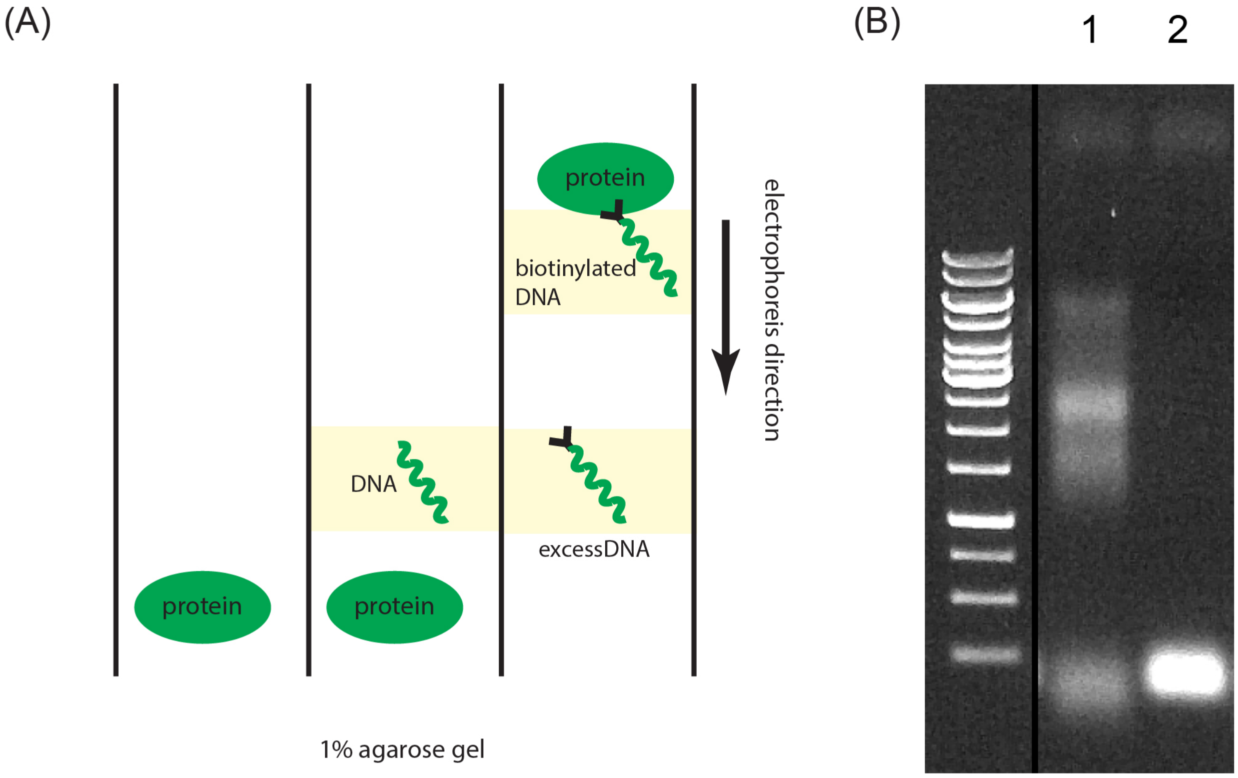

Figure 3.3.5: (A) Illustration of the mechanism for testing the biotin affinity for the streptavidin-PAmCherry fusion protein. (B) Experimental demonstration of the biotin affinity for the streptavidin-PAmCherry fusion protein. Lane 1: fusion protein + biotinylated DNA; lane 2: fusion protein + DNA without biotin modification.

fusion protein and the DNA (compared to the compact, faster band in lane 2, where the DNA doesn't have a biotin molecule modified at the end). Overall, the streptavidin-PAmCherry fusion protein proved to be functional for biotin binding as well as fluorescence imaging.

For streptavidin-PAGFP, similar cloning and purification processes were performed. However, it was found that the fusion protein was poorly expressed in *E. coli* compared with streptavidin-PAmCherry (Figure 3.3.6 lanes 1 and 2). No new dominant band was seen after IPTG induction. It is known that a species has preference for coding one certain amino acid when there is codon degeneracy. Therefore, for the same protein, the synthesis efficiencies

| Name | Sequence |
|---|---|
| codon-optimized PAGFP | ATG GTT TCT AAA GGT GAA GAA CTG TTC ACC GGT<br>GTT GTT CCG ATC CTG GTT GAA CTG GAC GGT GAC<br>GTT AAC GGT CAC AAA TTC TCT GTT TCT GGT GAA<br>GGT GAA GGT GAC GCT ACC TAC GGT AAA CTG ACC<br>CTG AAA TTC ATC TGC ACC ACC GGT AAA CTG CCG<br>GTT CCG TGG CCG ACC CTG GTT ACC ACC TTC TCT<br>TAC GGT GTT CAG TGC TTC TCT CGT TAC CCG GAC<br>CAC ATG AAA CAG CAC GAC TTC TTC AAA TCT GCT<br>ATG CCG GAA GGT TAC GTT CAG GAA CGT ACC ATC<br>TTC TTC AAA GAC GAC GGT AAC TAC AAA ACC CGT<br>GCT GAA GTT AAA TTC GAA GGT GAC ACC CTG GTT<br>AAC CGT ATC GAA CTG AAA GGT ATC GAC TTC AAA<br>GAA GAC GGT AAC ATC CTG GGT CAC AAA CTG GAA<br>TAC AAC TAC AAC TCT CAC AAC GTT TAC ATC ATG GCT<br>GAC AAA CAG AAA AAC GGT ATC AAA GCT AAC TTC<br>AAA ATC CGT CAC AAC ATC GAA GAC GGT TCT GTT<br>CAG CTG GCT GAC CAC TAC CAG CAG AAC ACC CCG<br>ATC GGT GAC GGT CCG GTT CTG CTG CCG GAC AAC<br>CAC TAC CTG TCT CAC CAG TCT AAA CTG TCT AAA<br>GAC CCG AAC GAA AAA CGT GAC CAC ATG GTT CTG<br>CTG GAA TTC GTT ACC GCT GCT GGT ATC ACC CTG<br>GGT ATG GAC GAA CTG TAC AAA |

Table 3.2: Sequence of codon-optimized PAGFP.

will differ significantly with different sequences. For this reason, a codon-optimized PAGFP was designed (https://www.idtdna.com/CodonOpt) with the hope of increasing the expression efficiency of the protein in *E. coli* (sequence listed in Table 3.2). The same cloning and expression procedures were carried out for this optimized sequence. Interestingly, the expression level of the streptavidin-optimized-PAGFP fusion protein (Figure 3.3.6 lanes 3 and 4) was indeed significantly increased—a strong band at $\sim 40$ kDa, corresponding to the fusion size, was observed after induction. Therefore, this fusion will be purified in the future for further imaging experiments.

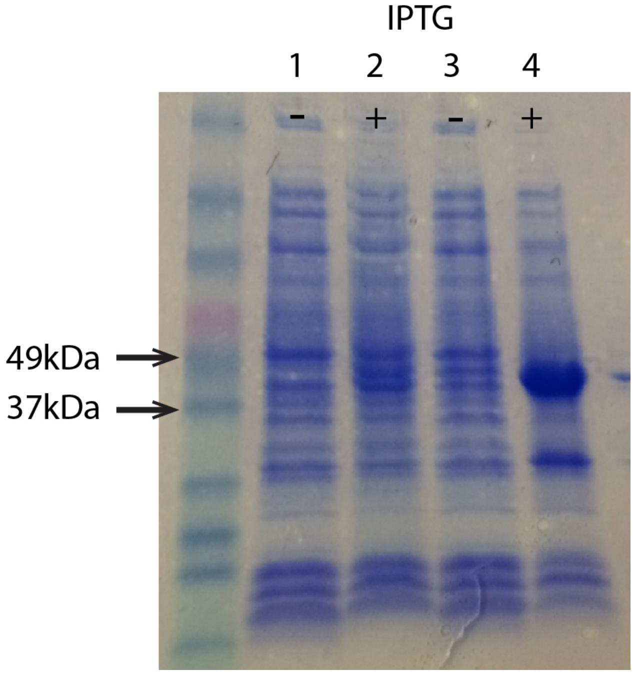

Figure 3.3.6: PAGE analysis for confirmation of the expression of streptavidin-PAGFP fusion protein and streptavidin-codon-optimized-PAGFP fusion protein. *E. coli* cells containing: streptavidin-PAGFP plasmid before (lane 1) and after (lane 2) induction; streptavidin-codon-optimized-PAGFP before (lane 3) and after (lane 4) induction.

### 3.3.4 Gold NP/FP assembly construction and characterization

Silane-PEG-biotin (600 Da, Figure 3.3.7, Nanocs Inc.) was dissolved in 95% ethanol at 50mg/mL. 200 $\mu$L silica coated gold NP (20 pM) was centrifuged at 10000 rpm for 20 min and the pellet was mixed with 50 $\mu$L silane-PEG-biotin solution.

The mixture was shaken at 200 rpm on an orbital shaker at room temperature for 3 hours to allow full conjugation. The mixture was then centrifuged at 10000 rpm for 20 min and washed with water twice. UV-vis absorption measurement before (Figure 3.3.8 blue line) and after silane-PEG-biotin modification (Figure 3.3.8 orange line) showed that the modified NPs were still well dispersed in solution and the plasmonic resonance frequency remained unchanged.

To link FPs to the modified NPs, the purified streptavidin-PAmCherry protein was mixed with the gold NPs and allowed to incubate at room temperature for 15 min. The product was centrifuged at 10000 rpm for 20 min, and free proteins in the supernatant were separated from the particle pellet. UV-vis absorption spectrum of the redispersed sample (Figure 3.3.8 yellow line) confirmed the good dispersity of the final product (no aggregation).

### 3.3.5 PALM single-molecule super-resolution imaging on single particle assembly

Gold NP/FP assemblies were immobilized on Ar-plasma cleaned coverslip (PE-50, Plasma Etch, Inc.) by drop casting. [48] 10 $\mu$L of sample was drop cast on the coverslip for 15 min before rinsing with water and blow drying with nitrogen. The sample was first imaged in dark-field mode: a broadband halogen white light source excited the sample from above through a dark-field condenser, and scattered light was collected in an Olympus IX71 inverted microscope equipped with a dark-field oil-immersion objective (NA = 0.6). The diffraction-limited image of a single NP assembly was aligned to the entrance slit of an imag-

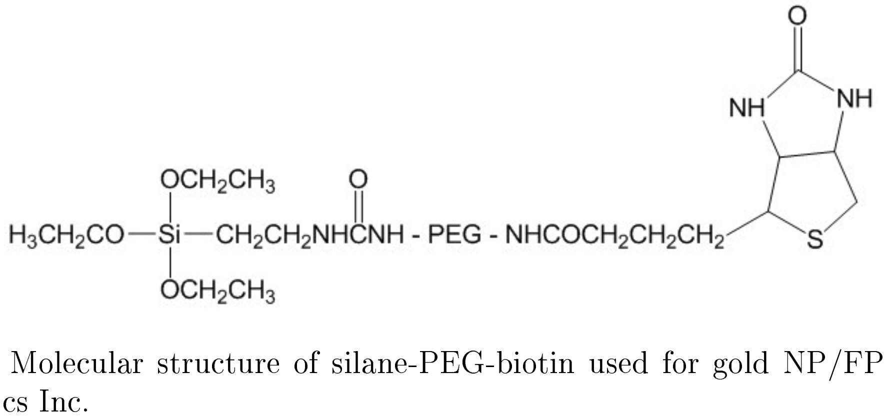

Figure 3.3.7: Molecular structure of silane-PEG-biotin used for gold NP/FP conjugation. Source: Nanocs Inc.

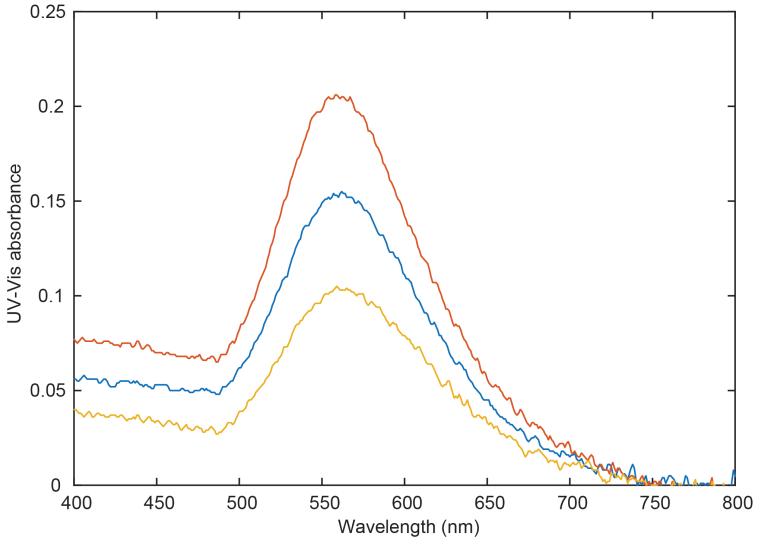

Figure 3.3.8: UV-vis absorption spectra of silica-coated gold NP (blue line), silane-PEG-biotin modified silica-coated gold NP (orange line) and fusion protein conjugated gold NP (yellow line).

ing spectrograph (Acton 2300, Princeton Instruments), and spectral data were collected on an electron-multiplying charge-coupled device (EMCCD, 2 s integration time; Andor iXon). Background spectra collected from nearby positions with no NP assembly on the spectrograph entrance slit were subtracted from measured spectra, and all data were divided by the broadband spectrum of the halogen light source and any additional neutral density filters to correct for the system spectral efficiency. In dark-field view (Figure 3.3.9A), it was found that about half of the particles observed displayed the greenish color characteristic of a single spherical gold NP (Figure 3.3.9B). Correlated scanning electron microscopy (SEM) images proved that those green particles were indeed single gold NPs (Figure 3.3.10A and B), while the yellow or orange particles were aggregates (Figure 3.3.10C and D). Therefore, all the fluorescence imaging was performed on the single NP assemblies, which were easily distinguished by color in dark-field.

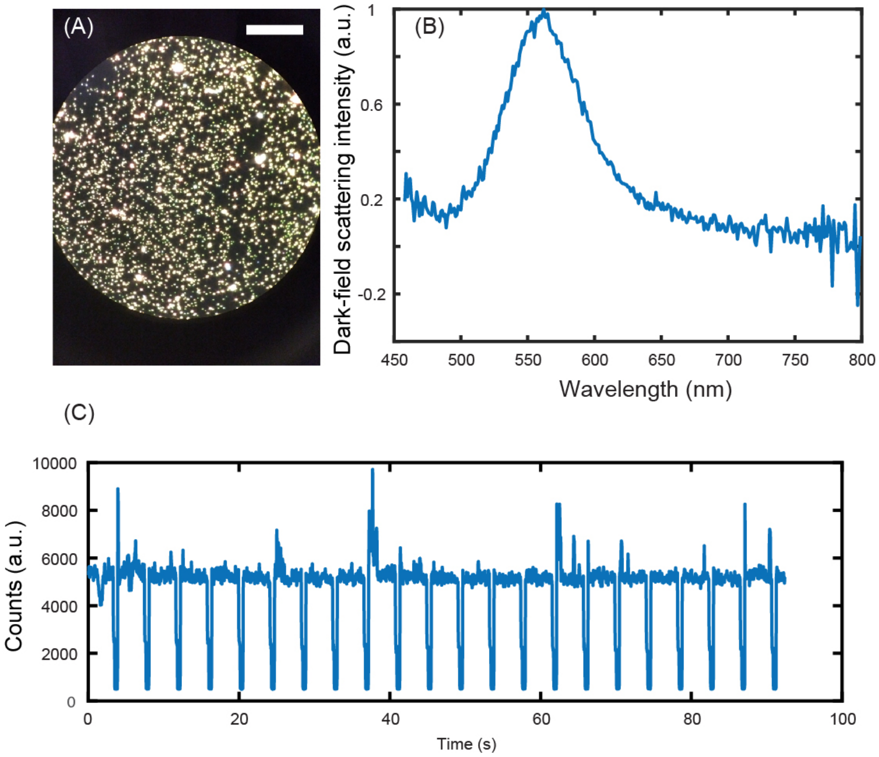

Figure 3.3.9: (A) Eye-piece view of dark-field scattering of streptavidin-PAmCherry conjugated gold NPs. The green dots correspond to single NP assemblies. Scale bar: 40 $\mu$m (B) Dark-field scattering spectrum of a protein-conjugated single gold NP. (C) Time trace of the average pixel intensity over 11 × 11 pixels around the diffraction-limited position of a gold NP/FP assembly.

Single-molecule movies were analyzed by a home-written Matlab code SMALL-LABS. Briefly, the constant fluorescence background from gold NP itself was accurately subtracted pixel-by-pixel based on identification of fluorescence on and off frames, and only the fluorescence from FPs was counted and fitted to a 2D Gaussian to extract position and intensity information (Figure 3.3.9C). To quantify the fluorescence enhancement from plasmon-coupling, non-coupled FPs were also analyzed using the same algorithm. Specifically, streptavidin-PAmCherry solution was directly drop cast on coverslip and activated so that sparse single molecules were excited and imaged.

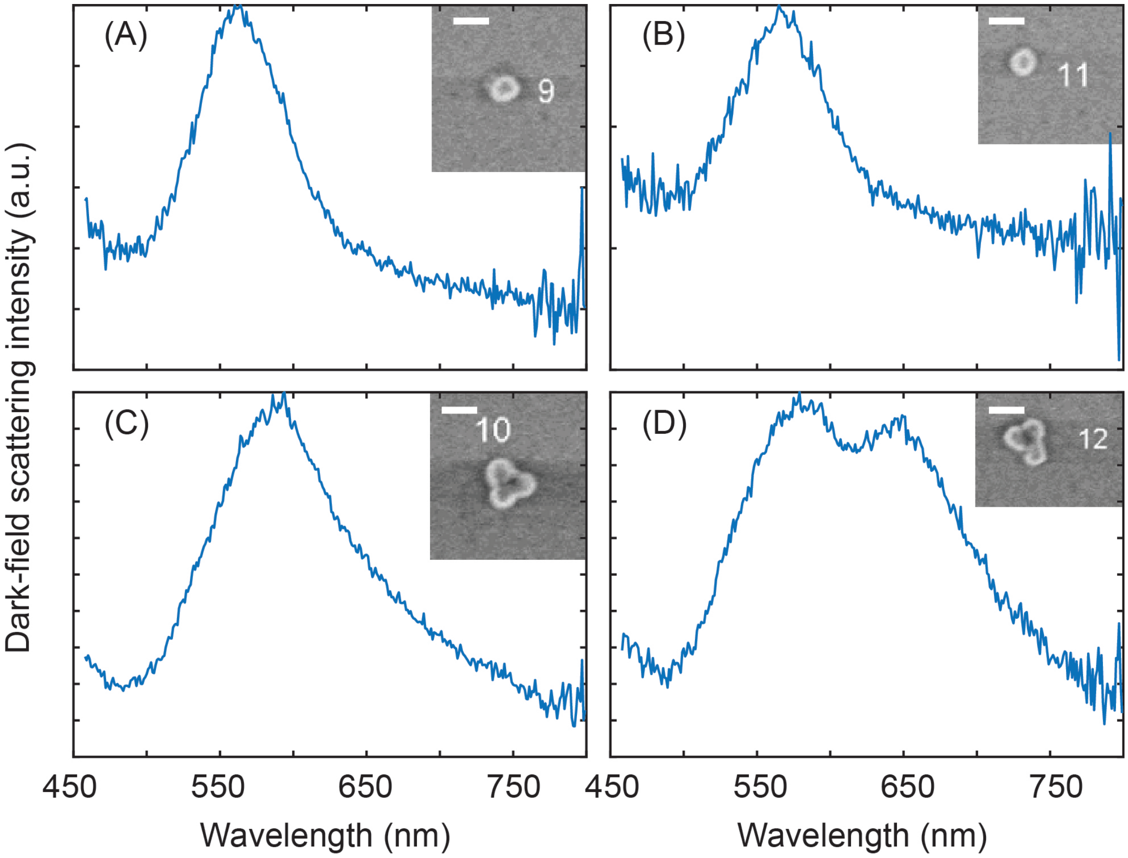

Figure 3.3.10: Dark-field scattering spectra of gold NP/FP assemblies with different color in dark-field and the correlated SEM image. (A) and (B): green particles are indeed single spherical gold NPs of the expected size. (C) and (D): orange/yellow particles in dark-field, which are easily distinguishable, are confirmed to be aggregates. Scale bar: 100 nm.

Preliminary results are shown in Figure 3.3.11. Firstly, it is important to note that by using single-molecule imaging, we can actually map out the distributions of molecule intensities or any other investigated properties. FP molecules even without coupling showed an intrinsic heterogeneity in fluorescence intensity with a finite width in the histogram (Figure 3.3.11, pink histogram). This information was not accessible from the ensemble average through bulk experiment and demonstrated the power of single-molecule technique. When coupled to gold NPs with a 20 nm silica shell spacer, the intensity distribution was clearly shifted to

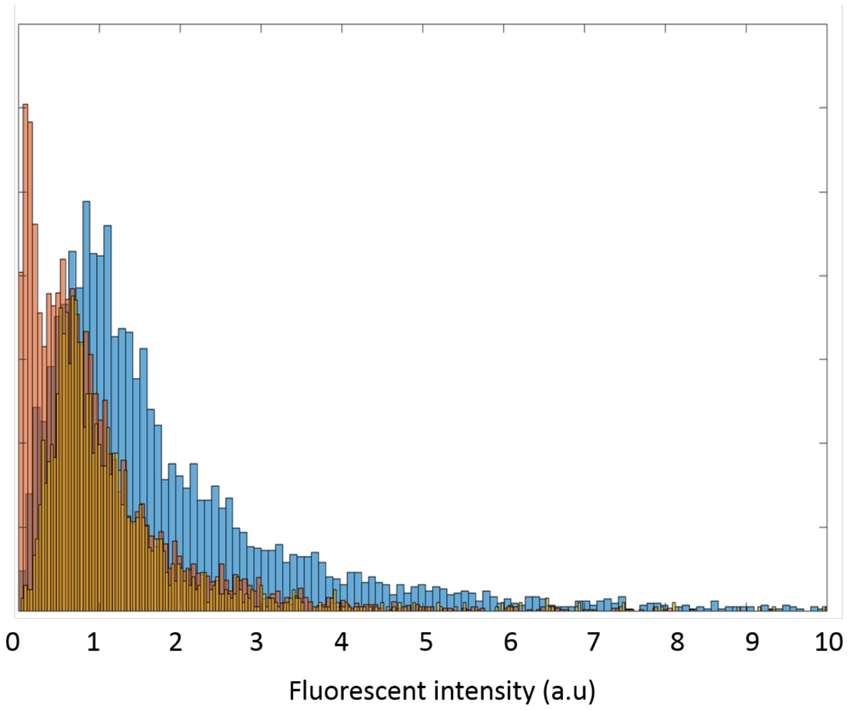

Figure 3.3.11: Distributions of the intensity of single PAmCherry protein molecules coupled to gold NPs with 20 nm silica shell spacer (blue), 80 nm silica shell spacer (yellow) and not coupled (pink).

increased brightness. The average of all the molecules in the two histograms was increased ∼ 2-fold after coupling to the NPs. Secondly, it is particularly interesting to note that the entire distribution shifts as a whole without changing the overall shape of the distribution (Figure 3.3.11, blue histogram), with only the width of the distribution slightly broadened. These differences seem to indicate that all the molecules investigated here were actually equally enhanced by the plasmonic nano-antenna, which is consistent with the fact that all protein molecules were located at the same distance away from the nano-antenna. Furthermore, when the spacer thickness increases to 80 nm, well past the plasmon-enhancement regime, the molecule fluorescence intensity went back to no enhancement (Figure 3.3.11, yellow histogram). Compared with our previous study [48] and other previous ensemble work [150], where there was substantial broadening attributed to a distribution of distances and enhancement was evidenced only through the long tail in the histogram, this study shows the advantage of a symmetric geometry, where the distance was very precisely controlled and homogeneous and no uncoupled component was observed.

## 3.4 Conclusions and ongoing work

This Chapter presents work on studying the plasmon-enhanced fluorescence of photoactivatable fluorescent proteins (FPs). FPs are important labeling probes for biological imaging because they are genetically encodable. Yet, their dimmer intensity and photo stability significantly limit the achievable single-molecule imaging resolution. Coupling to plasmonic nano-antennas is an easy, economical and efficient way to enhance fluorescence of FPs [47,48] and it is important to better understand this interaction. In this Chapter, a gold NP/FP assembly was constructed to investigate the influence of distance for FPs fluorescence enhancement. The preliminary data has shown that PAmCherry can be robustly enhanced 2-fold coupled to a gold NP with 20 nm separation distance while too large distance, like 80 nm, does not have any enhancing effect. It will be interesting to compare these results for PAmCherry with other fluorescent proteins. For example, PAGFP is another interesting target for enhancement since in our lab, we found that PAGFP seems dimmer than PAmCherry and an enhanced-PAGFP would be very valuable for two color imaging.

# CHAPTER IV

# Emission mislocalization in dye-gold NP coupled system

*The work presented in this Chapter was submitted for publication as:*

Bing Fu, Benjamin P. Isaacoff, Julie S. Biteen*, "Super-Resolving the Actual Position of Single Fluorescent Molecules Coupled to a Plasmonic Nano-Antenna"

As co-authors, BPI conducted the Finite Difference Time Domain simulations for the fluorescence emission of a dye molecule coupled to a nano-antenna. All authors participated in the discussion and revision of the manuscript.

## 4.1 Abstract

Plasmonic nanoparticles (NPs) enhance the radiative decay rate of adjacent dyes and can significantly increase fluorescence intensity for improved spectroscopy. However, the NP is a nano-antenna that complicates super-resolution imaging by introducing a mislocalization between the actual position of the emitter and its super-resolved apparent emission position. The mislocalization magnitude depends strongly on the dye-NP coupling geometry. It is therefore crucial to quantify mislocalization to recover the actual emitter position in a

coupled system. Here, we super-resolve in two and three dimensions the distance-dependent emission mislocalization of single fluorescent molecules coupled to gold NPs with precise distance tuning via double-stranded DNA. We develop an analytical framework to uncover detailed spatial information when direct 3D imaging is not accessible. We measure up to 50 nm emission mislocalizations and show that smaller separation distances lead to stronger mislocalizations, also verified by electromagnetic calculations. Overall, by quantifying the distance-dependent mislocalization shift in gold NP/dye coupled systems for the first time, we show that it is possible to recover the actual physical position of a strongly coupled single emitter.

## 4.2 Introduction and motivation

Single-molecule super-resolution fluorescence imaging improves on traditional light microscopy by localizing emission below the diffraction limit and revealing information previously hidden by lower resolution and heterogeneity. [12, 14, 18] Due to high signal to noise ratios, good biocompatibility, and minimal perturbations to the system, it has been extensively applied in biological studies to map nanoscale structures [151] and reveal subcellular dynamics. [34, 42] Furthermore, super-resolution fluorescence imaging has contributed significantly to nanophotonics by enabling direct measurements of near-field light-matter interactions in a far-field microscope. [46] Upon resonant excitation, the local electromagnetic field near the plasmonic nanoparticle (NP) surface is enhanced due to the local surface plasmon resonance (LSPR). [67] Plasmonic nanomaterials can be used in the near field to engineer optical properties such as the electronic decay rates of proximal dyes. Depending on the nanostructures and fluorophores, significant enhancements up to tens of thousands-fold [94] or, conversely, quenching at short separation distances, are observed, and the distance- and wavelength-dependence has been studied. [48, 118, 134] Plasmonic enhancement is particularly useful in ultra-sensitive detection [152] and enhanced solar cell light harvesting, [153] and has recently shown promise for enhanced-resolution single-molecule cellular imaging. [80, 101]

However, though fluorescence enhancement has been well characterized experimentally and with electromagnetic calculations, a critical gap remains in our understanding of the dye-NP coupling: because of the increased local density of optical states, far-field microscopy detects an apparent fluorescence emission position that deviates significantly from the actual molecule position. Furthermore, though fluorescence enhancement occurs only over distances of ∼10 - 20 nm, this "emission mislocalization" phenomenon has been detected for molecules much farther away from the NP [46, 100] and for a wide variety of nano-antennas. [46, 49, 100, 154] Therefore, despite the fluorescence enhancement, mislocalization obfuscates the location of a plasmon-coupled fluorescent molecule and has prevented accurate plasmon-enhanced single-molecule super-resolution imaging.

Thus, as the super-resolution imaging community strives for brighter metal-enhanced probes, this newly recognized problem of mislocalization is of great concern. [97–99] For instance, dye molecule emission is strongly coupled into plasmonic nano-antennas, even at a separation distances up to 90 nm. [46,49,98] Because experimental NP-fluorophore separation distances have been broadly distributed due to randomly positioned dyes or asymmetric nanostructures, [46, 49, 98–100] no previous study was able to quantify this mislocalization effect in the tens of nanometers regime relevant to plasmonic enhancement. This article provides, to our knowledge, the first quantitative map of mislocalization information, which enables us to recover the actual emitter position from the plasmon-coupled system.

Here, we understand the emission mislocalization from plasmon-coupled dye molecules by constructing perfectly symmetric assemblies of spherical gold NPs conjugated with ATTO532 dyes through rigid, tunable double-stranded DNA (dsDNA) spacers. The apparent emission positions of all dye molecules are super-resolved by dSTORM (direct Stochastic Optical Reconstruction Microscopy). [15, 16, 155, 156] In this system, we correlate these apparent emission positions with the actual known dye positions to reveal the amount of localization distortion. Firstly, 3D super-resolution imaging reveals qualitative mislocalization in larger symmetric nanoassemblies. Then 2D imaging characterizes smaller nanoassemblies with stronger radiative LSPR modes, and we use statistical simulations to uncover information that is obscured by 2D projections. Overall, in our measurements of dyes coupled to an 80 nm gold NP, we observe 46 nm mislocalizations for 33 nm spacers, and at least 30 nm mislocalizations for 23 nm spacers. Electromagnetic calculations reproduce the mislocalization effect, but predict an even more obvious distance dependence. Also, calculations reveal properties which are not distinguishable in experiments: emission mislocalization changes as a function of the dye dipole orientation and axial position. Overall, this article provides experimental and computational measurements of the distance-dependent emission mislocalization of single dye molecules near nano-antennas to enable applications of accurate plasmon-enhanced single-molecule imaging.

## 4.3 Experimental methods

### 4.3.1 NP Assembly Samples.

The protocol was slightly modified from previously published methods. [157, 158] First, thiolated single-stranded DNA (ssDNA) was mixed with complementary ATTO532 labeled ssDNA and hybridized at 95°C for 2 min followed by 1 hour incubation at room temperature. [157] Then 0.1 M dithiothreitol (DTT) (final concentration) and 0.2 M phosphate buffer (pH = 8.0) were combined with the dsDNA to reduce the disulfide group. [159] An Illustra NAP column (GE Healthcare Life Sciences) was used to clean up the reduced dsDNA sample. 200 nm and 80 nm gold NPs (nominal sizes, BBI Solutions) were immediately mixed with an excess of dsDNA and the mixture was incubated $>$ 16 hours while gently shaking (at 60 Hz) to ensure high-yield conjugation. [160] The sodium chloride concentration in the buffer was then gradually brought up to 0.5 M to increase the loading yield of dsDNA on the NPs, and the sample was incubated overnight at room temperature while gently shaking. [158,160] Finally, we centrifuged the conjugated particles at 10,000 rpm for 20 min three times to remove unconjugated DNA, and the final pellet was dispersed in deionized water for future imaging.

For imaging immobilized NP/ATTO532 assemblies on a microscope coverslip, NPs modified as described above were diluted 10-fold and 10 $\mu$L of the dilute suspension was dropped cast on a Ar plasma-cleaned (200 mTorr, 15 min, PE-50, Plasma Etch Inc.) coverslip. The NP suspension was allowed to sit on the surface about 15 min before rinsing and air drying.

To measure the NP assemblies sizes using dynamic light scattering (DLS), gold NP samples were diluted to about 1 mL in water for DLS measurements (Malvern Zetasizer Nano - ZS). First, bare small (80 nm) gold NPs without any DNA modification were measured to get the actual NP size. Then, gold NP/dye assemblies were measured and the DNA lengths were calculated by subtracting the measured gold NP size. For the large (200 nm) gold NPs, the broader distribution in DLS makes the estimation of DNA lengths less accurate. Thus, bare large gold NPs without any DNA modification were measured to get the actual size, then we used the DNA lengths measured from the smaller NPs for the larger NPs.

### 4.3.2 Single-Particle Dark-Field Scattering Spectroscopy.

Modified NPs immobilized on a coverslip were immersed in dSTORM buffer (0.5mg/mL glucose oxidase, 40$\mu$g/mL catalase, 10% w/v glucose, 10mM methylethylamine) for dark-field scattering measurements. A broadband halogen white light source excited the sample through a dark-field condenser, and scattered light was collected in an Olympus IX71 inverted microscope equipped with a dark-field oil-immersion objective (NA = 0.6). The diffraction-limited image of a single NR was aligned to the entrance slit of an imaging spectrograph (Acton 2300, Princeton Instruments), and spectral data were collected on an EMCCD (4 s integration time; Andor iXon). Background spectra collected from nearby positions with no NR on the spectrograph entrance slit were subtracted from measured spectra, and all data were normalized by the broadband spectrum of the halogen light source and any additional neutral density filters to correct for the system spectral efficiency.

### 4.3.3 dSTORM experiments.

First, the dark-field scattering image was used to distinguish the single NP/ATTO532 assemblies (green color in dark-field) from any possible dimers or large clusters (orange or red color). Epifluorescence imaging was performed on single particles one at a time with a 100×1.3NA oil-immersion objective in an Olympus IX71 inverted microscope (Figure 4.4.2a, inset). Samples were excited with circularly polarized 515 nm laser light (Spectra-Physics Excelsior 515 nm and Tower Optical Z-10-A-.250-A-514.5 quarter wave plate) with intensities of ~36.4 W/mm$^2$ for 80 nm NPs and ~79.3 W/mm$^2$ for 200 nm NPs. In dSTORM buffer, the dye molecules appeared on and off stochastically therefore allowed the super-resolution localizations from a single molecule. Reference experiments on DNA-coated NPs without dye molecules showed no significant fluorescence emission bursts over this flat background and the buffer is indeed responsible for stochastic blinking (Figure 4.4.5). Single-molecule analysis of intensity traces as in Figure 4.4.2b were ensured by adjusting the laser intensity to favor single-molecule bursts, and by excluding any rare two-step bleaching from the analysis, which indicates simultaneous emission of multiple molecules (Figure 4.4.6). The single-molecule emission events were not expected to have a constant intensity due to the different possible dipole orientations they may possess, as well as rapid blinking kinetics in the dSTORM buffer.

Fluorescence emission was filtered appropriately (Semrock LPD01-514R/BLP01-514R-25) to maximize signal and minimize scattered laser light and then imaged on a 512 pixel × 512 pixel Andor iXon EMCCD (1 camera pixel = 49 nm in the imaging plane) at 20 or 40 ms/frame for 200 s. The center of the NP (red cross in Figure 4.4.2e) was obtained by fitting the single-NP emission in 20 off-frames. Apparent emission positions of all dye molecules were combined into one map by registering relative to the NP center positions. The localization density was calculated as number of localizations per certain area, which was consistent throughout all the analysis.

For 3D localizations, a 3D calibration curve was first obtained by imaging fluorescent TetraSpeck polystyrene beads (Invitrogen TetraSpeck Microsphere, $0.2\mu$m) with a cylindrical lens (Thorlabs Inc. LJ1144RM-A, f = 500 mm) in the emission pathway. [161] The beads were diluted 10-fold and drop cast on a coverslip to provide isolated single emitters. 5 $\mu$L glycerol was sandwiched between the substrate and another coverslip before the sample was imaged. The z-position of the samples was tuned in 50-nm steps by a piezo stage (PI E-709 Digital Piezo Controller) and the fluorescence image was taken at each $z$-position. By fitting the PSF to a 2D asymmetric Gaussian function, a calibration curve that plotted the long-axis and short-axis Gaussian widths as a function of $z$-position was obtained and used to extract the $z$-positions of each localization in 3D imaging experiments (Figure 4.4.7).

### 4.3.4 Statistical Simulations.

Positions on the surface of a sphere were randomly sampled with the Matlab function RandSampleSphere (Matlab File Exchange). True imaging conditions are replicated by adding noise in the positions according to the experimentally characterized 2D localization precision (± 22 nm; Figure 4.4.12), and by simulating 150 detected molecules. These simulated imaging data were translated into curves of single-molecule localization probability. The precise peak positions come from fitting the peak region of each curve to a Gaussian function (Figure 4.4.16).

### 4.3.5 FDTD Calculations.

Electromagnetic simulations were performed using the Lumerical FDTD Solutions software package. The real sample geometry was considered (Methods), and the scattering spectrum was computed by exciting the NP from above with a broadband plane wave and measuring the scattered power in the far-field through a numerical aperture, NA = 0.6, as in the dark-field measurements. Apparent emission positions were calculated by exciting the NP with a broadband point dipole source (constant current). The radiation propagating downward from the NP (into the glass) was projected to the far-field and focused through a lens with numerical aperture, NA = 1.3, as in experiments. This far-field image was fit to a symmetric 2D Gaussian to determine the apparent position of the emission, as previously described. [49]

To compute the emission from all molecular positions in the experimental system, the dipole source was placed at 25 or 45 different locations (for the 78.6 nm and 179 nm spheres, respectively), along a vertical circular arc in the $xz$ plane at $y = 0$ around the NP located the origin; the simulated points were mapped onto all possible experimental points by symmetry (Methods). The arc radius was the radius of the NP plus the length of the DNA spacer (11 nm, 22.8 nm, or 32.6 nm). The dipole positions were angularly spaced equally starting directly below the NP at the glass interface and ending directly above the NP (Figure 4.4.19a). At each location, three simulations were performed, each with the dipole oriented along a different Cartesian direction ($x, y$, or $z$). Because the NP and the dipole source were both located in the same $xz$ plane, and because the 2D localization procedure used only returns the $(x, y)$ positions, only the fitted $x$ position was kept; deviations from $y = 0$ were small enough ($< 1$ nm) to be ignored for simplicity. In FDTD calculations, we assume that the dye molecule dipoles were randomly oriented and remained stationary during a single imaging frame (40 ms); therefore the calculated results in Figure 4.4.19 are the average of all three possible orientations weighted by their calculated fluorescence enhancement. [162]

Though DLS measurements showed expected size differences for NPs conjugated with dsDNA of various lengths (Figure 4.4.1), the dark-field scattering spectra of all the samples was the same regardless of DNA modification or the spacer length (Figure 4.4.3). This result indicates that the dsDNA layer was probably not dense enough to affect a visible peak shift. Therefore, we modeled the spacer layer with the refractive index of water in FDTD calculations.

In our calculations, DNA-modified gold NPs were modeled as gold spheres with a diameter determined from DLS measurements (Table 4.3). The gold sphere was located above a glass coverslip at a distance given by the length of the dsDNA spacer (11.0 nm, 22.8 nm, and 32.6 nm), and the halfspace above the coverslip surrounding the sphere was water. Refractive index data for gold was taken from Johnson and Christy, [130] glass was set to a dispersionless value of $n = 1.51$ and $k = 0$, and water was set to $n = 1.33$ and $k = 0$.

To match experiments where emitting, fluorescent dyes are located anywhere on the surface of a spherical shell of DNA linkers about a NP sphere, the arc of simulated emitters were mapped onto all other azimuthal angles using the following procedure. First, the simulated $x$ position and the corresponding mislocalization (only the $x$ position was mislocalized; Figure 4.4.21d) were interpolated to a higher density to allow better sampling. Points were then selected from a collection of $(x, y)$ points generated from random points on the surface of a sphere projected to the $xy$ plane using RandSampleSphere (Matlab File Exchange). At each point, the radial distance was calculated and used to match a simulated $x$ position (50% were taken from the top half of the sphere and 50% from the bottom half due to the degeneracy in 2D imaging). The selected $(x, y)$ position was then shifted along the radius by the (positive or negative) distance given by the $x$ mislocalization of the original point. In this way, all possible $(x, y, z)$ positions on the surface of the spherical shell determined by the sphere with the DNA linker were generated based on the results from just the circular arc in the $xz$ plane.

## 4.4 Results and discussions

### 4.4.1 Gold NP/dye assembly preparation and characterization.

To measure the distance dependence of dye/NP interactions in a symmetric assembly, we modified spherical gold NPs with a monolayer of rigid dsDNA linked to ATTO532 dye molecules at the other end; the DNA length was tunable from 10 to 90 base pairs (nominal

| Nominal Gold NP size (nm) | DLS Gold NP size (nm) | DNA base pair (bp) | Sequence | Nominal ds-DNA (nm) | DNA DLS (nm) |
|---|---|---|---|---|---|
| 80 | 78.6 | - | - | | |
| 80 | 78.6 | 10 | /5ThioMC6-D/CT TGC CAT CG | 3.4 | 3.5 |
| 80 | 78.6 | 30 | /5ThioMC6-D/CT TGC CAT CGC TAG TAC ATG GCA CTG ACT G | 10.2 | 11.0 |
| 80 | 78.6 | 74 | /5ThioMC6-D/CT TGC CAT CGC TAG TAC ATG GCA CTG ACT GAA AGT ACA CGG CTA TCA TGC CGC GAT ACC TGC ATA CCT TTA ACG | 25.2 | 22.8 |
| 80 | 78.6 | 90 | /5ThioMC6-D/CT TGC CAT CGC TAG TAC ATG GCA CTG ACT GAA AGT ACA CGG CTA TCA TGC CGC GAT ACC TGC ATA CCT TTA ACG CAT AAC TGA GCA CTG G | 30.6 | 32.6 |
| 200 | 179.1 | - | - | - | - |
| 200 | 179.1 | 30 | /5ThioMC6-D/CT TGC CAT CGC TAG TAC ATG GCA CTG ACT G | 10.2 | 11.0 |
| 200 | 179.1 | 90 | /5ThioMC6-D/CT TGC CAT CGC TAG TAC ATG GCA CTG ACT GAA AGT ACA CGG CTA TCA TGC CGC GAT ACC TGC ATA CCT TTA ACG CAT AAC TGA GCA CTG G | 30.6 | 32.6 |

Table 4.3: Summary of all the DNA spacers used. Sequence and measured data are listed.

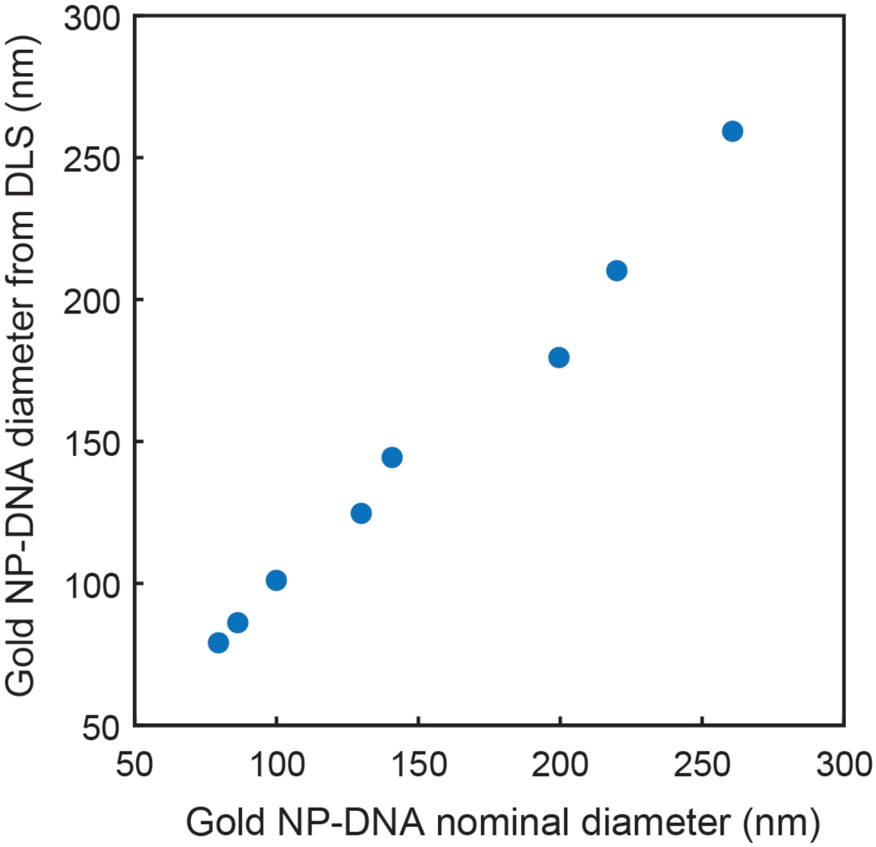

Figure 4.4.1: DLS measurement of gold NP/dye assemblies versus nominal values. First five points: 80 nm diameter gold NPs with no DNA, 3.5 nm DNA, 11.0 nm DNA, 22.8 nm DNA, and 32.6 nm DNA, respectively; last 3 points: 200 nm diameter gold NPs with no DNA, 11.0 nm DNA, and 32.6 nm DNA, respectively.

lengths: 3.4 - 30.6 nm). Dynamic light scattering (DLS) of the NP/dye assemblies in aqueous solution confirmed success of modification (Figure 4.4.1, Table 4.3, Methods), and the measured assembly sizes correlated well with the nominal 0.34 nm per base pair, which verifies that the dsDNA spacers are rigid in this length regime. [163] Single NP/dye assemblies were drop-cast onto a glass coverslip (Figure 4.4.2a, right inset). The dark-field spectra of individual NP/dye assemblies (blue lines in Figure 4.4.2a and Figure 4.4.3) show a resonance peak that overlaps with the fluorescence emission peak of ATTO532 (pink line), which is one of the conditions for plasmon-enhanced fluorescence. [105, 133] Finite-difference time-domain (FDTD) electromagnetic calculations of the NP/dye assemblies predicted plasmon resonances consistent with experiments (black line in Figure 4.4.2a and Figure 4.4.3).

### 4.4.2 dSTORM super-resolution imaging of mislocalized emission from dye molecules near plasmonic NPs.

Single NP/dye assemblies were illuminated at 515 nm, which excited both the dye molecules and the NP plasmon mode, and were imaged in dSTORM buffer, [15,16,155] which switched ATTO532 dye molecules on and off stochastically to enable single-molecule microscopy. The drop-cast dye/NP assemblies were dispersed to allow single-particle experiments, and the assemblies stayed stationary during imaging (Figure 4.4.4). The intensity time trace for the dyes on a single NP (averaged over a 450 × 450 nm imaging area about the NP center position) showed bursts of emission from the photoswitched molecules and a constant-intensity NP fluorescence background (Figure 4.4.2b). [48] The off-frames (background from constant low-intensity fluorescence from the NP only) were distinguished from the on-frames (single dye molecule bursts) in the raw data with the STaSI change-point finding algorithm (red lines in Figure 4.4.2c,d) [164] and the average background image from the nearby off-frames was subtracted from each on-frame. The dots in Figure 4.4.2e show 38 successive $(x, y)$ localizations of a single ATTO532 dye molecule positioned 32.6 nm (red circle) from the surface of an 80 nm diameter (diameter from DLS: 78.6 nm) gold NP (black circle). The dot colors represent the localization densities. It is interesting to note that, though the apparent emission positions are shifted inward from the actual emitter positions, [46] the average emission position is not at the NP center. Thus, though the dye molecules are strongly coupled to

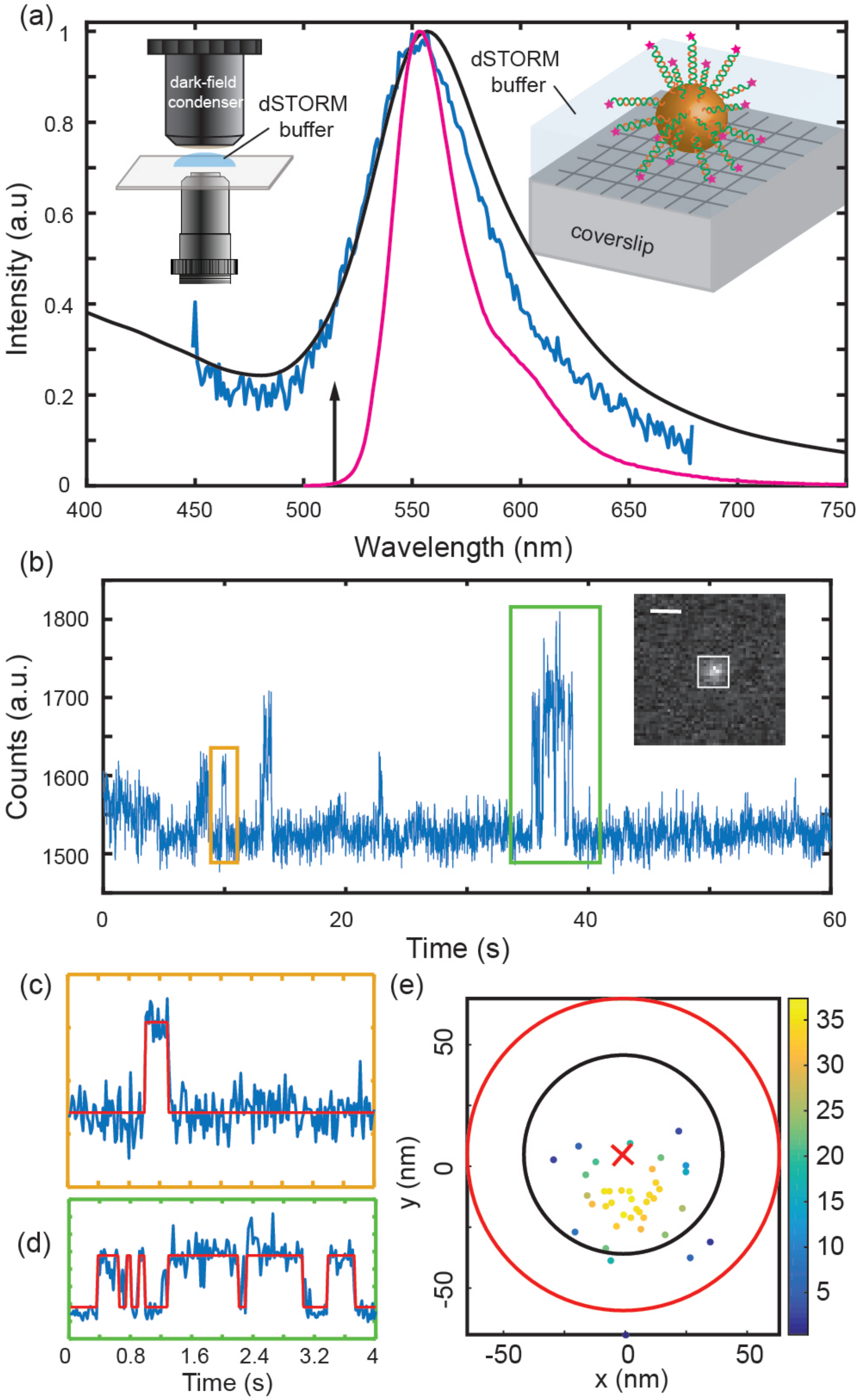
(a)
Intensity (a.u)
Wavelength (nm)
1
0.8
0.6
0.4
0.2
0
400
450
500
550
600
650
700
750
dark-field condenser
dSTORM buffer
dSTORM buffer
coverslip
(b)
Counts (a.u.)
Time (s)
1800
1700
1600
1500
0
20
40
60
(c)
(d)
0
0.8
1.6
2.4
3.2
4
Time (s)
(e)
y (nm)
x (nm)
50
0
-50
-50
0
50
35
30
25
20
15
10
5

Figure 4.4.2:

Figure 4.4.2: dSTORM Data analysis. (a) Measured (blue) and simulated (black) dark-field scattering spectra of a single 80 nm NP modified with 11 nm dsDNA-ATTO532; fluorescence emission spectrum of dsDNA-ATTO532 (pink line) excited at 515 nm (arrow). Inset: microscope and sample geometry. (b) Mean fluorescence intensity (over 450 × 450 nm, inset white box) vs. time for a single 80 nm NP/dye assembly with 32.6 nm dsDNA linkers. Scale bar: 500 nm. (c, d) Magnification of the orange and green boxes in 'b', respectively. Red lines: change point algorithm curve fitting. (e) Super-resolved emission from a representative molecule. Each dot is the localization of the same single molecule in one imaging frame. Color bar: density of localizations. Black circle: 80 nm NP diameter; red circle: actual dye molecule positions with 22.8 nm dsDNA spacer; red cross: geometric center. All localizations are mislocalized from the outer circle toward the NP center.

the plasmonic NP, the extent of coupling, which is a function of separation distance, can be measured in terms of mislocalization distance with single-molecule imaging.

### 4.4.3 3D imaging of NP-coupled dye molecules.

To overcome the limitation of conventional super-resolution images, which provide only the 2D apparent dye emission positions, we super-resolved the 3D positions of single molecules based on astigmatism through a cylindrical lens. [161] The alignment was calibrated with fluorescent beads (Figure 4.4.7). [161] Due to the 60-nm axial ($z$) precision (Figures 4.4.8 and 4.4.12), we investigated larger 200 nm gold NPs (diameter from DLS: 179 nm) modified with dsDNA-ATTO532 of length 11.0 nm or 32.6 nm (Figure 4.4.1). The dipole plasmon resonance mode at about 580 nm (Figure 4.4.9) had spectral overlap with the dye fluorescence emission. The 3D super-resolution localizations and fluorescence intensities for each single-molecule with dsDNA spacers of 11.0 nm or 32.6 nm are mapped out in Figure 4.4.10a and d, respectively.

3D imaging avoids the $z$-position ambiguity in 2D imaging. We selected the central slice of the NP/dye assembly (blue rectangles in Figures 4.4.10a,d) by plotting all apparent

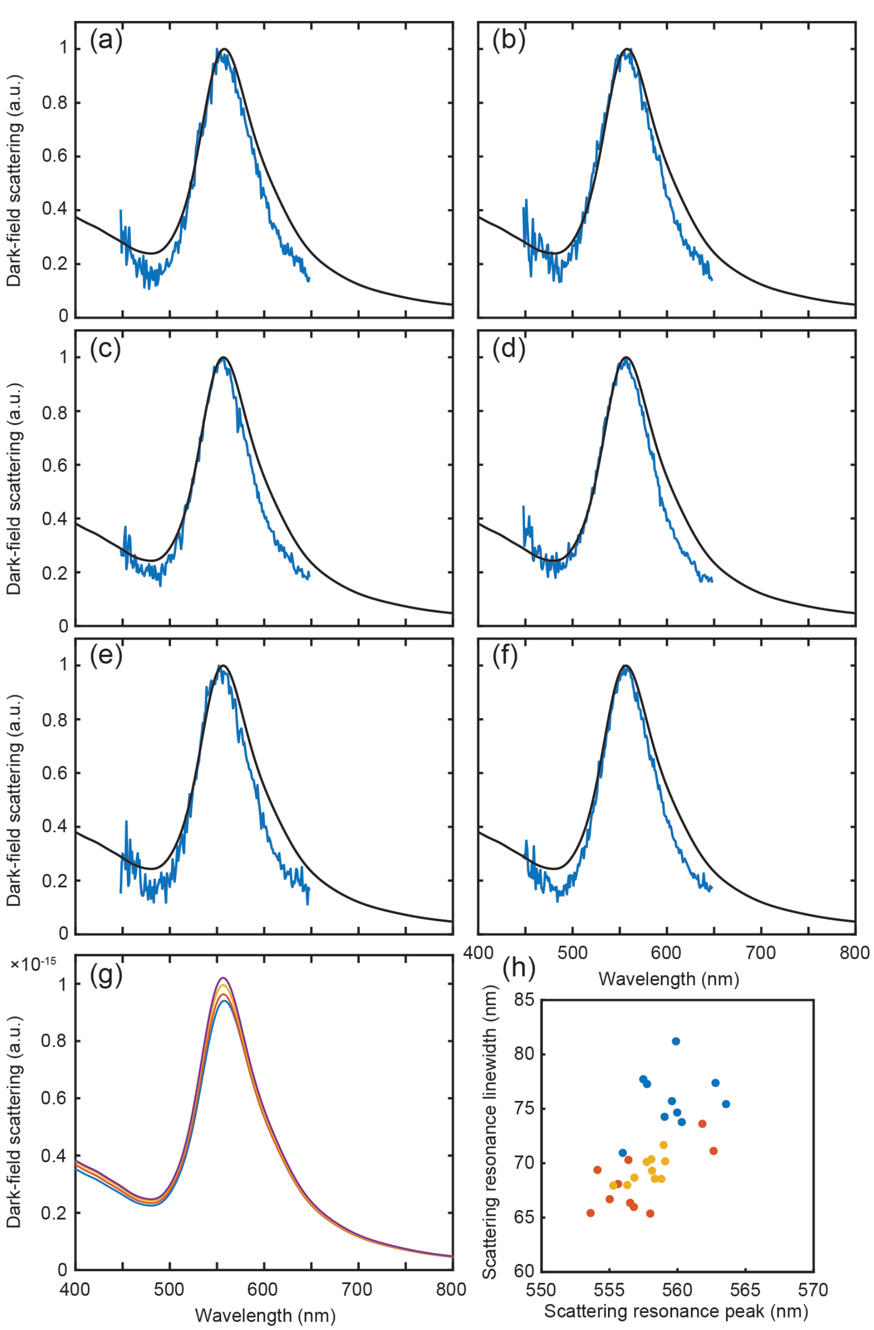
(a)
(b)
(c)
(d)
(e)
(f)
(g)
(h)
Dark-field scattering (a.u.)
0
0.2
0.4
0.6
0.8
1
×10⁻¹⁵
400
500
600
700
800
Wavelength (nm)
Scattering resonance linewidth (nm)
60
65
70
75
80
85
550
555
560
565
570
Scattering resonance peak (nm)

Figure 4.4.3:

Figure 4.4.3: (a-f) Blue lines: representative dark-field scattering spectra of 80 nm gold NPs and gold NP/dye assemblies. (a,b) NPs without DNA modification. (c,d) NP/dye assemblies with 11.0 nm spacers. (e,f) NP/dye assemblies with 22.8 nm spacers. (g) FDTD calculations of the scattering spectra of assemblies with different spacer lengths. From top to bottom: no DNA modification; 11.0 nm; 22.8 nm and 32.6 nm. Normalized plots of these computational curves are overlaid in black in panels ’a’ - ’f’. (h) Dark-field scattering peak positions of representative NP/dye assemblies. Blue: no DNA modification. Orange: 11.0 nm spacer. Yellow: 22.8 nm spacer.

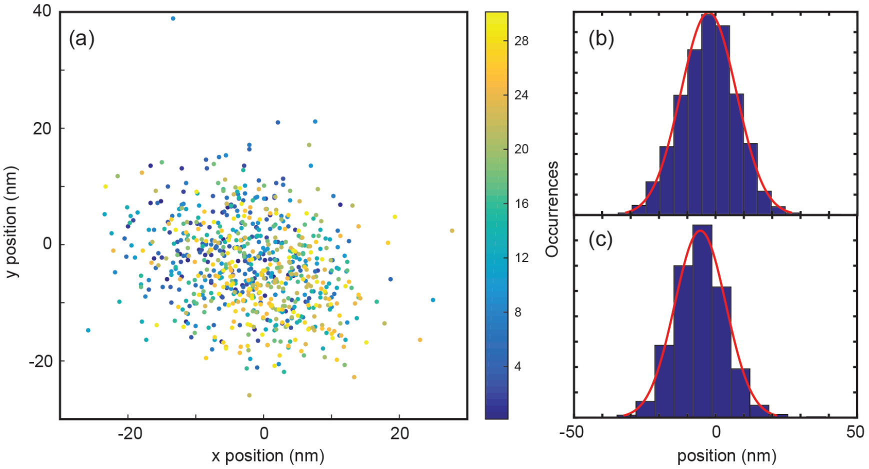

Figure 4.4.4: (a) Sequential localizations of a gold NP from its fluorescence image. No significant drift is observed over the course of 30 seconds (colorbar: time in s). (b) The localization precision is 9.3 nm along the $x$ axis and (c) 8.8 nm along the $y$-axis.

$xy$ emission positions with $z$ in the range of $-75$ nm to $+75$ nm in Figures 4.4.10b,e for 11.0 nm and 32.6 nm spacer distances, respectively. For comparison, localizations that fall outside this central slice (green rectangles in Figure 4.4.10a,d) are plotted in Figure 4.4.10c,f. All projected localization slice maps are color coded by the normalized average localization density at that radius; this relative number of localizations provides the distribution of the apparent positions: the densest areas (yellow) represent the area with the highest probability of emission events.

Choosing the central slice reduces the NP/dye assembly from a 3D sphere to a disc: these

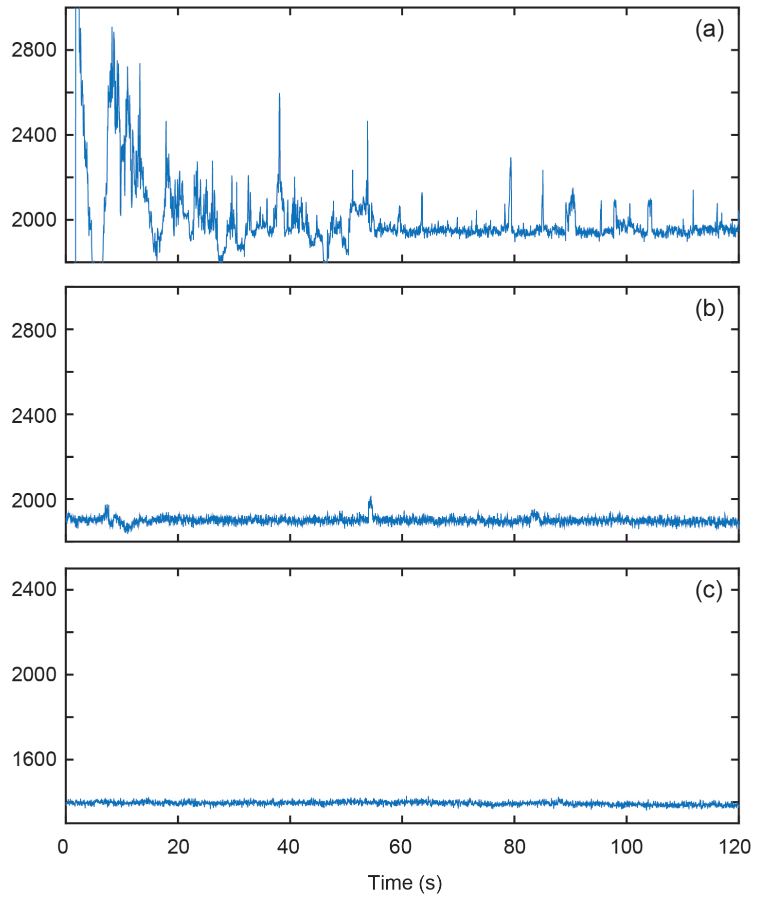

Figure 4.4.5: Time trace of fluorescence intensity averaged over the 450 nm × 450 nm area around the center of a gold NP assembly. (a) NP/dye assembly in dSTORM buffer. The expected stochastic blinking from single dye molecules is observed. (b) NP/DNA (no dye) in dSTORM buffer. Only occasional fluorescence signals are observed; these bursts are very weak and can be distinguished from the real signals in 'a' by applying a threshold. (c) NP/dye assembly in water after photobleaching. Without dSTORM buffer, no blinking is observed.

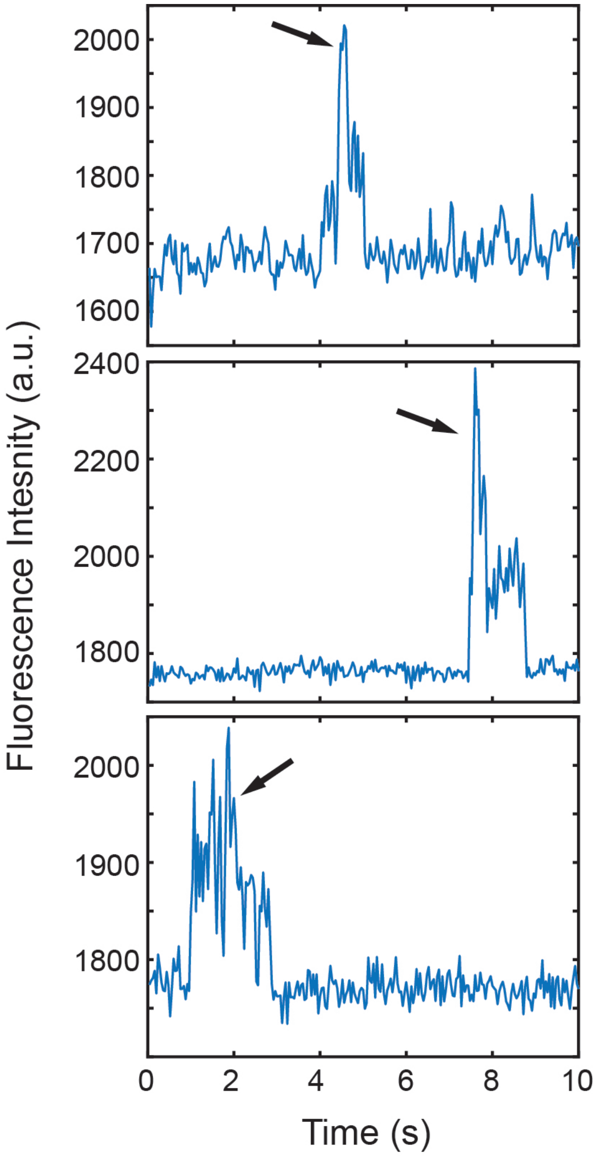

Figure 4.4.6: The dSTORM imaging conditions are optimized to produce single-molecule bursts. Rare multiple-molecule fluorescence signals show two-step photobleaching (black arrows); these signals are excluded in analysis.

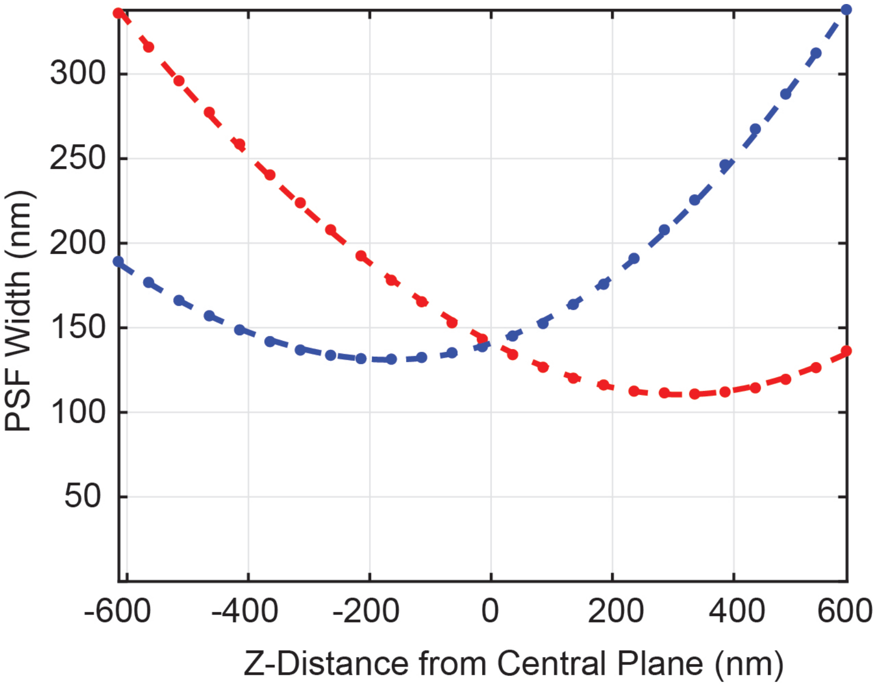

Figure 4.4.7: 3D imaging calibration curve obtained by imaging an immobilized 200 nm fluorescent TetraSpeck polystyrene bead with an objective positioner. Blue: $x$-width; red: $y$-width. For a given signal, the $z$-position is determined from the PSF widths in the $x$- and $y$-directions.

molecules are arranged in a circle (red circle in Figures 4.4.10b,e) some distance away from the gold NP surface (black circle in Figures 4.4.10b,e). It is therefore notable that the most probable apparent molecule positions (yellow areas in Figures 4.4.10b,e) are significantly shifted from the red circle toward the NP for both spacer lengths. Here, because we are measuring the apparent emission positions from molecules on a circle and not the 3D surface of a sphere, it is reasonable to draw conclusions about the mislocalization distance based on the apparent position maps. With the 11.0 nm dsDNA spacer, we observed a wide ring-shaped localizations distribution (Figure 4.4.10b) consistent with a radially symmetric shift of the ATTO532 dyes toward the gold NP. The highest density appears about 80 nm away from the NP center (Figure 4.4.11). This ∼20 nm mislocalization shift shows the effect of

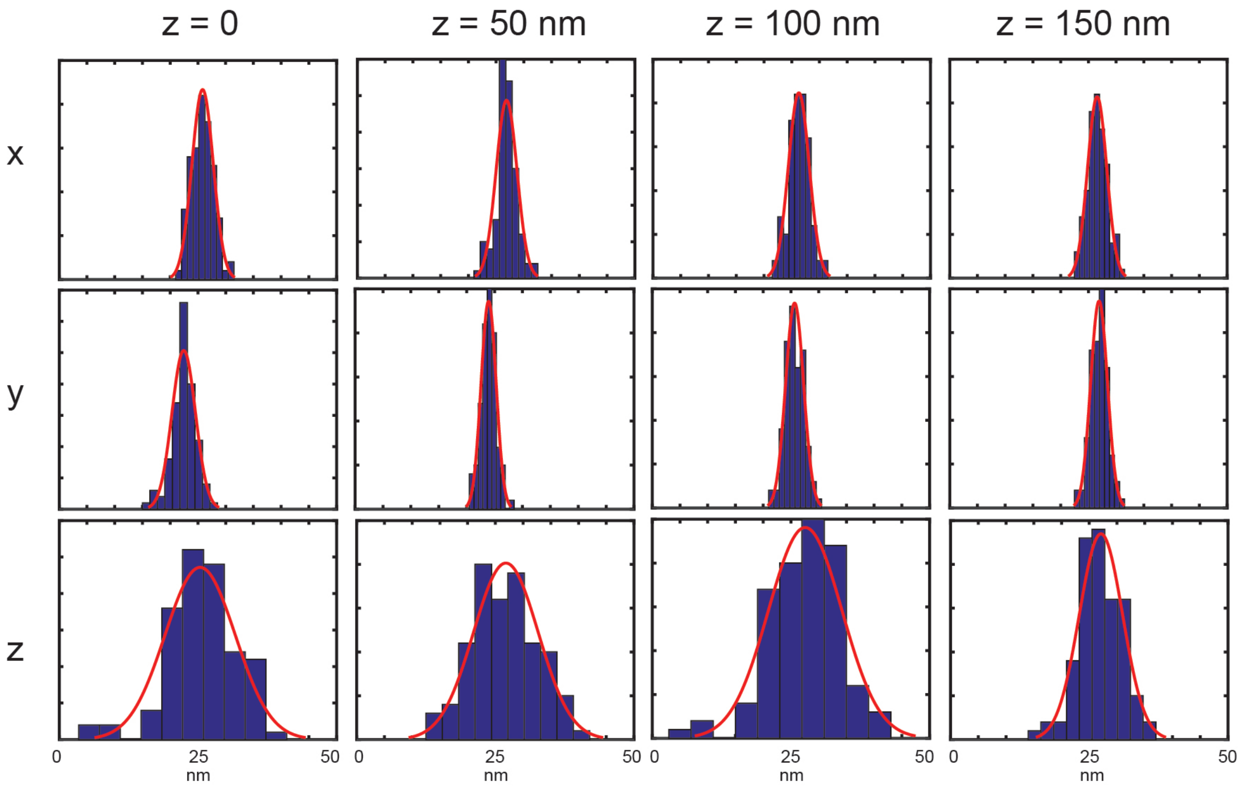

Figure 4.4.8: 3D localization precisions of an immobilized TetraSpeck bead at different $z$-planes. The in-plane ($x$-and $y$-axis) precisions are ∼3 times better than the axial ($z$-axis) precision.

dye/NP coupling.

In contrast, the map combining the slices from above and below is generated from the same NP/dye assembly and with the same analysis parameters (Figure 4.4.10c), but shows a very different distribution: the highest apparent emission position is tightly concentrated at the NP center. This central localization position is consistent with the fact that these slices include molecules located near the top and bottom poles of the dye/NP assembly —in the $xy$ plane, the actual positions of those molecules are near the NP center and no significant mislocalization is predicted. Similarly, for the longer (32.6 nm) spacers, we also observed

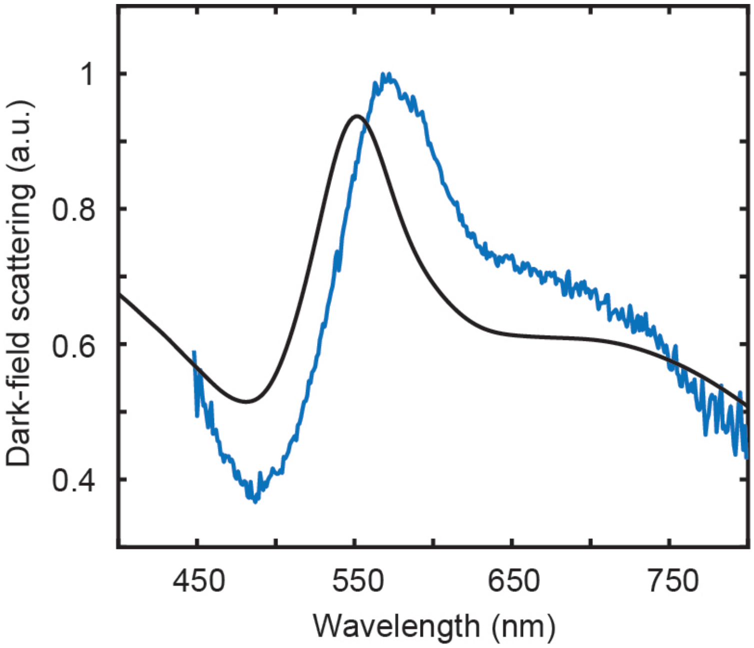

Figure 4.4.9: Dark-field scattering spectra of a bare 200 nm gold NP (without DNA modification). Blue: experimental data; black: FDTD calculation. A bluer dipole mode (∼550 - 580 nm) and a redder quadrupole mode (∼700 nm) are both observed. The discrepancy between experiment and calculation may be attributed to the use of a plane wave to calculate the scattering spectrum. For large particle sizes, retardation effects become significant, and it is necessary to use a conical annular source (as in the experiments) to calculate the dark-field scattering spectrum. [18] Still, the dipole simulations discussed in the main text do accurately represent the experiments regardless of particle size.

two different maps for the two different $z$ slices: the center slice has a wide, ring-shape apparent emission position density (Figure 4.4.10e), for which the radial plot (Figure 4.4.11) shows about 40 nm emission mislocalization, and the upper and lower slices show the highest localization density at the center (Figure 4.4.10f). The results in Figure 4.4.10 demonstrate that 3D imaging can resolve $z$ positions to reveal the true coupling effect. Figure 4.4.10 also demonstrates that a simple analysis of the 2D projection alone, which includes the data from all image slices with different $z$ positions, can lead to erroneous conclusions about the mislocalization if not carefully considered.

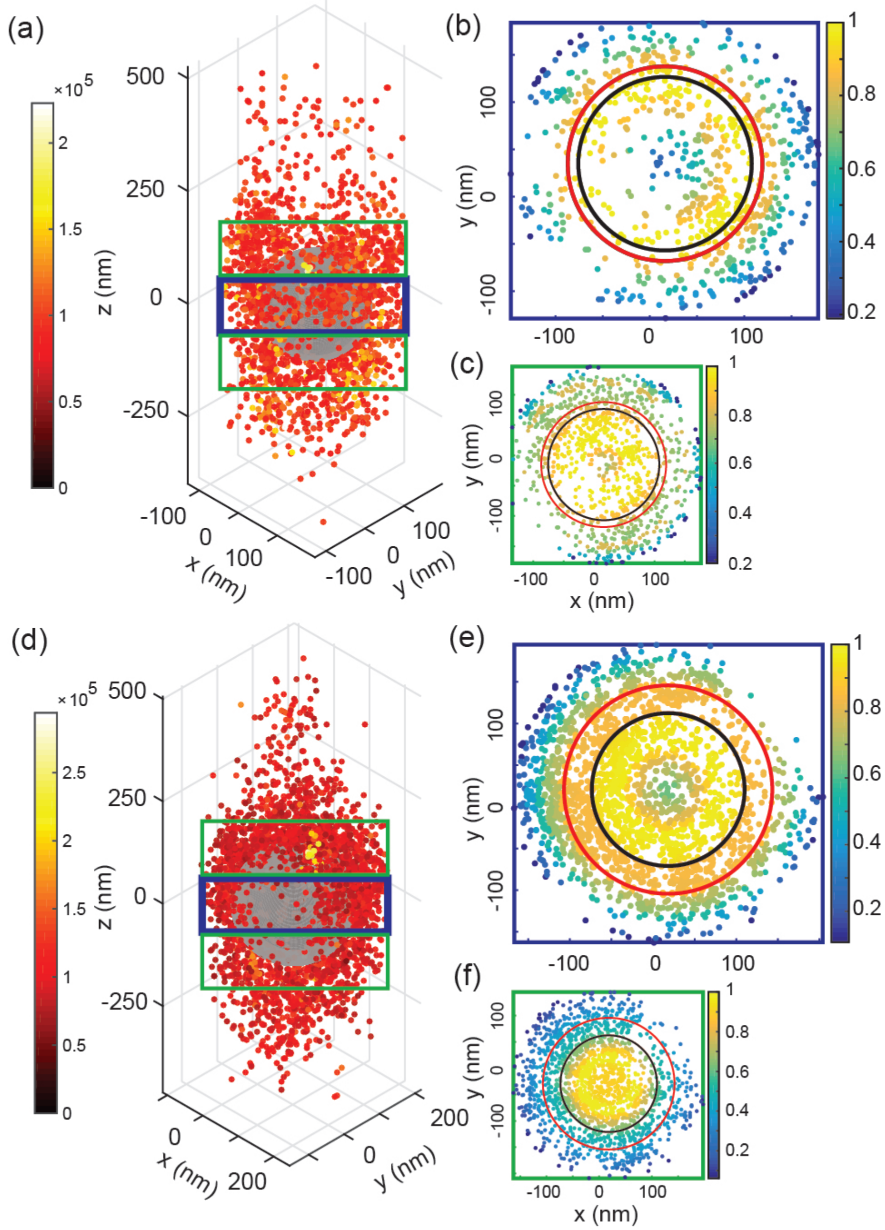
(a)
×10^5
2
1.5
1
0.5
0
500
250
0
-250
z (nm)
-100
0
100
x (nm)
-100
0
100
y (nm)
(b)
100
0
-100
y (nm)
-100
0
100
1
0.8
0.6
0.4
0.2
(c)
100
0
-100
y (nm)
-100
0
100
x (nm)
1
0.8
0.6
0.4
0.2
(d)
×10^5
2.5
2
1.5
1
0.5
0
500
250
0
-250
z (nm)
0
200
x (nm)
0
200
y (nm)
(e)
100
0
-100
y (nm)
-100
0
100
1
0.8
0.6
0.4
0.2
(f)
100
0
-100
y (nm)
-100
0
100
x (nm)
1
0.8
0.6
0.4
0.2

Figure 4.4.10:

Figure 4.4.10: 3D localizations. (a) 3D localizations of dye molecules attached to a 200 nm gold NP via 11 nm DNA linkers. Each dot represents one emission localization, color coded by intensity. (b) $xy$ plane projection of all the localization positions inside the central 150 nm thick slice (blue rectangle in 'a'). Color bar: normalized density of localizations. The density is averaged at each radius according to the circular symmetry of the system. Black circle: gold NP; red circle: actual dye molecule positions. (c) $xy$ plane projection of all localizations inside the two outer slices combined (green rectangles in 'a'). (d-f) Same plots as in 'a-c' but with 32.6 nm DNA spacers. In both cases, the central slice projection maps show wider, ring-shaped localization densities than the top/bottom slices, which is evidence that super-resolution imaging provides 3D spatial information in this structure.

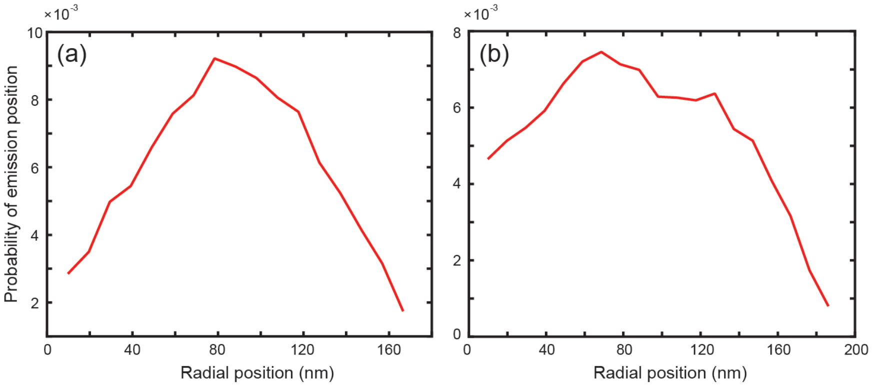

Figure 4.4.11: Radial density curve of center 150 nm slice in Figures 4.4.10a and f, for molecules coupled to a 200 nm gold NP with (a) 11.0 nm spacers and (b) 32.6 nm spacers. These curves correspond to the maps in Figures 4.4.10b and e, respectively.

### 4.4.4 2D imaging of 80 nm NP-coupled dye molecules.

Though 3D imaging enables $z$ filtering of plasmon-coupled dye emission, providing access to the ideal ring-like geometry in Figures 4.4.10b and e, our astigmatism-based 3D imaging approach permitted only axial resolutions of $\Delta z \sim 60$ nm. Thus, though the center slice of 200 nm NPs could be separated from the top and bottom with this approach, the center slice of smaller gold NPs cannot be parsed in this way. However, 80 nm gold NPs (diameter from DLS: 78.6 nm) have bluer resonance peaks that overlap better with the ATTO532 fluorescence spectrum, and avoid the higher-order modes and retardation effects which exist in the

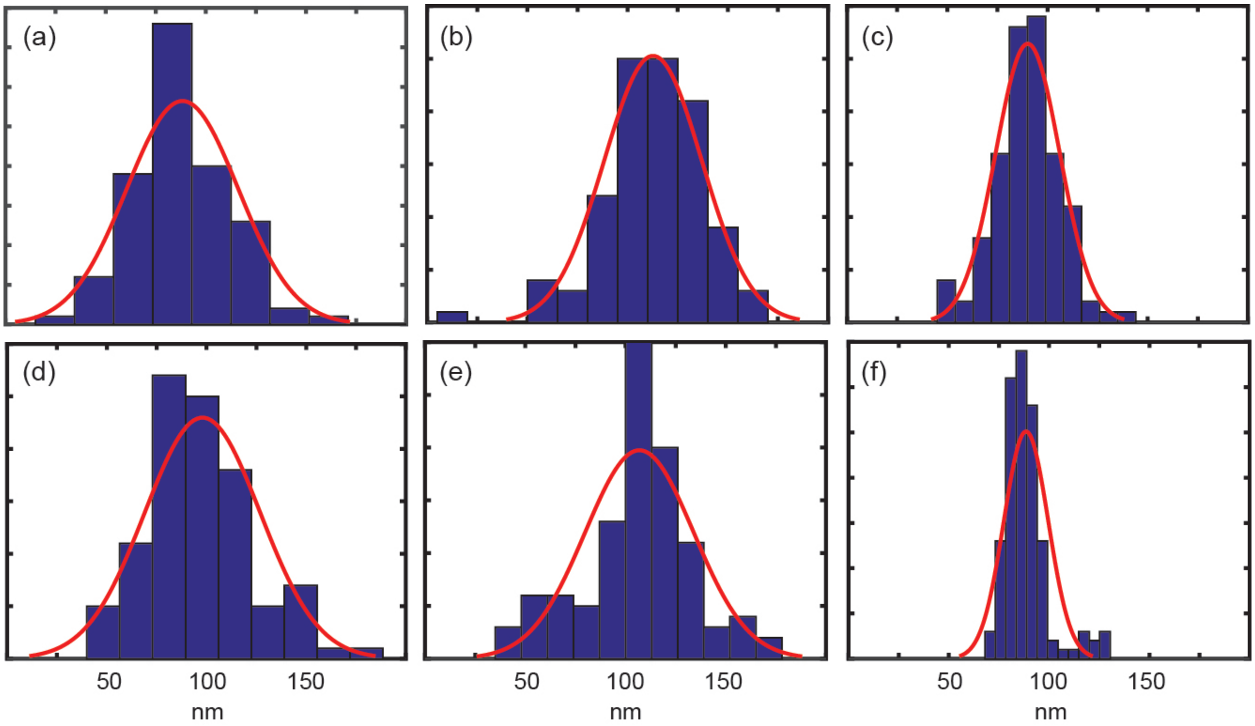

Figure 4.4.12: 2D localization precisions of representative single ATTO532 dye molecules. (a-c) $x$-position precision. (d-f) $y$-position precision. Standard deviations from a to f: 27 nm, 24 nm, 16 nm, 28 nm, 26 nm, and 11 nm, respectively. Average standard deviation on localization precision from multiple molecules is $\sim$22 nm.

larger particles (Figure 4.4.9). Therefore, 80 nm gold NPs provide a better, more interesting structure for plasmonic fluorescence enhancement, and it is important to understand the emission mislocalization for assemblies of ATTO532 dyes and 80 nm gold NPs.

We separated ATTO532 from 80 nm gold NPs with dsDNA spacers of four different lengths: 3.5 nm, 11.0 nm, 22.8 nm and 32.6 nm (Table 4.3). For the 3.5 nm spacer length, we observed very few emission events. Since DLS indicates an 86 nm assembly diameter, this decrease in localization density is consistent with quenching of the dye molecules at very short separation distances. [46, 118] For the three other spacer lengths, the emission from each dye molecule was detected and the apparent emission position was resolved with an $xy$ localization precision of ± 22 nm (Figure 4.4.12) with 2D dSTORM imaging. To quantitatively examine the super-resolved apparent emission patterns from dye molecules conjugated to gold NPs, the apparent localization positions (relative to each NP center position) from all dyes in 77 - 102 single-particle experiments were compiled into one map for each spacer length (Figures 4.4.13a-d; Table 4.4). For example, the apparent position and fluorescence intensity for each emission localization in all assemblies with 11 nm spacers is indicated with a dot in Figure 4.4.13a. Interestingly, in this map most of the best enhanced molecules (yellow color) have apparent emission positions near the center of the assembly; this pattern is consistent with our previous findings for other sample geometries that the best coupled (brightest) molecules are strongly mislocalized and appear to emit from the center of the NP. [46]

| Spacer lengths (nm) | No. of NPs | No. of single molecules | No. of localizations |
|---|---|---|---|
| 11.0 | 102 | 151 | 2691 |
| 22.8 | 94 | 195 | 2650 |
| 32.6 | 77 | 160 | 4748 |

Table 4.4: Statistics of 80 nm gold NP/dye assemblies dSTORM experiments.

Still, imaging this spherical geometry yields a 2D projection of all molecules at all $z$-positions; molecules that appear to radiate from the center of the assembly therefore might be molecules that are actually at the top or bottom of the NP in 3D space and that would show up at the center due to projection even without coupling. To quantify how mislocalized the apparent emission positions are from the actual emitter positions, we instead look at the density distribution in the localization maps. Here, a stronger coupling will shift more apparent emission positions toward the NP center and generate a more concentrated distribution (higher density of apparent emission events) at the center; a weaker coupling would lead to a more diffuse distribution with lower, more spread out density in the center. The normalized

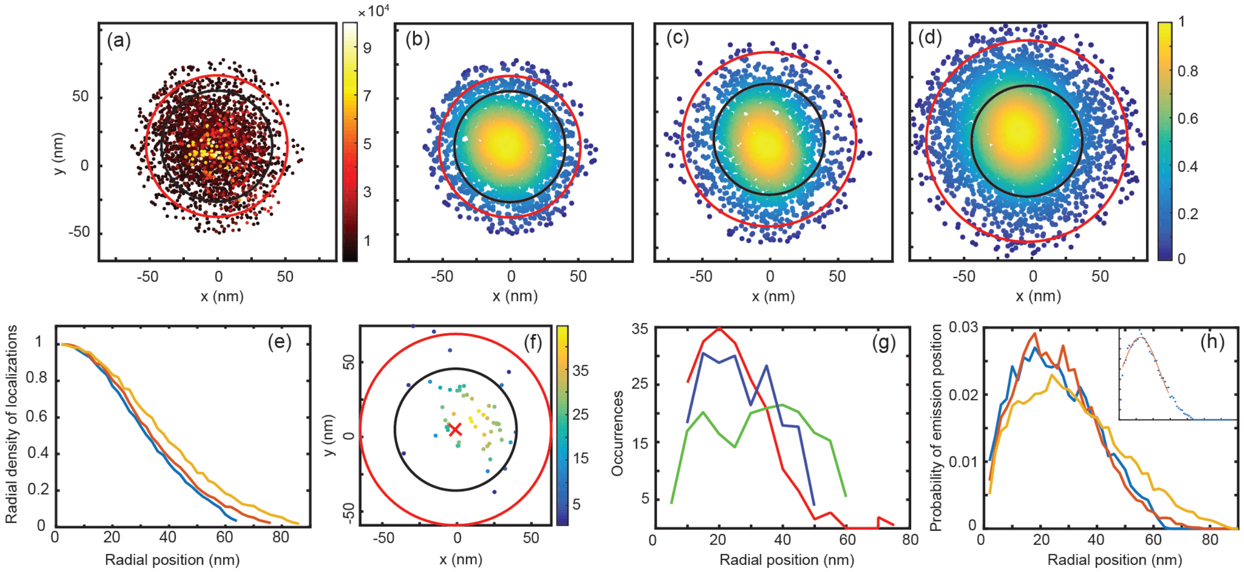

Figure 4.4.13: 2D localization. (a) 2D localizations of dyes 11.0 nm from an 80 nm gold NP, color coded by intensity. Black/red circles: gold NP circumference/actual dye positions. (b-d) Localization maps for 11.0 nm (b), 22.8 nm (c) and 32.6 nm (d) dsDNA spacers, color coded by normalized localization densities. (e) Radial density plots for 11.0 nm (blue), 22.8 nm (red), and 32.6 nm (yellow) spacers calculated directly from the density maps in 'b-d'. (f) Localizations from a single molecule as in Figure 4.4.2e. (g) Localization probability plot for the single molecule in 'f' (red) and two other examples. The probability at each radius is the average of density of all dots at that concentric slice. (h) Single-molecule localization probability curves for 11.0 nm (blue), 22.8 nm (red), and 32.6 nm (yellow) spacers obtained by adding all single molecule radial density curves like in 'g'. Inset: Gaussian fit of the yellow curve.

density maps were calculated for 11.0 nm, 22.8 nm, and 32.6 nm spacers (Figures 4.4.13b, c, d, respectively), and all three lengths give qualitatively obvious concentrations of apparent emissions at the assembly center. The radial plots of the three density maps (Figure 4.4.13e) indicate subtle differences between the profiles for the 11.0 nm spacer (blue line), 22.8 nm spacer (red line), and 32.6 nm spacer (yellow line), but the trend is only qualitative.

We therefore developed a new analysis method based on the single-molecule data to quantify differences in coupling as a function of spacer length. Indeed, the density maps in Figures 4.4.13b-d and the corresponding radial density plots in Figure 4.4.13e, which combine every localization of all dye molecules attached to all NPs, provide an ensemble-averaged view and neglect the single-molecule information that is available in our dSTORM data. Thus, to take advantage of the single-molecule information, we looked at the emission localizations positions from each single molecule individually as described in Figure 4.4.2e. The map of localizations over the course of 100 imaging frames for one example single molecule is shown in Figure 4.4.13f, and the emission localization probability for that one molecule was calculated as a function of radius from the NP center (red line in Figure 4.4.13g). Two additional example curves are also plotted in Figure 4.4.13g. In these single-molecule radial plots, the peak of each curve corresponds to the most likely emission position for that molecule; this is the position that is considered the average emission position in single-molecule imaging. Importantly, the localization probability peak positions here do not coincide with the particle center, rather this position reflects the true mislocalized apparent emission position of the corresponding molecule.

To quantify the mislocalization without averaging that blurs the ensemble analysis in Figures 4.4.13b-e, we added the single-molecule localization probability curves from all molecules instead of merely considering the localization events for all molecules as a whole. These summed curves were normalized to provide a probability distribution (Figure 4.4.13h), and a fit to this curve (Figure 4.4.13h, inset) reveals how the emission peak position varies as a function of spacer length. For the two shorter spacers (blue and red curves), the most probable apparent emission position (curve peak) is at ∼20 nm, whereas for the longest spacer (yellow curve), the peak is shifted to ∼25 nm.

### 4.4.5 Statistical simulations of plasmon-free dSTORM experiments.

The experimental results in Figure 4.4.13h explicitly quantify the influence of spacer length on emission mislocalization. However, because the dyes are distributed on a 3D spherical surface, in-depth analysis is needed to separate the effect of the 2D projection from the true mislocalization. We therefore compared the peak positions of the single-molecule localization probability curves from simulated data for an ideal dSTORM experiment (i.e., in the absence of plasmonic coupling). For example, to match the experimental parameters for the shortest linker assemblies (78.6 nm NP diameter and 11.0 nm dsDNA spacer), we stochastically sampled the $xy$ positions of 2,300 points (number chosen based on usual experimental statistics; Table 4.4) on the surface of a 100.6 nm diameter sphere. The simulated localization positions and densities for this uncoupled system are shown in Figures 4.4.14a and b, respectively. Figure 4.4.14b clearly indicates a ring-shaped maximum density at ∼40 nm radius (yellow region). This radius is shifted in from the actual radius of the sphere (red circle) because of the 2D projection, but is clearly different from the map in Figure 4.4.13b, where the localization density concentrated at the NP center.

The difference in the localization density distribution between the experiments in Figure 4.4.13b and the simulations in Figure 4.4.14b can be attributed to (1) finite localization pre-

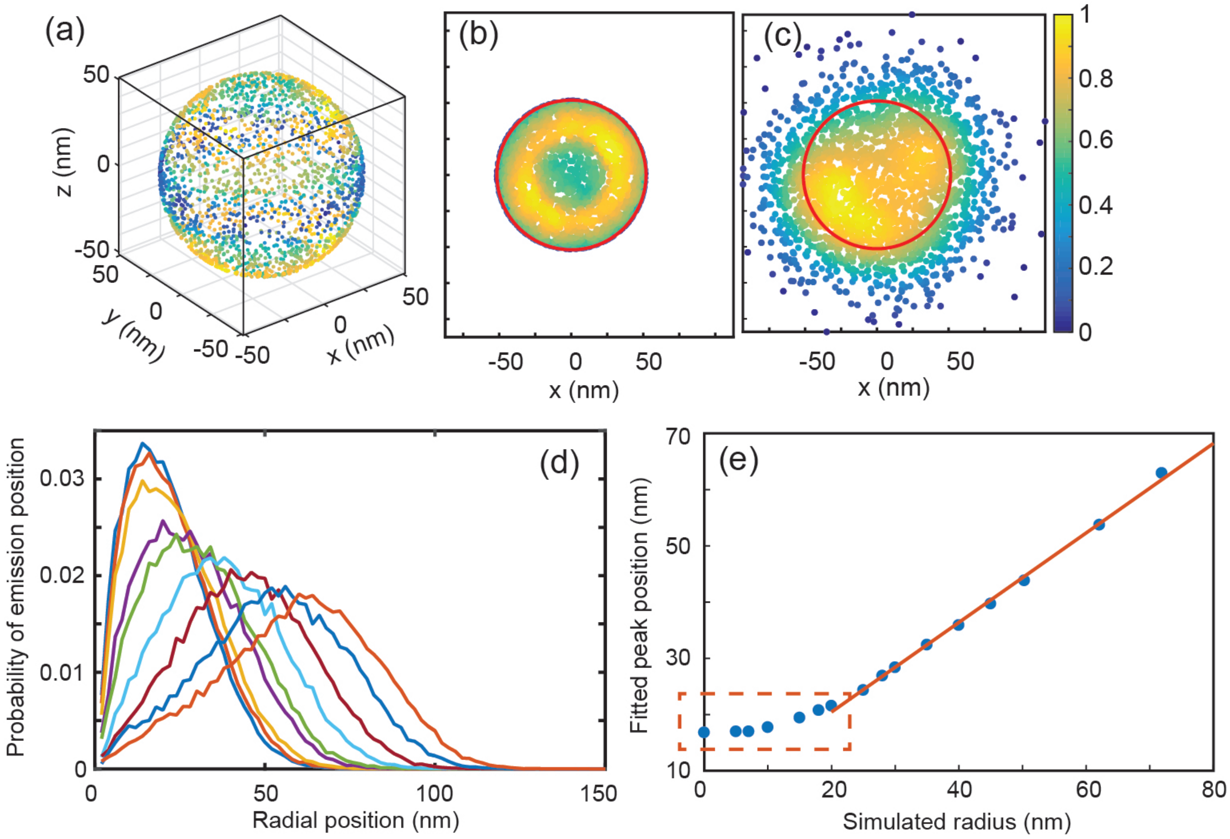

Figure 4.4.14: Statistical simulation of plasmon-free dSTORM experiments. (a) 2,300 randomly sampled dots on a 3D 50.3 nm-radius sphere color coded by normalized dot density in 2D projection. (b) $xy$ plane projection as in 'a' color coded by normalized density. (c) Representative simulated localization position density map from 150 single dye molecules projected on the $xy$ plane incorporating localization precision and dye blinking statistics (Figure 4.4.15). Red circles in 'b' and 'c': sphere circumference. (d) Localization probability curves as in Figure 4.4.13(h). From left to right, sphere radius = 5, 10, 15, 25, 30, 40, 50.3, 62.1, and 71.9 nm. (e) Peak positions of the localization probability curves in 'd' as a function of the actual simulated radii. The relationship is linear for radius > 20 nm ($y = 0.80x + 4.5; R^2 = 0.998$). Below 20 nm (dashed rectangle), the data deviates from the linear trend and it is not possible to interpolate precisely in this region.

cision in the experiments, (2) finite sampling in the experiment, and (3) plasmon coupling. To account for the first two effects, the true imaging conditions are replicated in Figure 4.4.14c by adding noise in the positions according to the experimentally characterized 2D localization precision (± 22 nm; Figure 4.4.12), and by reducing the number of positions simulated from 2,300 to 150 single molecules. Each molecule is localized multiple times according to the experimental blinking statistics (Figure 4.4.15) so that the total localization number is still ∼2,300. Interestingly, the localization density map in Figure 4.4.14c for the uncoupled simulations still shows the greatest localization probability at ∼40 nm (yellow region; circular asymmetry due to limited sampling; compare Figures 4.4.14c to b), and is still very different from the experimental data (Figure 4.4.13b), which shows a concentrated localization distribution at the NP center. The clear difference between the uncoupled case in Figure 4.4.14 and the coupled experimental measurements in Figure 4.4.13 clearly demonstrates that plasmon coupling results in significant mislocalization of fluorescence emission.

These simulated imaging data were translated in Figure 4.4.14d into curves of single-molecule localization probability (calculated as in Figure 4.4.13h). The localization probability varies as a function of actual simulated sphere radius (Figure 4.4.14e and Figure 4.4.16). When the sphere radius is 20 nm or smaller, the position of maximum emission position probability is near the NP center (dashed rectangle in Figure 4.4.14e), which indicates that at this experimental localization precision, different radii less than 20 nm are not distinguishable. On the other hand, with sphere radius $>$ 20 nm, the maximal probability of emission position increases with sphere diameter. Most importantly, the relation is very linear. Thus, we can accurately determine the actual radius even with the presence of a 2D projection and finite localization precision (∼22 nm). With the current experiment conditions, differences in radii down to ±5 nm are readily distinguishable in the straight-line regime. Furthermore,

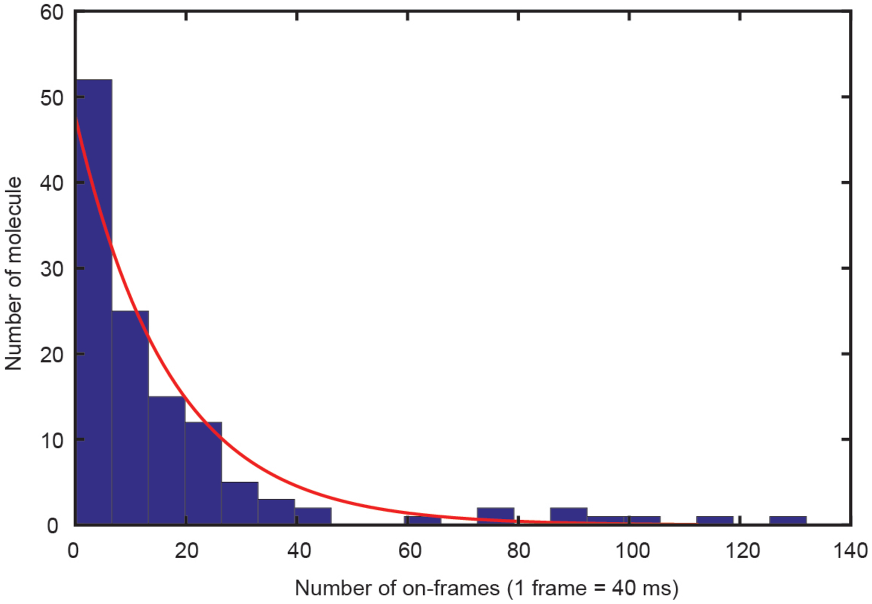

Figure 4.4.15: The fluorescence from each ATTO532 molecule is detected over sequential 40-ms imaging frames before photobleaching. Here, the distribution of the number of on-frames for each single ATTO532 dye molecule coupled to 80 nm gold NP is shown. The distribution is fit to an exponential decay with $t_{1/2} = 17$ frames, which is used in statistical simulations.

for these simulations of uncoupled assemblies, the linear correlation between the fitted peak position and the original sphere radius is robust to simulation parameters: the radial curves in Figure 4.4.14d and the linear correlation in Figure 4.4.14e are unchanged whether high sampling (here: 1,500 simulated molecules) or fewer simulated molecules (150 molecules; Figures 4.4.16 and 4.4.17) are analyzed. Therefore, the single-molecule localization analysis introduced in Figure 4.4.13h is indeed able to reveal information down to 5 nm precision, even when only 2D projection maps are available and the localization precision is as high as 22 nm.

Importantly, this new understanding of the single-molecule localization probability distributions enables the first ever quantitative measurement of the emission mislocalization phenomenon that has been recognized by Biteen et al. and Waks et al. over the last five

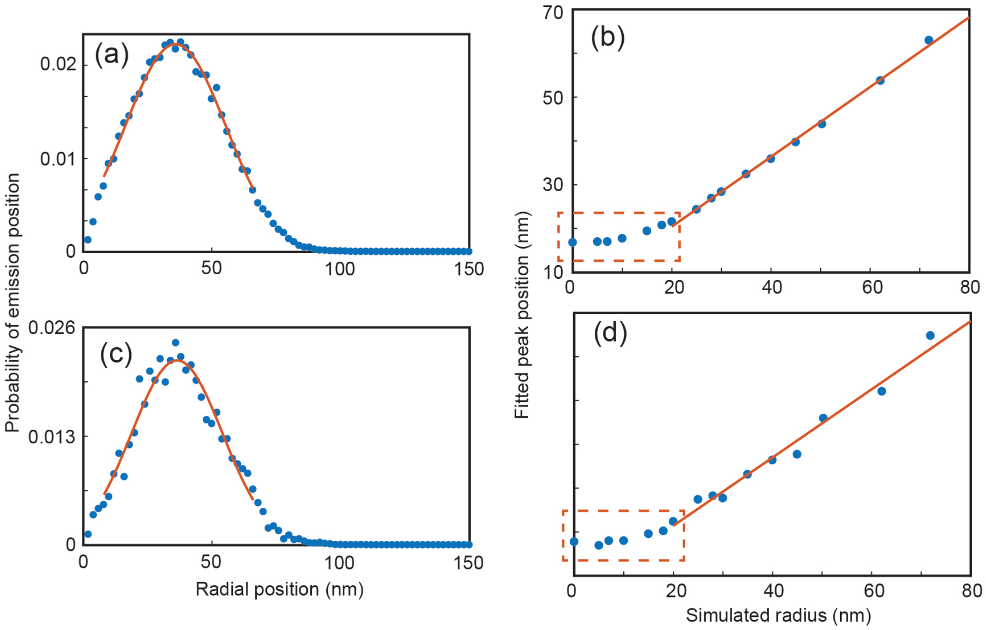

Figure 4.4.16: (a,c) Example fits of the emission localization probability curves to a Gaussian function to find the precise peak positions. (b,d) calibration curve of fitted peak positions versus actual simulated radius. (a,b) 1500 simulated molecules. Calibration curve fitting function: $y = 0.79612x + 4.5367.R^2 = 0.998$. (c,d) 150 simulated molecules. Calibration curve fitting function: $y = 0.77788x + 5.8864, R^2 = 0.979$. Despite the noisier data in (c), which more accurately represents the experiments, the calibration curves are very similar. The regions below 20 nm highlighted in the dashed rectangles in 'b' and 'd' do not follow the linear relation.

years. [46,100] The simulated look-up-table in Figure 4.4.14e provides the context in which to interpret the experimental data (Figure 4.4.13h). For instance, fitting our experimental localization probability curve (Figure 4.4.13h, yellow line; Figure 4.4.18) gives a peak position of 24.9 nm for the 32.6 nm spacer (dye-NP assembly radius of 71.9 nm), which corresponds based on the look-up table in Figure 4.4.14e to 25.6 nm in 3D. Thus the plasmonic NP/dye interaction accounts for a mislocalization of 71.9 nm − 25.6 nm = 46.3 nm! The shorter spacers (11 nm and 22.8 nm), show localization probability maxima at 20.9 nm and 21.9 nm, respectively (Figure 4.4.18). These apparent emission positions are very close to the NP

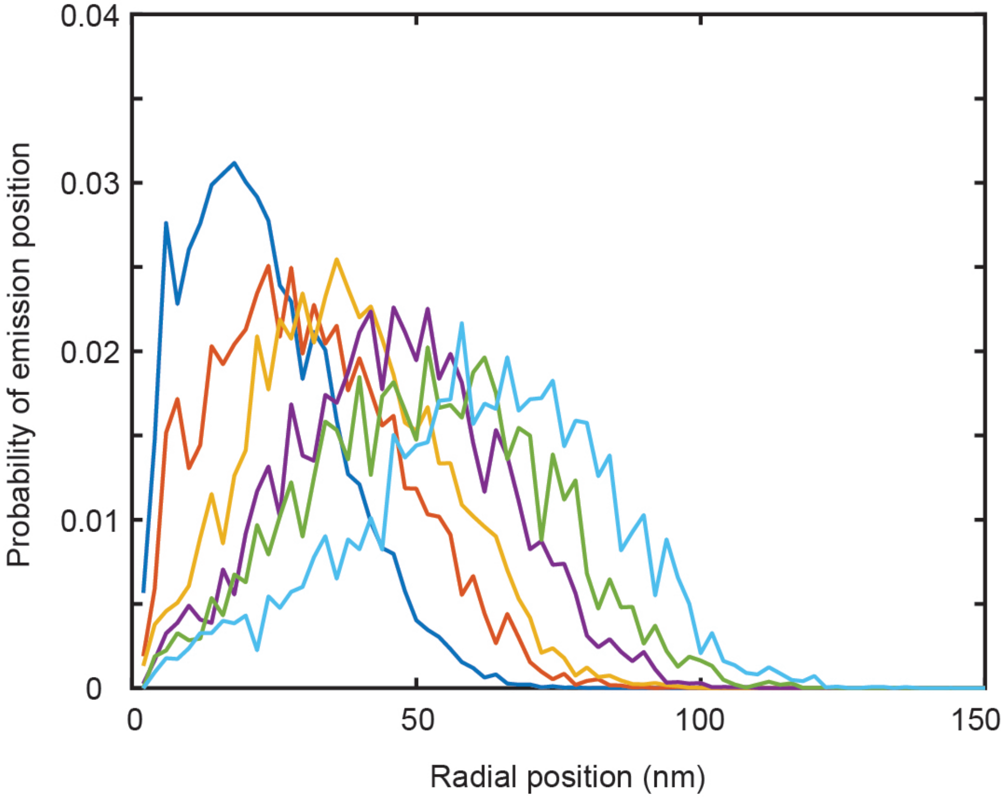

Figure 4.4.17: Emission localization probability curves for 150 simulated molecules. Simulated radius from left to right, dark blue: 10 nm, orange: 30 nm, yellow: 40 nm, purple: 50.3 nm, green: 62.1 nm and light blue: 71.9 nm.

center and indicate mislocalizations of 29.7 nm and 40.3 nm. However, because these fitted peak positions are at the non-linear region in Figure 4.4.14e, these mislocalizations are lower bounds, and the apparent emission position may indeed deviate from the actual emitter position by up to 50.3 nm and 62.1 nm. The mislocalization of dye molecules near a plasmonic NP is therefore real, and we have shown here that the magnitude of mislocalization can be quantified with far-field single-molecule, super-resolution imaging.

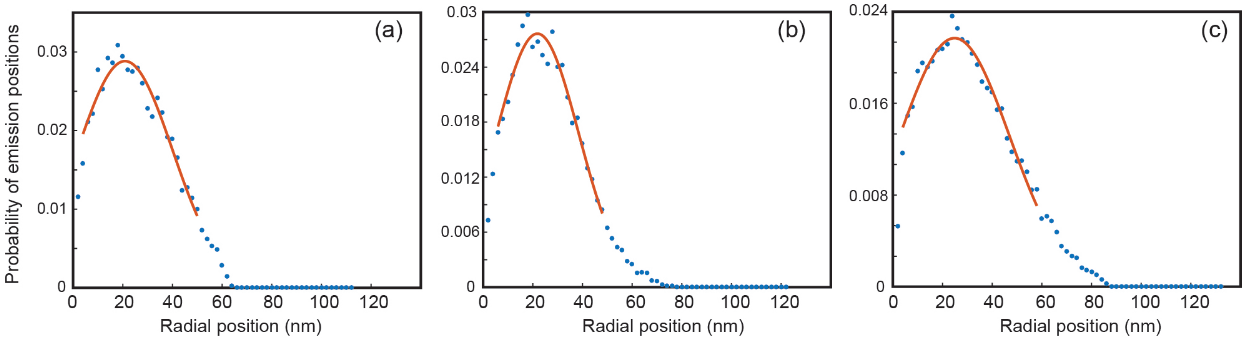

Figure 4.4.18: Fits of the experimental data to Gaussian function to find the precise peak positions for three different spacer lengths. (a) 11.0 nm spacer: peak position = 20.9 nm; (b) 22.8 nm spacer: peak position = 21.9 nm; (c) 32.6 nm: peak position = 24.9 nm.

### 4.4.6 Electromagnetic calculations.

To develop a theoretical framework within which to understand the physics underlying this mislocalization effect, we conducted full-field FDTD electromagnetic calculations of radiating dipoles near a gold NP. For each spacer length (11.0, 22.8, and 32.6 nm), the far-field emission profile for each of a series of dipoles (Figure 4.4.19a) was calculated and fit to a 2D Gaussian to determine the super-resolved apparent emission positions according to our experimental protocol for single-molecule imaging. Calculated localization density maps (Figures 4.4.19b-f) were obtained by introducing the experimental localization precisions and dye blinking statistics. We calculated maps for the 150-nm thick center slices of the 200 nm NP assemblies. These maps show broad, ring-shaped localization distributions which match the experimental data for 150-nm center slices (compare Figures 4.4.10b and e to Figures 4.4.19b and c). For the 32.6 nm spacer in Figure 4.4.19c, the apparent emission maximum is at 110 nm, showing the expected coupling effect (emission mislocalization toward the NP center, Figure 4.4.20). Surprisingly, because the emission pattern of a single molecule is distorted by the nearby nano-antenna, under certain conditions, the emission actually seems to be pushed away from

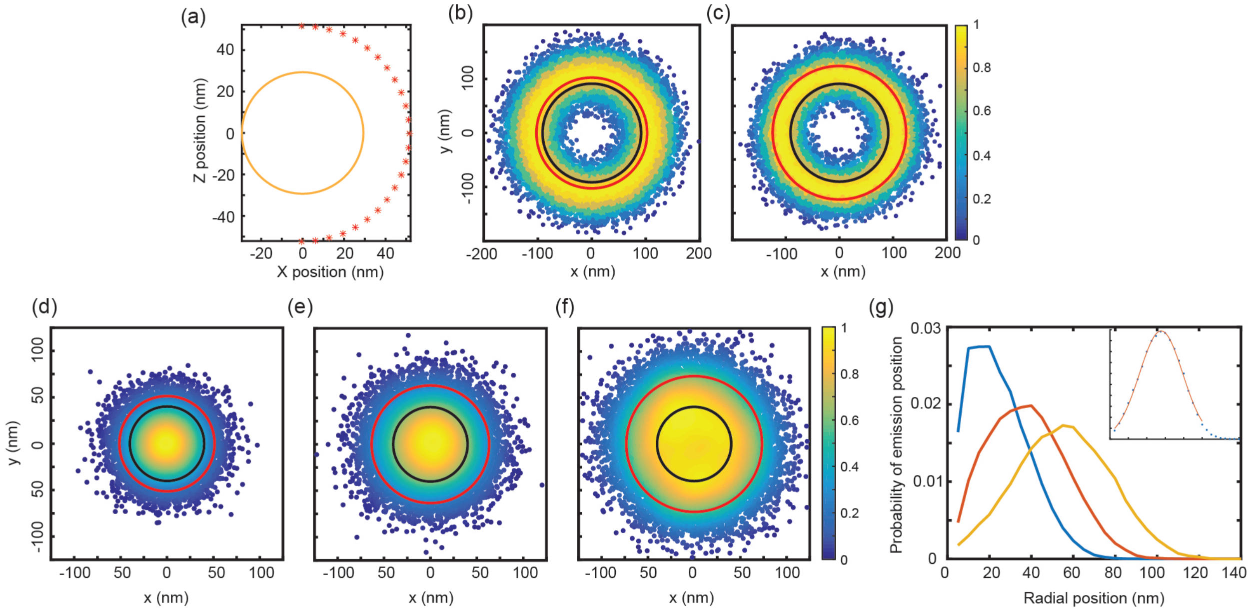

Figure 4.4.19: FDTD calculations. (a) Calculation geometry. Red stars: simulated dipole positions. All possible actual molecule positions were accounted for by spherical symmetry. (b,c) Localization densities for dipoles coupled to a 200 nm gold NP with (b) 11.0 nm and (c) 32.6 nm spacers. Density values are averaged over each concentric circle to recover the symmetry. These plots are the $xy$ projections of a 150-nm slice in the center of the assembly. (d-f) $xy$ projections of single-molecule apparent emission localizations from dipoles coupled to an 80 nm gold NP with (d) 11.0 nm, (e) 22.8 nm, (f) 32.6 nm dsDNA spacers, color coded by densities. In 'b - f', experimental localization precision and dye blinking statistics are incorporated. (g) Single-molecule localization probability curves for simulations in 'd - f' (blue: 11.0 nm; red: 22.8 nm; yellow: 32.6 nm), calculated as in Figure 4.4.13h by summing the radial density curve from each molecule. Inset: Gaussian fit of yellow curve.

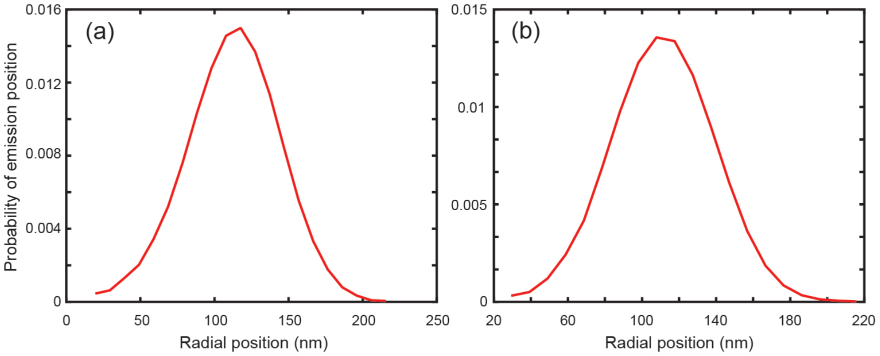

Figure 4.4.20: Radial density curve of center 150-nm slice for molecules coupled to 200 nm gold NP from FDTD calculation data, with (a) 11.0 nm spacer and (b) 32.6 nm spacer. Compared to Figure S8, these FDTD calculations predict a weaker coupling effect (peaks are at a larger radial position).

the NP. For example, for the 11.0 nm spacer in Figure 4.4.19b, the apparent emission center position is at 120 nm, a greater distance than the actual dye position diameter of 100.5 nm (Figure 4.4.20). This subtle difference was also observed in the experimental data: the shorter spacer (Figure 4.4.10b) produced slightly less mislocalization than the longer spacer (Figure 4.4.10c).

For the 80 nm NP assemblies, we calculated the apparent dye emission positions for three spacer lengths corresponding to the experiments in Figure 4.4.13 (Figures 4.4.19d-f). In general, the calculations reproduce the experiments: the majority of the molecule apparent emissions appear at the center, creating very high localization densities consistent with strong mislocalization. This effect depends on the spacer length. Notably, for the shortest spacer (Figure 4.4.19d; 11.0 nm), the calculated map looks very similar to the experimental data (Figure 4.4.13b); however, for the medium spacer (Figure 4.4.19e; 22.8 nm), the calculated map shows a more diffuse density distribution, indicating a weaker predicted coupling compared to experiments (Figure 4.4.13c); and finally, a significant discrepancy was noted for the longest spacer (Figure 4.4.19f; 32.6 nm). In this last case, the calculations predict a broad, ring-like distribution of emission events, while the experiments still show very strong coupling and mislocalization (Figure 4.4.13d). Comparing the calculated localization probability curves in Figure 4.4.19g to the experimental curves in Figure 4.4.13h clearly demonstrates this discrepancy: the calculated distance-dependent mislocalization distances are 32.7, 22.7, and 7.9 nm for 11.0 nm, 22.8 nm and 32.6 nm spacers, respectively; these mislocalizations are consistently smaller than experimental values. Because the mislocalization distance depends strongly on the dipole orientation, especially for the longer spacers (Figure 4.4.21), this disagreement may be explained by the dipole orientation of molecules, which was not readily measurable in real experiments. Furthermore, for a given dipole orientation, the mislocalization distance also depends strongly on the axial ($z$) position (and thus the lateral displacement from the imaging axis) of the molecule (Figure 4.4.21).

## 4.5 Conclusions.

The ability of single-molecule super-resolution imaging to beat the diffraction limit of light depends on the number of photons detected from each probe molecule. [25] Diverse efforts have addressed the challenge of improving label brightness and coupling to plasmonic metal NPs to improve the optical properties of common labeling probes has great potential to broadly improve super-resolution imaging. However, even though the plasmon resonance tremendously increases the fluorescence decay rate to produce a much brighter probe, the high local density of optical states drastically changes the emission pattern of the coupled fluorescent molecule. As a result, the super-resolved emission is mislocalized by the nearby nano-antenna and thus no longer reflects the actual emitter position. Here, we have measured the apparent emission positions of dyes coupled to a spherical plasmonic NP molecule by

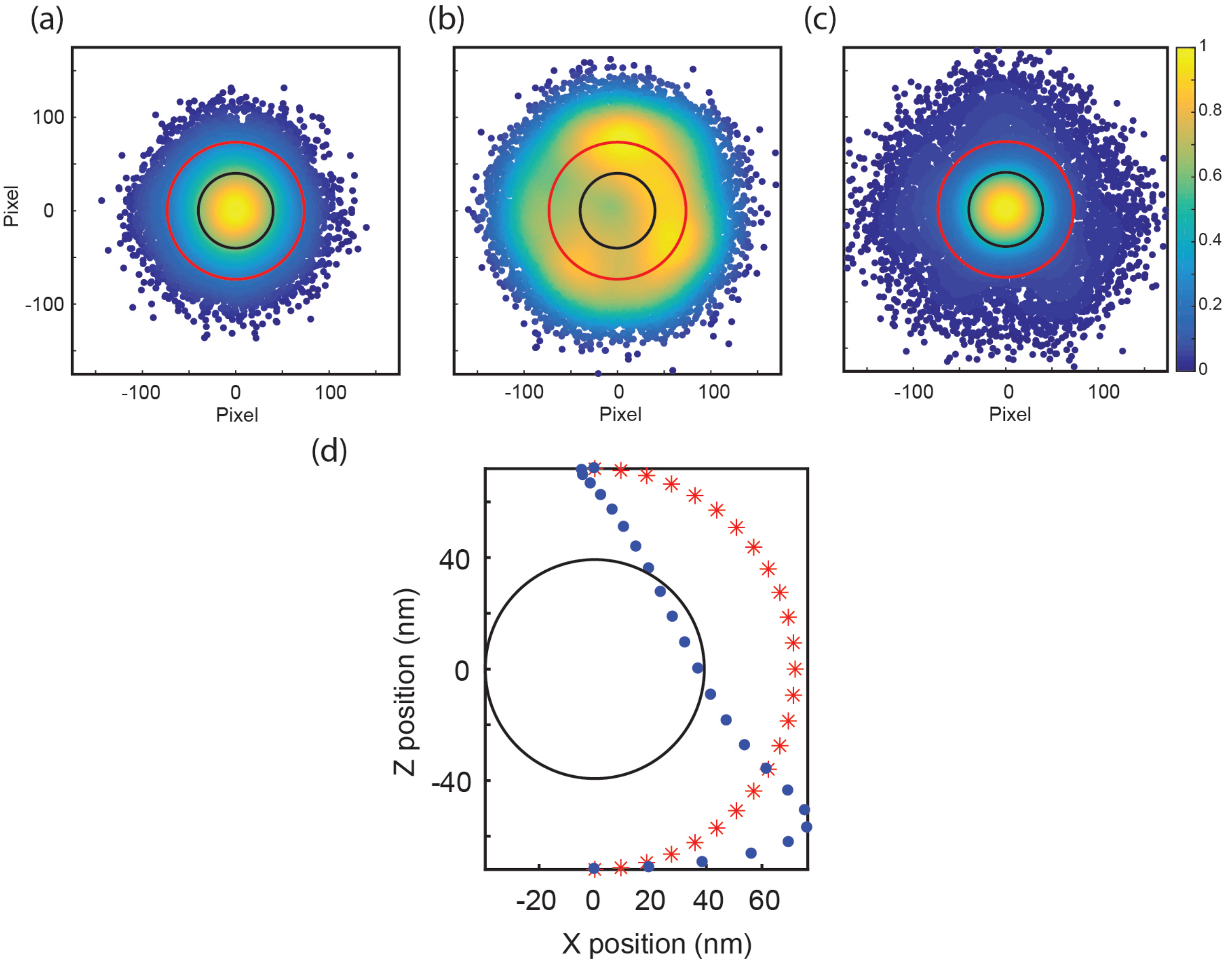

Figure 4.4.21: FDTD calculations of apparent emission maps for ATTO532 dye with (a) $x$-dipole orientation, (b) $y$-dipole orientation, and (c) $z$-dipole orientation in an 80 nm gold NP/32.6 nm dsDNA/ATTO532 assembly. (d) Mislocalizations at different $z$-positions for $x$-dipole orientation (red stars: actual dipole positions, blue dots: predicted apparent emission position).

molecule. By fine tuning the separation distance with nanometer precision, we understood the distance-dependence of this mislocalization effect, and for the first time, we demonstrate the ability to quantitatively deconvolve mislocalization effects for plasmon-coupled dyes and therefore harness the power of plasmon-enhanced super-resolution imaging without bias.

# CHAPTER V

# Conclusions and future directions

## 5.1 Conclusions

Single-molecule super-resolution fluorescence microscopy is playing a more and more important role in studying sub-diffraction (smaller than a few hundreds of nanometers) structures, dynamics and reactions. It possesses high sensitivity, maintains the native investigated environment (does not require high vacuum or low temperature) and exerts minimal perturbations to the target, which is especially important for studying living systems. Further enhancing the power and scope of this valuable technique by providing better resolution using plasmonic nano-antenna is therefore very meaningful work. Yet many challenges and underlying mechanistic questions need to be solved for better understanding this phenomenon.

The present Thesis focused on one central question: what is the interaction between a single nano-antenna and various kinds of single fluorescent molecules? And how does it change as a function of separation distance? Chapters II and III study the distance-dependence plasmon-enhanced fluorescence for both dye molecules and fluorescent proteins. Chapter II uses the PAINT single-molecule technique—which takes advantage of adsorption/ desorption molecule motion in solution—to investigate the single molecule fluorescence located near a single gold nanorod separated by a nanometer-thick spacer layer. We found that this spacer layer is essential for achieving the optimal fluorescence enhancement and 10 nm proved to be the best thickness for this particular geometry. Plasmon-enhancement was shown to be universal for fluorescent proteins as well as dye molecules; interestingly, fluorescent proteins, which were originally fluorophores with poor brightness, actually gained higher enhancement due to the increased electromagnetic field. This work provided the evidence that both dye molecules and fluorescent protein molecules were indeed enhanced by coupling to a plasmonic nano-antenna with a 10-nm spacer layer. This thickness value was important as it was close to the thickness of cellular membrane, therefore membrane proteins labeled with a fluorescent probe could be conveniently enhanced coupled to a plasmonic substrate.

Chapter III aims to understand the distance-dependent fluorescence enhancement in a context of more precise distance control, as accurate separation distances are unknown in the PAINT experiments in Chapter II. To accomplish this, red and green photoactivatable fluorescent proteins are fused with a streptavidin protein through cloning; then they are chemically linked to a silica-shell-coated gold nanosphere and the distance can be tuned by changing the shell thickness. This assembly ensures a relatively homogeneous separation distance between each fluorescent molecule and the nano-antenna. We observe a 2-fold enhancement for red photoactivatable fluorescent proteins with a 20-nm spacer. Compared with the results in Chapter II, we can clearly see that the previously obtained 10-nm best thickness is indeed obscured by the distance heterogeneity in PAINT experiments and enhancement can still be observed with even thicker spacer.

Importantly, besides enhancement, the coupling between nano-antenna and fluorescent molecules also leads to an emission mislocalization effect, which has been attracting more and more research interest. Due to the dramatically increased local density of states near an excited plasmonic nano-antenna, the super-resolved emission position of a coupled molecule is significantly changed and cannot truthfully represent the actual emitter position. This effect poses problems when researchers rely on fluorescent molecule positions to map hotspot locations or tracking proteins on a plasmonic substrate. Toward the goal of understanding this mislocalization effect, Chapter IV investigates a gold NP/dye system using both 2D and 3D super-resolution imaging techniques. We find that this emission distortion is up to 40 nm when molecules are located within 32 nm from the nano-antenna. Most importantly, through developing a new single-molecule data analysis method, we show that accurate, quantified distance-dependent mislocalization data can be obtained, which provides great potential for recovering the real emitter position in the coupled system.

## 5.2 Future directions

With the knowledge of the distance-dependent single-molecule plasmon enhancement gained in this Thesis, the next step would be to apply this enhancement in real biological super-resolution imaging. The best targets which are most significantly enhanced are those located in the plasmonic near field ($\sim$ 20 - 50 nm from the nano-antenna). Membrane proteins possess important biological functions and the cell membrane or any additional spacer layers will locate them at the ideal distance for optimal enhancement therefore they are excellent candidates for this purpose. One key question for this application is to design a plasmonic substrate that has the appropriate plasmon resonance for coupling to the fluorophores as well as high nano-antenna density to cover the entire cell region. Nanosphere lithography—where noble metal nano-antennas are formed in the interstices of tightly assembled micron-sized beads—and E-beam lithography—where customized shapes and arrays are directed written through electron beam—can be used to design the desired nano-antenna array and these structures held great promise for plasmon-enhanced imaging. It is important that those designed nano-antenna arrays still have the resonance overlapping well with the investigated fluorophores; furthermore, dense hotspots that are available to interact with the targets on top are most desirable. For instance, bowtie structures [165] can achieve thousands-fold enhancement, yet this high enhancement is only available at the very small nano-gap region. Better array design that can realized higher density of hotspots and expand the area for enhancement would be a challenge. On the other hand, the mislocalization effect is also expected to exist in these array substrates, and it will be interesting to see what the emission localization pattern is like for those coupling plasmonic arrays. By tuning the fluorophore color, nano-antenna resonance and excitation wavelength, different coupling behaviors between molecules and the arrays are expected to be observed.

The interactions between nano-antenna and fluorescent molecules have been investigated in this Thesis in terms of intensity enhancement and super-resolved emission positions. There are many other important aspects to reveal the entire picture of this coupling effect. Anisotropic nano-antennas have LSPRs with well-defined polarizations. For instance, nanorods have both longitudinal and transverse plasmon modes. These modes will couple differently with fluorescent molecules with different emission wavelengths, dipole orientations and locations relative to the nano-antenna. Firstly, it will be interesting to see how the coupling influences the emission polarizations of a nearby molecule due to the plasmon modes. Secondly, it is desirable to find an approach for controlling the dipole orientations of single molecules coupled to a nano-antenna. From the work in Chapter IV, we can see that the dipole orientations of single molecules significantly affect the coupling effect; therefore, if we can separate different dipole orientations, averaged results can be resolved. Guest-host chemistry may contribute to this problem by fixing the orientation of a single fluorophore in the vacancy of a larger molecule. For example, methylene blue single molecules were found to stand vertically when incorporated in the hollow hydrophobic internal region of cucurbit[7]uril. [166] Thirdly, plasmon-enhancement includes excitation enhancement and emission enhancement and the work in this Thesis cannot distinguish the two. By using fluorophores with a large Stoke's shift, such as quantum dots, we can selectively excite at the excitation wavelength or emission wavelength to explore the difference. Furthermore, fluorescence lifetime studies can help to understand how the plasmon coupling influences decay rates of the molecules, shining light on the underlining mechanism.

On the other hand, we can also expand the scope of molecules that interact with plasmonic nano-antennas. For examples, nano-diamonds are carbon nanocrystals that fluoresce due to the nitrogen vacancies. They are bright, non-bleaching and very biocompatible, therefore a potential new category of imaging probe. Gold/silver nanoclusters are very small, fluorescent nanocrystals containing only tens of atoms. They have large Stoke's shift, relative high stability (bleach slower than dye molecules), longer lifetime and high two-photon absorption efficiency. Currently their quantum yield is quite low ($< 5\%$) [167] therefore it is very interesting to see how those nanoclusters can interact with plasmonic nanoparticles and possibly enhancement can be observed.

In summary, interactions between single plasmonic nano-antenna and single molecules are investigated in depth in this Thesis using super-resolution imaging techniques. Deeper understandings of plasmon-coupled fluorescence are gained and it shows great potential for enhanced fluorescence imaging applications. Furthermore, super-resolution in general is great tool for studying many other sub-diffraction optical properties and chemical reactions.

# APPENDICES

# APPENDIX A
# Code for Chapter 3
# cutactivation, pickfits

*cutactivation*: a MATLAB function that cuts the activation frames from the entire recorded movie. The activation frames appear periodically in the movie.

*pickfits*: a MATLAB function that picks the fits within certain frames from the activation frames (in time domain) from all good fits.

```
function cutactivation(file)
% Take out activation frames and output a new .tif file from .mat
 file, where .mat file is 3-dimensional data
% of the original .tif or .nd2 movies.
% INPUT
% file: the .mat data file for the original movie (.nd2 or .tif). This
 file is a
% 3-dimensional matrix containing all the movie data.
% OUTPUT
% A .tif movie without activation frames will be saved. A .mat file
 containing:
% 1)the original frame number of the resulted .tif without activation
 frames
% (e.g. the 100th frame in this new .tif may be the 120nd in the
 original movie,
% so '120' will be saved in an array in the '100th' place). 2) All the
% activation frames (the cut off frames) in an array
fr_rate = 40; % frame rate, ms
act_dur = 600; % how long the activation lasts, ms
interval = 4; % the interval between adjacent activations, s
act_frms = act_dur/(fr_rate);
interval_frms = interval*1000/fr_rate + 4;
% Don't know why there is a 4 frame discrepency.
opt = 1; % Different options for identify activation frames

load(file);
if ~exist('outputmat','var')
    fprintf('Variable name is wrong!\n');
    return
end

[fd,name,ext] = fileparts(file);
num_fr = size(outputmat,3);
width = size(outputmat,1);
height = size(outputmat,2);
[t,~] = plot_Z_profile_mat(file,2,'ifwhole',1);
newmat = zeros(width,height,num_fr);
switch opt
    case 1
        % In this case, 406nm laser (dim frames) is on for a few
 frames, then
        % 561nm laser is open after another few frames delay (even
 dimmer frames
        % when both the lasers are closed). The last frame of the
 darker frames
        % (before 561nm laser is open) will be a peak in the firt
 different
        % function (Y = diff(X)).
        Y = diff(t);
        thrsh = 1000;
        % thrsh is the difference between the dark frame (both lasers
 are off)
```

```
        % and the normal fluorescence background (peak height in Y).
        [~,loc] = findpeaks(Y,'MinPeakHeight', thrsh);
        loc = loc(loc > 800);
        % exclude the peak corresponding for the opening of shutter
(leave at
        % lease 1200 frames, i.e. 48 seconds for bleaching before
begin
        % activations)

        % Sometimes high fluorescence signal also gives "fake"
differential
        % peaks. Take those out.
        med = median(t);
        st = std(t);
        for kkk = 1:size(loc,1)
            if t(loc(kkk)) > (med-0.5*st);
                loc(kkk) = 0;
            end
        end
        loc(~loc) = [];
        % double check
        Z = diff(loc);
        Z_uniq = unique(Z);
        if numel(Z_uniq) ~= 1
            warning('Activation picking may be wrong.');
            Z_uniq
        end
        cycle = size(loc,1);

        cutoffarray = zeros(num_fr, 1);
        newmoviearray = [1:1:num_fr]';
        newmat = outputmat;
        act_lastfrm = zeros(num_fr, 1);
        kk = 1;
        tt = 1;
        first = loc(1);
        for jj = 1:cycle
            curractfr = first + (jj-1)*interval_frms;
            if curractfr < num_fr
                act_lastfrm(tt) = curractfr;
                for ii = 1: act_frms
                    cutoffarray(kk) = curractfr;
                    curractfr = curractfr-1;
                    kk = kk + 1;
                end
                tt = tt + 1;
            end
        end
        cutoffarray(~cutoffarray) = [];
        act_lastfrm(~act_lastfrm) = [];

        newmat(:,:,cutoffarray) = [];
        newmoviearray(cutoffarray) = [];
```

```
    case 2
        % In this case, mostly similar to case 1, but the difference
 is that the
        % 406nm on/561nm off frames are not actually dimmer, they are
 much
        % brighter than the background fluorescence, which generates
 peaks in
        % the original time trace.
        Y = diff(t);
        thrsh = 1000;
        % thrsh is the difference between 406nm laser and the
 background
        % fluorescence.
        [~,loc] = findpeaks(Y,'MinPeakHeight',thrsh);
        % Sometimes high fluorescence signal also gives "fake"
 differential
        % peaks. Take those out.
        med = median(t);
        st = std(t);
        for kkk = 1:size(loc,1)
            if t(loc(kkk)+1) > med
                loc(kkk) = [];
            end
        end
        cycle = size(loc,1);
        cutoffarray = zeros(num_fr, 1);
        newmoviearray = [1:1:num_fr]';
        newmat = outputmat;
        act_lastfrm = zeros(num_fr, 1);
        kk = 1;
        tt = 1;
        for jj = 1:cycle
            curractfr = loc(jj) + 1;
            if curractfr < num_fr
                for ii = 1: act_frms
                    cutoffarray(kk) = curractfr;
                    curractfr = curractfr+1;
                    kk = kk + 1;
                end
                act_lastfrm(tt) = curractfr - 1;
                tt = tt + 1;
            end
        end

        cutoffarray(~cutoffarray) = [];
        act_lastfrm(~act_lastfrm) = [];

        newmat(:,:,cutoffarray) = [];
        newmoviearray(cutoffarray) = [];
end
F = diff(act_lastfrm);
if numel(unique(F)) ~= 1
    warning('Activation picking may be wrong.');
    uniq(F)
```

```
end

newmat = uint16(newmat);
% Save .tif movie without activation frames
outputfile = [fd filesep name '_noactivation.tif'];
options.overwrite=true;
saveastiff(newmat,outputfile,options);

cutdatafile = [fd filesep name '_activation_frms_info.mat'];
save(cutdatafile, 'cutoffarray','newmoviearray','act_lastfrm');
% 'cutoffaray' is the original frames numbers array that are cut;
% 'newmoviearray' is the original frames numbers array that are kept;
% 'act_lastfrm' is the original frames numbers that correspond to the
 last frame
% of each activation period (the fluorescence signal should be right
 after or
% shortly after this frame). This is useful for identification of real
 data,
% which should appear right after or shortly after this frame.

end
```

*Published with MATLAB® R2016b*

```
function pickfits(fitsfile,act_infofile,varargin)
% This function picks out the fluorescence signal from all the good
 fits
%based on the frames they appear: real signal should be N frames after
 the
% activation frames INPUT fitsfile: the _AccBGSUB_fits.mat file
 generated from
% SMALLLABS algorithm. Note: the analysis is run on _noactivation.tif
 movie so
% the frame number is not the same as the original movie, where the
 activations
% are not taken out. Important variables: fits - contains all the
 gussess
% information and goodfits Boolean; trk_filt - tracks Boolean, tracks
 are
% molecules that last 3 or more than three frames

% act_infofile: the .mat file generated from cutactivation.m.
 Important
% variables: act_lastfrm - the last frame of activation. Signal N
 frames after
% these are considered real. Note: the frames numbers here are the
 numbers from
% the original movie. newmoviearray - what are the original frame
 numbers for
% each frame in the new movie (without activation frames).

% OUTPUT Create a .mat file that meet the picking requirement. The
 data is in
% the same format as _AccBGSUB_fits.mat. File name:
 '_AccBGSUB_fits_picked.mat'.

N = 20;
% How many frames after the activations are considered real data.

params.tracked = 0;
track_Boolean = params.tracked;
% Default: do not use tracked data.

[folder,name,~] = fileparts(fitsfile);
[~,name2,~] = fileparts(act_infofile);
if
 ~strcmp(strrep(name,'_noactivation_AccBGSUB_fits',''),strrep(name2,...
        'activation_frms_info',''))
    warning('Fits file and act_info file do not match!');
    return
end

if nargin > 2
    Fnames = fieldnames(params);
    for iii=1:2:nargin-2
        whichField = strcmp(Fnames,varargin{iii});
```

```
        if all(~whichField)
            warning('Check spelling. Parameter change may have not
 occurred.');
        end

        eval(['params.' Fnames{whichField} ' = varargin{iii+1};'])
    end
end

load(fitsfile);
load(act_infofile);

% check if N is longer than the interval of activation. If yes, ask
 user to
% change N and terminate program
act_interval = act_lastfrm(2) - act_lastfrm(1);
if N >= (act_interval - 1)
    disp('N is larger than the activation interval. Decrease N.');
    return
end

pickedarray_org = zeros(size(newmoviearray,1),1);
% Picked frame numbers in original movie
jj = 1;
for ii = 1:size(act_lastfrm,1)
    for kk = 1: N
        pickedarray_org(jj) = act_lastfrm(ii) + kk;
        jj = jj + 1;
    end
end
pickedarray_org(~pickedarray_org) = [];

% Find their new frame numbers in the new movie
pickedarray_new = zeros(size(pickedarray_org,1),1);
for tt = 1:size(pickedarray_org,1)
    try
        curr = find(newmoviearray == pickedarray_org(tt));
        if curr
            pickedarray_new(tt) = curr;
        else
            fprintf('Reaching the last activation cycle and no
 corresponding frames.\nExit loop and continue.\n');
            break
        end
    catch
        fprintf('tt = %g is not successful.\n',tt);
    end
end
pickedarray_new(~pickedarray_new) = [];
% Take out the good fits in the picked frames. You can choose use
 tracked data
% (first and last frames taken out) or not.

goodfits = fits(find(fits(:,9) == 1),:);
```

```
if params.tracked == 1
    goodfits = fits(find(trk_filt),:);
end
pickedgoodfits = zeros(1,9);
for jjj = 1:size(pickedarray_new,1)
    currfrm = goodfits(find(goodfits(:,1) == pickedarray_new(jjj)),:);
    if currfrm
        pickedgoodfits = [pickedgoodfits;currfrm];
    else
        fprintf('No good fits in frame %g\n',pickedarray_new(jjj));
    end
end
pickedgoodfits(1,:) = [];


% Output picked goodfits and picking parameters

outputname = [folder filesep name '_picked.mat'];
save(outputname,'pickedgoodfits','N','track_Boolean','fits_col_headers');
```

*Published with MATLAB® R2016b*

# APPENDIX B
# Code for Chapter 4
# STORM4, plotZ_profile, newbgsSTORMfit, radial_density, simu_STORM

*STORM4*: a MATLAB main script that analyzes dSTORM data. The frames of single molecule fluorescence pulses are recorded and positions of corresponding nanoparticle are localized.

*plot_Z_profile*: a MATLAB function that plots the time trace of average pixel intensity in an indicated area.

*newbgsSTORMfit*: a MATLAB function that localizes the single molecule pulses identified in STORM4.m.

*radial_density*: a MATLAB function that plots that radial density of a density scatter plot.

*simu_STORM*: a MATLAB function that simulates the experimental dSTORM data, including localization precisions and dye molecule blinking statistics.

```
% Bing Fu, Oct. 17, 2016 This script is used in STORM analysis version
 4. This
% main script plot the time trace of the diffraction spot and manually
 pick the
% good pieces of traces and find the on-frames and the corresponding
 GNP
% position. Update Add check for GNP fitting: if the GNP in this frame
 can not
% be well fitted, stop the program OUTPUT Same as STORM.m, the
 outfiles include
% the _Time_Trace.mat, _PulsesFrameNumbers.mat and also the
 _GNP_position.mat as
% in FitGNP.m.
tic
MLE = 0;
% Whether or not fit the GNP positions using MLE (otherwise lsq
 fitting)
GNP_opt = 1;
% Two ways to fit the GNP 2D position: opt 1 - fit each individual
 frame and
% average the position; opt 2 - for dimmer GNP which is hard to be
 fitted,
% average the frames first and then fit that averaged frame
movie = 'T:\Lab Members\Bing Fu\data\2016\2016-10-24 all 80nm-30-6nm
 newest radial density plot\1024-30-6nm_18.tif';
[pr_folder, moviename, ~] = fileparts(movie);
% min_int = 100; %%% May change from movie to movie. This is the
 minimum
% intensity that will count for a molecule. %%%

[t, outtrace] = plot_Z_profile(movie, 1); % make the time trace of
 selected area which contains the GNP. %
% need to change the parameters in plot_Z_profile for each movie %
save([pr_folder filesep moviename '_Time_Trace'], 'outtrace');
toc

mk = 1;
while mk
    a = input('Does this trace look good? Y/N\n', 's');
    if a == 'N'   %% If there are some noisy trace, get rid of it
        x = input('Enter the lower range:\n');
        y = input('Enter the higher range:\n');
        t_temp = t(x:y);
    elseif a == 'Y'
        t_temp = t;
        x = 1;
        y = size(imfinfo(movie),1);
    end
    [bg, frms] = find_intensitiesV2(t_temp); % using STaSI to find the
 background level of the GNP FL
    sprintf('The background intensity is: %d', bg)
    %     thresh = bg + min_int;
```

```
    pulses_frm = frms;
    if ~isempty(pulses_frm)
        real_pulses_frm = pulses_frm + x - 1; % recover the original
 frame number from the original movie
        params = struct('PulsesFrames', real_pulses_frm);
        outfile = [pr_folder filesep moviename sprintf('_%g-
%g',x,y) '_PulsesFrameNumbers'];
        save(outfile, 'params');

        %         %% Fit the BGS movie for the indicated frames %  the
 BGS movie
        %         is a tif folder obtained by
        %         bing_separate_movies_avg_subtract_new.m and
 unstack_BingV2.m
        %
        %         mols = size(real_pulses_frm, 1); % how many pulses
 to fit
        %         foldername = 'C:\Users\bingf\Documents\STORM data
\9-29
        %         data\0929g_031_sub1\0929g_031_sub1'; % this is the
 folder that
        %         contains all the -bgs.tif allfiles =
 dir2(foldername); guess =
        %         cell(1, mols); fits = cell(1, mols); for ii = 1:mols
        %             frnum = num2str(real_pulses_frm(ii)); len =
 length(frnum);
        %             if len < 4
        %                 lead = 4 - len; pattern = [repmat('0', 1,
 lead)
        %                 frnum];
        %             else
        %                 pattern = frnum;
        %             end matching = regexp({allfiles(:).name},
 pattern);
        %             matched = find(~cellfun(@isempty,matching));
 curr_fm =
        %             [foldername filesep allfiles(matched).name]; [a,
 b] =
        %             FitSingleMol(curr_fm); guess{1, ii} = a; fits{1,
 ii} = b;
        %         end
        %
        %         guessfilename = [movie(1:end-4) sprintf('_%g-%g-
initguess', x,
        %         y)]; goodfitfilename = [movie(1:end-4)
        %         sprintf('_%g-%g-goodfit', x, y)];
 save(guessfilename,
        %         'guess'); save(goodfitfilename, 'fits');

        % Pick the corresponding background GNP frames
        temp_s = input('Enter the frame array you want to fit GNP
 bg:');
        s = temp_s + x - 1;
        msg = sprintf('Starting frame x = %d; Add this up\n', x);
```

```
        display(msg);
        GNPstr = input('Enter again:\n', 's');
        rl = length(s); % The frame length of the region, the average
position of the GNP. This is a range that is...
        % near the pulses frames and is on a flat background

        % Load the movie to find the GNP position
        if GNP_opt == 1
            sum_x = 0;
            sum_y = 0;
            for ii = 1:rl
                [guesses, goodfits] = FitSingleMol_newbgs2(movie,
s(ii), MLE);
                if goodfits == 0
                    msg = sprintf('GNP on frame %g can not be fitted.
Exit script.', s(ii));
                    display(msg);
                    return
                end
                amps = goodfits(:,3); % The third column is Gaussian
amplitude
                ind = find(amps == max(amps)); % GNP should be the
brightest if there are multiple fits
                pos_x = goodfits(ind, 9);
                pos_y = goodfits(ind, 11);
                sum_x = sum_x + pos_x;
                sum_y = sum_y + pos_y;
            end

            pos_x_avg = sum_x/rl;
            pos_y_avg = sum_y/rl;

        elseif GNP_opt == 2
            img_sum = 0;
            for ii = 1:rl
                curr_fr = imread(movie, s(ii));
                img_sum = img_sum + curr_fr;
            end
            img_avg = img_sum/rl;
            outimgname = [pr_folder filesep moviename sprintf('_%g-
%g',x,y) '_GNP_avg_img.tif'];
            imwrite(img_avg, outimgname);
            [guesses, goodfits] = FitSingleMol_newbgs2(outimgname, 1,
MLE);
            amps = goodfits(:,3); % The third column is Gaussian
amplitude
            ind = find(amps == max(amps)); % GNP should be the
brightest if there are multiple fits
            pos_x_avg = goodfits(ind, 9);
            pos_y_avg = goodfits(ind, 11);
        end

        [folder, filename, ~] = fileparts([outfile '.mat']);
        base = filename(1: end-19);
```

```
        output = struct('GNP_frame_array', GNPstr, 'X_position',
 pos_x_avg, 'Y_position', pos_y_avg);
        save([folder filesep base '_GNP_position'], 'output');
    else
        display('There are no pulses in this trace!');
    end
    mk = input('Do you want to analyze another piece of trace? 1 for
 Yes/0 for No\n');
    if mk
        clf
        plot(t);
    end
end
```

*Published with MATLAB® R2016b*

```
function [t, plotparam] = plot_Z_profile(fd, opt)
% fd is the tif or folder of the raw movie;opt 1 - square; opt 2 -
 rectangle.
% Similar to the "plot Z-axis profile" plug-in in ImageJ, plot the
 time trace of
% a movie tiff stack in one folder for any given area (average
 intensity. Load
% the tiff stack frames
clc
clf
% fd = 'T:\Lab Members\Bing Fu\data\2016\2016-3-15\new A-P 10X(reused)
 001';
corn_x = 27; % for opt 1 and 2
corn_y = 37; % for opt 1 and 2
squaresize = 9; % for opt 1
width = 20; % for opt 2
height = 16; % for opt 2

[folder, name, ~] = fileparts(fd);
if isdir(fd)
    cont = dir2(fd);
    frmsnum = size(cont, 1); % number of frames
    t = zeros(frmsnum, 1);
    for ii = 1: frmsnum
        FrameCounter(1, frmsnum, ii, 1);
        a = [fd filesep cont(ii).name];
        currfr = double(imread(a));
        if opt == 1 % option 1 is a square region whose upper left
 corner coordinate is given
            corn = [corn_x corn_y];
            up = corn(2);
            bottom = corn(2) + squaresize - 1;
            left = corn(1);
            right = corn(1) + squaresize - 1;
        else if opt == 2 % option 2 is a rectangular region whose
 upper left corner coordinate is given
                corn = [corn_x corn_y];
                up = corn(2);
                bottom = corn(2) + height - 1;
                left = corn(1);
                right = corn(1) + width - 1;
            end
        end
        % calculate the average intensity within the indicated region
        avg = mean(mean(currfr(up:bottom, left:right)));
        t(ii) = avg;
    end
else if fd(end-3:end) == '.tif'
        a = imfinfo(fd);
        frmsnum = size(a, 1); % number of frames
        t = zeros(frmsnum, 1);
        for ii = 1: frmsnum
```

```
            currfr = double(imread(fd, ii));
            FrameCounter(1, frmsnum, ii, 1);
            if opt == 1 % option 1 is a square region whose upper left
 corner coordinate is given
                corn = [corn_x corn_y];
                up = corn(2);
                bottom = corn(2) + squaresize - 1;
                left = corn(1);
                right = corn(1) + squaresize - 1;
            else if opt == 2 % option 2 is a rectangular region whose
 upper left corner coordinate is given
                    corn = [corn_x corn_y];
                    up = corn(2);
                    bottom = corn(2) + height - 1;
                    left = corn(1);
                    right = corn(1) + width - 1;
                end
            end
            % calculate the average intensity within the indicated
 region
            avg = mean(mean(currfr(up:bottom, left:right)));
            t(ii) = avg;
        end
    end
end

plot(t);
hold off
% saveas(gcf, [folder filesep name '.png']);

% Prepare output file
if opt == 1
    plotparam = struct('Time_Trace', t, 'Corner_X',
 corn_x, 'Corner_Y', corn_y, ...
        'Square_Size', squaresize);
elseif opt == 2
    plotparam = struct('Time_Trace', t, 'Corner_X',
 corn_x, 'Corner_Y', corn_y, ...
        'Width', width, 'Height', height);
end

end
```

*Published with MATLAB® R2016b*

```
function newbgsSTORMfit(folder)
% This function fits the bgs-frames from bgs_Bing_loop.m.
% INPUT
% folder: the full path of the folder that contains all the bgs
 folders and the
% corresponding _PulsesFrameNumbers.mat files to locate which frames
 to be
% fitted
% OUTPUT
% .mat files that contains the guesses and goodfits data as before.
MLE = 0;
cd(folder)
allmat = dir('*.mat');
allmat_num = size(allmat, 1);
for ii = 1:allmat_num
    if size(allmat(ii).name, 2) > 23
        curr_file = allmat(ii).name;
        if strcmp(curr_file(end-22:end), '_PulsesFrameNumbers.mat')
            basename = curr_file(1:end-23);
            bgs_fd = [folder filesep basename];
            if exist(bgs_fd, 'dir') ~= 7
                msg = sprintf('The corresponding bgs folder for %s do
 not exist!', basename);
                display(msg);
            else
                % The movie name is the part that before the last
 underscore in
                % basename.
                ind = find(basename == '_', 1, 'last');
                mv_name = basename(1:ind-1);
                % Load the on-frames from the pulse file
                onfr = load([folder filesep curr_file]);
                onframe_array = onfr.params.PulsesFrames;
                onfr_num = size(onframe_array,1);
                guess = cell(1, onfr_num);
                fits = cell(1, onfr_num);
                for jj = 1:onfr_num
                    curr_bgs_fr = [bgs_fd filesep sprintf('%s_%d-
bgs.tif', mv_name, onframe_array(jj))];
                    [a, b] = FitSingleMol_newbgs(curr_bgs_fr,MLE);
                    guess{1, jj} = a;
                    fits{1, jj} = b;
                end
                if MLE ~= 1
                    guessfilename = [folder filesep basename '-
initguess-newbgs'];
                    goodfitfilename = [folder filesep basename '-
goodfit-newbgs'];
                elseif MLE == 1
                    guessfilename = [folder filesep basename '-
initguess-newbgs-MLE'];
```

```
                    goodfitfilename = [folder filesep basename '-
goodfit-newbgs-MLE'];
                end
                save(guessfilename, 'guess');
                save(goodfitfilename, 'fits');
            end
        end
    end
end
end
```

*Published with MATLAB® R2016b*

```
% Bing Fu, August 11, 2016
function r_density = radial_density(ref_x, ref_y, fitspos_x,
 fitspos_y, out)
% Plot the radial density of localizations using values from
 scatplot.m Break
% down the density plot radially and caculate the average of density
 at each
% radial distance. INPUT The input is from the output of Plot_map
 (only the
% localizations inside the GNP-DNA circle, no outsider points). ref_x:
 reference
% GNP x position from Plot_map.m (in pixel) ref_y: reference GNP y
 position from
% Plot_map.m (in pixel) fitspos_x: all localization position x pixel
 fitspos_y:
% all localization position y pixel out: output from function
 scatplot.m OUTPUT
% r_density is a N by 6 double matrix. 1st comlum: radius in nm; 2nd:
 sum of
% density value from out.ddf in this ring region; 3rd: how many
 localizations
% are in this ring region; 4th: averaged radial density in this ring
 region;
% 5th: normalized averaged radial density; 6th: distance/total
 radius(GNP+DNA)
% percent. Plot the 5th column vs. 1th columm or 6th column
 (normalized by the
% particle size).

pixel = 49; % Pixel size (nm)
GNP_rad = 40; % GNP radius in nanometer
DNA = 32.6; % dsDNA spacer length in nanometer
r_tot = GNP_rad + DNA; % unit: nm
r_inc = 2; % nm of radius increase in each sampling ring
total_loc = size(fitspos_x, 1);
num_point = round(r_tot/r_inc) + 30;
r_density = zeros(num_point, 6); % The third column is used to record
 how many localizations in this region
r_density(1:num_point, 1) = r_inc:r_inc:(num_point*r_inc);
r_density(1:num_point, 6) = [(r_inc/r_tot):(r_inc/r_tot):
(num_point*r_inc/r_tot)];
for ii = 1: total_loc
    curr_x = fitspos_x(ii);
    curr_y = fitspos_y(ii);
    curr_den = out.ddf(ii);
    r = sqrt((curr_x - ref_x)^2 + (curr_y - ref_y)^2); % in pixel
    r_nm = r*pixel; % in nm
    ind = floor(r_nm/r_inc)+1;
    r_density(ind,2) = r_density(ind, 2) + curr_den;
    r_density(ind,3) = r_density(ind, 3) + 1;

end
```

```
r_density(:,4) = r_density(:,2)./r_density(:,3); % radial density
r_density(:,5) = r_density(:,4)/max(r_density(:,4)); % normalized
 radial density
plot(r_density(:,1), r_density(:,4), 'r', 'LineWidth', 2);
end
```

*Published with MATLAB® R2016b*

```
function [allx, ally, all_out, r_den, r] = simu_STORM(r, opt)
% Bing Fu, Sept. 21, 2016
% Simulate my STORM experiment: molecules are on a surface of a sphere
 with
% radius r; each molecule emissions are localized several times
 (corresponds to
% several on-frames) within precission of certain Gaussian-shape
 probability.
% Simulate the localization map and also the radial density plot to
 compare with
% the experimental data.
% INPUT
% r: the radius of sphere in nanometer
% opt: option 1 - my twoDprojection.m code to generate the dots
 positions
% option 2 - RandSampleSphere.m to generate the dots positions
pixel = 49; % Pixel size in nanometer
sigma = 0.45; % Localization precision in pixel
pd = makedist('Exponential', 'mu', 16.9);
% The number of localizations of each molecule has exponential
 probability, with
% mean of 16.9 (from fit of real data)
allx = zeros(100000,1);
ally = zeros(100000,1);
count = 1;

r_tot = r; % unit: nm
r_inc = 2; % nm of radius increase in each sampling ring
num_point = round(r_tot/r_inc) + 100;
r_den = zeros(num_point, 2);
r_den(1:num_point, 1) = r_inc:r_inc:(num_point*r_inc);
switch opt
    case 1
        N = 16;
        P = 16;
        r_pix = r/pixel;
        [x, y] = twoDprojection(r_pix,N,P);
        mol_num = size(x,1);
        for ii = 1:mol_num
            on_frames = round(random(pd));
            if on_frames >= 8
                Rx = normrnd(x(ii),sigma, [on_frames, 1]);
                Ry = normrnd(y(ii),sigma, [on_frames, 1]);
                out = scatplot(Rx,Ry, 'circles', 0.5, 100, 5, 1, 25);
                axis equal
                curr_r_den = radial_density(0, 0, Rx, Ry, out);
                curr_r_den(isnan(curr_r_den)) = 0;
                r_den(1:num_point, 2) = r_den(1:num_point,2) +
 curr_r_den(:,4);
                allx(count:count+on_frames-1) = Rx;
                ally(count:count+on_frames-1) = Ry;
                count = count + on_frames;
```

```
           end
       end
       allx(count:end) = [];
       ally(count:end) = [];
       scatter(allx,ally);
       all_out = scatplot(allx,ally, 'circles', 0.5, 100, 5, 1, 25);
       xlabel('Pixel');
       ylabel('Pixel');
       axis equal
       % Draw circle (the sphere prejection) where the molecules
locate
       hold on
       th = 0:pi/50:2*pi;
       xunit_GNP = r/pixel*cos(th);
       yunit_GNP = r/pixel*sin(th);
       plot(xunit_GNP, yunit_GNP, 'r', 'LineWidth', 2);
       figure
       plot(r_den(:,1),r_den(:,2));
       xlabel('nm');
       ylabel('Radial density');
   case 2
       X = RandSampleSphere(150,'uniform');
       X = X.*r/pixel;
       mol_num = size(X,1);
       for ii = 1:mol_num
           on_frames = round(random(pd));
           if on_frames >= 8
               Rx = normrnd(X(ii,1),sigma, [on_frames, 1]);
               Ry = normrnd(X(ii,2),sigma, [on_frames, 1]);
               out = scatplot(Rx,Ry, 'circles', 0.5, 100, 5, 1, 25);
               axis equal
               curr_r_den = radial_density(0, 0, Rx, Ry, out);
               curr_r_den(isnan(curr_r_den)) = 0;
               r_den(1:num_point, 2) = r_den(1:num_point,2) +
curr_r_den(:,4);
               allx(count:count+on_frames-1) = Rx;
               ally(count:count+on_frames-1) = Ry;
               count = count + on_frames;
           end
       end
       allx(count:end) = [];
       ally(count:end) = [];
       scatter(allx,ally);
       all_out = scatplot(allx,ally, 'circles', 0.5, 100, 5, 1, 25);
       xlabel('Pixel');
       ylabel('Pixel');
       axis equal
       % Draw circle (the sphere prejection) where the molecules
locate
       hold on
       th = 0:pi/50:2*pi;
       xunit_GNP = r/pixel*cos(th);
       yunit_GNP = r/pixel*sin(th);
       plot(xunit_GNP, yunit_GNP, 'r', 'LineWidth', 2);
```

```
        figure
        plot(r_den(:,1),r_den(:,2));
        xlabel('nm');
        ylabel('Probability of emission position');
end
```

*Published with MATLAB® R2016b*

# Bibliography

[1] G. B. Airy, "On the Diffraction of an Object-glass with a Circular Aperture," *Transactions of the Cambridge Philosophical Society*, vol. 5, pp. 283–291, 1835.

[2] H. H. Tuson and J. S. Biteen, "Unveiling the inner workings of live bacteria using super-resolution microscopy," *Analytical Chemistry*, vol. 87, no. 1, pp. 42–63, 2015.

[3] M. Hayat, *Principles and Techniques of Electron Microscopy: Biological Applications.* Van Nostrand Reinhold Inc.,U.S, 1971.

[4] T. Cordes and S. A. Blum, "Opportunities and challenges in single-molecule and single-particle fluorescence microscopy for mechanistic studies of chemical reactions," *Nature Chemistry*, vol. 5, no. 12, pp. 993–999, 2013.

[5] M. B. J. Roeffaers, G. D. Cremer, H. Uji-i, B. F. Sels, P. A. Jacobs, F. C. D. Schryver, D. E. D. Vos, and J. Hofkens, "Single-molecule fluorescence spectroscopy in (bio) catalysis," *Proceedings of the National Academy of Sciences*, vol. 104, no. 31, pp. 12603–12609, 2007.

[6] N. M. Esfandiari and S. A. Blum, "Homogeneous vs heterogeneous polymerization catalysis revealed by single-particle fluorescence microscopy," *Journal of the American Chemical Society*, vol. 133, no. 45, pp. 18145–18147, 2011.

[7] M. B. J. Roeffaers, B. F. Sels, H. Uji-I, F. C. De Schryver, P. a. Jacobs, D. E. De Vos, and J. Hofkens, "Spatially resolved observation of crystal-face-dependent catalysis by single turnover counting," *Nature*, vol. 439, no. 7076, pp. 572–575, 2006.

[8] A. Kiel, J. Kovacs, A. Mokhir, R. Krämer, and D. P. Herten, "Direct monitoring of formation and dissociation of individual metal complexes by single-molecule fluorescence spectroscopy," *Angewandte Chemie - International Edition*, vol. 46, no. 18, pp. 3363–3366, 2007.

[9] J. B. Pawley, *Handbook of Biological Confocal Microscopy.* Springer, 2006.

[10] S. W. Hell and J. Wichmann, "Breaking the Diffraction Resolution Limit By Stimulated-Emission - Stimulated-Emission-Depletion Fluorescence Microscopy," *Optics Letters*, vol. 19, no. 11, pp. 780–782, 1994.

[11] T. A.Klar and S. W. Hell, "Subdiffraction resolution in far-field fluorescence microscopy.," *Optics letters*, vol. 24, no. 14, pp. 954–956, 1999.

[12] E. Betzig, G. H. Patterson, R. Sougrat, O. W. Lindwasser, S. Olenych, J. S. Bonifacino, M. W. Davidson, J. Lippincott-Schwartz, and H. F. Hess, "Imaging intracellular fluorescent proteins at nanometer resolution.," *Science*, vol. 313, no. 5793, pp. 1642–1645, 2006.

[13] S. T. Hess, T. P. Girirajan, and M. D. Mason, "Ultra-High Resolution Imaging by Fluorescence Photoactivation Localization Microscopy," *Biophysical Journal*, vol. 91, no. 11, pp. 4258–4272, 2006.

[14] M. J. Rust, M. Bates, and X. Zhuang, "Sub-diffraction-limit imaging by stochastic optical reconstruction microscopy (STORM)," *Nature Methods*, vol. 3, no. 10, pp. 793–795, 2006.

[15] M. Heilemann, S. Van De Linde, M. Schüttpelz, R. Kasper, B. Seefeldt, A. Mukherjee, P. Tinnefeld, and M. Sauer, "Subdiffraction-resolution fluorescence imaging with conventional fluorescent probes," *Angewandte Chemie - International Edition*, vol. 47, no. 33, pp. 6172–6176, 2008.

[16] M. Heilemann, S. Van De Linde, A. Mukherjee, and M. Sauer, "Super-resolution imaging with small organic fluorophores," *Angewandte Chemie - International Edition*, vol. 48, no. 37, pp. 6903–6908, 2009.

[17] S. W. Hell and M. Kroug, "Ground-state-depletion fluorescence microscopy: a concept for breaking the diffracition resolution limit," *Applied Physics B: Lasers and Optics*, vol. 60, pp. 495–497, 1995.

[18] J. Fölling, M. Bossi, H. Bock, R. Medda, C. A. Wurm, B. Hein, S. Jakobs, C. Eggeling, and S. W. Hell, "Fluorescence nanoscopy by ground-state depletion and single-molecule return," *Nature Methods*, vol. 5, no. 11, pp. 943–945, 2008.

[19] A. Sharonov and R. M. Hochstrasser, "Wide-field subdiffraction imaging by accumulated binding of diffusing probes," *Proceedings of the National Academy of Sciences*, vol. 103, no. 50, pp. 18911–18916, 2006.

[20] R. Jungmann, M. S. Avendaño, M. Dai, J. B. Woehrstein, S. S. Agasti, Z. Feiger, A. Rodal, and P. Yin, "Quantitative super-resolution imaging with qPAINT," *Nature Methods*, vol. 13, no. 5, pp. 439–442, 2016.

[21] G. Giannone, E. Hosy, F. Levet, A. Constals, K. Schulze, A. I. Sobolevsky, M. P. Rosconi, E. Gouaux, R. Tampe, D. Choquet, and L. Cognet, "Dynamic superresolution imaging of endogenous proteins on living cells at ultra-high density," *Biophysical Journal*, vol. 99, no. 4, pp. 1303–1310, 2010.

[22] W. E. Moerner, "Single-molecule mountains yield nanoscale cell images," *Nature Methods*, vol. 3, no. 10, pp. 781–782, 2006.

[23] J. Gelles, B. J. Schnapp, and M. P. Sheetz, "Tracking kinesin-driven movements with nanometre-scale precision," *Nature*, vol. 331, no. 6155, pp. 450–453, 1988.

[24] A. van Oijen, J. Köhler, J. Schmidt, M. Müller, and G. Brakenhoff, "3-Dimensional super-resolution by spectrally selective imaging," *Chemical Physics Letters*, vol. 292, no. 1-2, pp. 183–187, 1998.

[25] R. E. Thompson, D. R. Larson, and W. W. Webb, "Precise nanometer localization analysis for individual fluorescent probes," *Biophysical journal*, vol. 82, no. 5, pp. 2775–2783, 2002.

[26] E. Ambrose, "A Surface Contact Microscope for the study of Cell Movements," 1956.

[27] D. Axelrod, "Cell-substrate Contacts Illuminated by Total-Internal Reflection Fluorescence," *Journal of Cell Biology*, vol. 89, no. 9, pp. 141–145, 1981.

[28] Y. Sako, S. Minoghchi, and T. Yanagida, "Single-molecule imaging of EGFR signalling on the surface of living cells," *Nature Cell Biology*, vol. 2, no. 3, pp. 168–172, 2000.

[29] M. Tokunaga, N. Imamoto, and K. Sakata-Sogawa, "Highly inclined thin illumination enables clear single-molecule imaging in cells," *Nature Methods*, vol. 5, no. 2, pp. 159–161, 2008.

[30] W. R. Legant, L. Shao, J. B. Grimm, T. A. Brown, D. E. Milkie, B. B. Avants, L. D. Lavis, and E. Betzig, "High-density three-dimensional localization microscopy across large volumes," *Nature Methods*, vol. 13, no. January, pp. 1–9, 2016.

[31] S. W. Hell, E. H. Stelzer, S. Lindek, and C. Cremer, "Confocal microscopy with an increased detection aperture: type-B 4Pi confocal microscopy," *Optics letters*, vol. 19, no. 3, pp. 222–224, 1994.

[32] R. Schmidt, C. A. Wurm, S. Jakobs, J. Engelhardt, A. Egner, and S. W. Hell, "Spherical nanosized focal spot unravels the interior of cells," *Nature Methods*, vol. 5, no. 6, pp. 539–544, 2008.

[33] U. Böhm, S. W. Hell, and R. Schmidt, "4Pi-RESOLFT nanoscopy," *Nature Communications*, vol. 7, pp. 10504–10511, 2016.

[34] F. Huang, G. Sirinakis, E. S. Allgeyer, L. K. Schroeder, W. C. Duim, E. B. Kromann, T. Phan, F. E. Rivera-Molina, J. R. Myers, I. Irnov, M. Lessard, Y. Zhang, M. A. Handel, C. Jacobs-Wagner, C. P. Lusk, J. E. Rothman, D. Toomre, M. J. Booth, and J. Bewersdorf, "Ultra-High Resolution 3D Imaging of Whole Cells," *Cell*, vol. 166, no. 4, pp. 1028–1040, 2016.

[35] B. Huang, W. Wang, M. Bates, and X. Zhuang, "Three-dimensional super-resolution imaging by stochastic optical reconstruction microscopy.," *Science*, vol. 319, no. 5864, pp. 810–813, 2008.

[36] S. R. P. Pavani, M. A. Thompson, J. S. Biteen, S. J. Lord, N. Liu, R. J. Twieg, R. Piestun, and W. E. Moerner, "Three-dimensional, single-molecule fluorescence imaging beyond the diffraction limit by using a double-helix point spread function," *Proceedings of the National Academy of Sciences*, vol. 106, no. 9, pp. 2995–2999, 2009.

[37] D. Aquino, A. Schönle, C. Geisler, C. V. Middendorff, C. A. Wurm, Y. Okamura, T. Lang, S. W. Hell, and A. Egner, "Two-color nanoscopy of three-dimensional volumes by 4Pi detection of stochastically switched fluorophores," *Nature Methods*, vol. 8, no. 4, pp. 353–359, 2011.

[38] F. Huang, T. M. P. Hartwich, F. E. Rivera-Molina, Y. Lin, W. C. Duim, J. J. Long, P. D. Uchil, J. R. Myers, M. a. Baird, W. Mothes, M. W. Davidson, D. Toomre, and J. Bewersdorf, "Video-rate nanoscopy using sCMOS camera-specific single-molecule localization algorithms," *Nature Methods*, vol. 10, no. 7, pp. 653–658, 2013.

[39] K. I. Willig, S. O. Rizzoli, V. Westphal, R. Jahn, and S. W. Hell, "STED microscopy reveals that synaptotagmin remains clustered after synaptic vesicle exocytosis," *Nature*, vol. 440, no. 7086, pp. 935–939, 2006.

[40] M. B. Stone, S. A. Shelby, and S. L. Veatch, "Super-Resolution Microscopy: Shedding Light on the Cellular Plasma Membrane," *Chemical Reviews*, 2017.

[41] J. Nixon-Abell, C. J. Obara, A. V. Weigel, D. Li, W. R. Legant, C. S. Xu, H. A. Pasolli, K. Harvey, H. F. Hess, E. Betzig, C. Blackstone, and J. Lippincott-Schwartz, "Increased spatiotemporal resolution reveals highly dynamic dense tubular matrices in the peripheral ER," *Science*, vol. 354, no. 6311, pp. aaf3928–aaf3928, 2016.

[42] Y. Liao, J. W. Schroeder, B. Gao, L. A. Simmons, and J. S. Biteen, "Single-molecule motions and interactions in live cells reveal target search dynamics in mismatch repair," *Proceedings of the National Academy of Sciences*, vol. 112, no. 50, pp. 6898–6906, 2015.

[43] K. S. Karunatilaka, E. A. Cameron, E. C. Martens, N. M. Koropatkin, and S. Biteen, "Superresolution Imaging Captures Carbohydrate Utilization Dynamics in Human Gut Symbionts," *mBio*, vol. 5, no. 6, pp. 1–10, 2014.

[44] B. L. Haas, J. S. Matson, V. J. Dirita, and J. S. Biteen, "Single-molecule tracking in live Vibrio cholerae reveals that ToxR recruits the membrane-bound virulence regulator TcpP to the toxT promoter," *Molecular Microbiology*, vol. 96, no. 1, pp. 4–13, 2015.

[45] Y. Liao, S. K. Yang, K. Koh, A. J. Matzger, and J. S. Biteen, "Heterogeneous single-molecule diffusion in one-, two-, and three-dimensional microporous coordination polymers: Directional, trapped, and immobile guests," *Nano Letters*, vol. 12, no. 6, pp. 3080–3085, 2012.

[46] E. Wertz, B. P. Isaacoff, J. D. Flynn, and J. S. Biteen, "Single-Molecule Super-Resolution Microscopy Reveals How Light Couples to a Plasmonic Nanoantenna on the Nanometer Scale," *Nano Letters*, vol. 15, pp. 2662–2670, 2015.

[47] J. E. Donehue, E. Wertz, C. N. Talicska, and J. S. Biteen, "Plasmon-Enhanced Brightness and Photostability from Single Fluorescent Proteins Coupled to Gold Nanorods," *Journal of Physical Chemistry C*, vol. 118, no. 27, pp. 15027–15035, 2014.

[48] B. Fu, J. D. Flynn, B. P. Isaacoff, D. J. Rowland, and J. S. Biteen, "Super-Resolving the Distance-Dependent Plasmon-Enhanced Fluorescence of Single Dye and Fluorescent Protein Molecules," *Journal of Physical Chemistry C*, vol. 119, no. 33, pp. 19350–19358, 2015.

[49] E. A. Wertz, B. P. Isaacoff, and J. S. Biteen, "Wavelength-Dependent Super-resolution Images of Dye Molecules Coupled to Plasmonic Nanotriangles," *ACS Photonics*, vol. 3, no. 10, pp. 1733–1740, 2016.

[50] N. Panchuk-Voloshina, R. P. Haugland, J. Bishop-Stewart, M. K. Bhalgat, P. J. Millard, F. Mao, W. Y. Leung, and R. P. Haugland, "Alexa dyes, a series of new fluorescent dyes that yield exceptionally bright, photostable conjugates," *J. Histochem. Cytochem.*, vol. 47, no. 9, pp. 1179–1188, 1999.

[51] K. Lidke, B. Rieger, T. Jovin, and R. Heintzmann, "Superresolution by localization of quantum dots using blinking statistics," *Optics Express*, vol. 13, no. 18, pp. 7052–7062, 2005.

[52] X. Nan, P. A. Sims, P. Chen, and X. Sunney Xie, "Observation of individual microtubule motor steps in living cells with endocytosed quantum dots," *Journal of Physical Chemistry B*, vol. 109, no. 51, pp. 24220–24224, 2005.

[53] M. Bruchez Jr., M. Moronne, P. Gin, S. Weiss, and A. P. Alivisatos, “Semiconductor Nanocrystals as Fluorescent Biological Labels,” *Science*, vol. 281, no. 5385, pp. 2013–2016, 1998.

[54] W. C. W. Chan and S. Nie, “Quantum Dot Bioconjugates for Ultrasensitive Nonisotopic Detection,” *Science*, vol. 281, no. 5385, pp. 2016–2018, 1998.

[55] U. Resch-Genger, M. Grabolle, S. Cavaliere-Jaricot, R. Nitschke, and T. Nann, “Quantum dots versus organic dyes as fluorescent labels,” *Nature Methods*, vol. 5, no. 9, pp. 763–775, 2008.

[56] W. Liu, M. Howarth, A. B. Greytak, Y. Zheng, D. G. Nocera, A. Y. Ting, and M. G. Bawendi, “Article Compact Biocompatible Quantum Dots Functionalized for Cellular Imaging Compact Biocompatible Quantum Dots Functionalized for Cellular Imaging,” *Journal of the American Chemical Society*, vol. 130, no. 11, pp. 1274–1284, 2008.

[57] M. Howarth, K. Takao, Y. Hayashi, and A. Y. Ting, “Targeting quantum dots to surface proteins in living cells with biotin ligase,” *Proceedings of the National Academy of Sciences*, vol. 102, no. 21, pp. 7583–7588, 2005.

[58] R. Y. Tsien, “The Green Fluorescent Protein,” *Annual Review of Biochemistry*, vol. 67, pp. 509–544, 1998.

[59] J. Zhang, R. E. Campbell, A. Y. Ting, and R. Y. Tsien, “Creating new fluorescent probes for cell biology,” *Nature reviews. Molecular cell biology*, vol. 3, no. 12, pp. 906–918, 2002.

[60] A. Gahlmann and W. E. Moerner, “Exploring bacterial cell biology with single-molecule tracking and super-resolution imaging,” *Nature reviews. Microbiology*, vol. 12, no. 1, pp. 9–22, 2014.

[61] P. L. Choyke, R. Alford, H. M. Simpson, J. Duberman, G. Craig Hill, M. Ogawa, C. Regino, and H. Kobayashi, “Toxicity of organic fluorophores used in molecular imaging: Literature review,” *Molecular Imaging*, vol. 8, no. 6, pp. 341–354, 2009.

[62] X. Shu, N. C. Shaner, C. A. Yarbrough, R. Y. Tsien, and S. J. Remington, “Novel Chromophores and Buried Charges Control Color in mFruits,” *Biochemistry*, vol. 45, no. 32, pp. 9639–9647, 2006.

[63] F. M. Raymo, “Photoactivatable Synthetic Dyes for Fluorescence Imaging at the Nanoscale,” *Journal of Physical Chemistry Letters*, vol. 3, pp. 2379–2385, 2012.

[64] S. K. Yang, X. Shi, S. Park, T. Ha, and S. C. Zimmerman, “A dendritic single-molecule fluorescent probe that is monovalent, photostable and minimally blinking,” *Nature Chemistry*, vol. 5, pp. 692–697, 2013.

[65] W. Q. Ong, Y. R. Citron, J. Schnitzbauer, D. Kamiyama, and B. Huang, “Heavy water: a simple solution to increasing the brightness of fluorescent proteins in super-resolution imaging,” *Chemical Communications*, vol. 51, no. 70, pp. 13451–13453, 2015.

[66] J. C. Vaughan, S. Jia, and X. Zhuang, “Ultrabright photoactivatable fluorophores created by reductive caging,” *Nature Methods*, vol. 9, no. 12, pp. 1181–1184, 2012.

[67] K. A. Willets and R. P. Van Duyne, “Localized surface plasmon resonance spectroscopy and sensing,” *Annual Review of Physical Chemistry*, vol. 58, pp. 267–297, 2007.

[68] L. J. E. Anderson, Y. R. Zhen, C. M. Payne, P. Nordlander, and J. H. Hafner, “Gold nanobelts as high confinement plasmonic waveguides,” *Nano Letters*, vol. 13, no. 12, pp. 6256–6261, 2013.

[69] J. Olson, A. Manjavacas, T. Basu, D. Huang, A. E. Schlather, B. Zheng, N. J. Halas, P. Nordlander, and S. Link, “High Chromaticity Aluminum Plasmonic Pixels for Active Liquid Crystal Displays,” *ACS Nano*, vol. 10, pp. 1108–1117, 2016.

[70] M. P. Backlund, A. Arbabi, P. N. Petrov, E. Arbabi, S. Saurabh, A. Faraon, and W. E. Moerner, “Removing orientation-induced localization biases in single-molecule microscopy using a broadband metasurface mask,” *Nature Photonics*, vol. 10, pp. 459–462, 2016.

[71] M. Khorasaninejad, W. T. Chen, R. C. Devlin, J. Oh, A. Y. Zhu, and F. Capasso, “Metalenses at visible wavelengths: Diffraction-limited focusing and subwavelength resolution imaging,” *Science*, vol. 352, no. 6290, pp. 1190–1194, 2016.

[72] C. Xie, L. Hanson, Y. Cui, and B. Cui, “Vertical nanopillars for highly localized fluorescence imaging,” *Proceedings of the National Academy of Sciences*, vol. 108, no. 10, pp. 3894–3899, 2011.

[73] V. Flauraud, T. S. Van Zanten, M. Mivelle, C. Manzo, M. Garcia-Parajo, and J. Brugger, “Large scale arrays of bowtie nanoaperture antennas for nanoscale dynamics in living cell membranes,” *Nano Letters*, vol. 15, pp. 4176–4182, 2015.

[74] L. Su, H. Yuan, G. Lu, S. Rocha, M. Orrit, J. Hofkens, and H. Uji-i, “Super-resolution Localization and Defocused Fluorescence Microscopy on Resonantly Coupled Single-Molecule, Single-Nanorod Hybrids,” *ACS Nano*, vol. 10, no. 2, pp. 2455–2466, 2016.

[75] S. Xu, Y. Cao, J. Zhou, X. Wang, X. Wang, and W. Xu, "Plasmonic enhancement of fluorescence on silver nanoparticle films.," *Nanotechnology*, vol. 22, no. 27, pp. 275715–275721, 2011.

[76] M. W. Knight, N. S. King, L. Liu, H. O. Everitt, P. Nordlander, and N. J. Halas, "Aluminum for Plasmonics," *ACS Nano*, vol. 8, no. 1, pp. 834–840, 2014.

[77] H. Cang, A. Labno, C. Lu, X. Yin, M. Liu, C. Gladden, Y. Liu, and X. Zhang, "Probing the elctromagnetic field of a 15-nanometre hotspot by single molecule imaging," *Nature*, vol. 469, pp. 385–388, 2011.

[78] G. V. Naik, V. M. Shalaev, and A. Boltasseva, "Alternative plasmonic materials: beyond gold and silver," *Advanced Materials*, vol. 25, no. 24, pp. 3264–3294, 2013.

[79] C. L. Haynes and R. P. Van Duyne, "Nanosphere Lithography: A Versatile Nanofabrication Tool for Studies of Size-Dependent Nanoparticle Optics Christy," *Journal of Physical Chemistry B*, vol. 105, pp. 5599–5611, 2001.

[80] S. A. Lee, A. Ponjavic, C. Siv, S. F. Lee, and J. S. Biteen, "Nanoscopic Cellular Imaging: Confinement Broadens Understanding," *ACS Nano*, vol. 10, no. 9, pp. 8143–8153, 2016.

[81] J. R. Lakowicz, *Principles of Fluorescence Spectroscopy Principles of Fluorescence Spectroscopy*. Springer, 2006.

[82] G. Sun, J. B. Khurgin, and R. A. Soref, "Practical enhancement of photoluminescence by metal nanoparticles," *Applied Physics Letters*, vol. 94, pp. 1–4, 2009.

[83] S. Nie and S. Emory, "Probing Single Molecules and Single Nanoparticles by Surface-Enhanced Raman Scattering," *Science*, vol. 275, pp. 1102–1106, 1997.

[84] V. E. Ferry, Luke A. Sweatlock, D. Pacifici, and H. A. Atwater, "Plasmonic Nanostructure Design for Efficient Light Coupling into Solar Cells," *Nano letters*, vol. 8, no. 12, pp. 4391–4397, 2009.

[85] V. E. Ferry, M. A. Verschuuren, H. B. T. Li, E. Verhagen, R. J. Walters, R. E. I. Schropp, H. A. Atwater, and A. Polman, "Light trapping in ultrathin plasmonic solar cells," *Optics Express*, vol. 18, pp. 237–245, 2010.

[86] P. N. Saeta, V. E. Ferry, D. Pacifici, J. N. Munday, and H. A. Atwater, "How much can guided modes enhance absorption in thin solar cells?," *Optics Express*, vol. 17, no. 23, pp. 20975–20990, 2009.

[87] M. Bauch, K. Toma, M. Toma, Q. Zhang, and J. Dostalek, “Plasmon-Enhanced Fluorescence Biosensors: a Review,” *Plasmonics*, vol. 9, pp. 781–799, 2014.

[88] C. Höppener and L. Novotny, “Exploiting the light-metal interaction for biomolecular sensing and imaging,” *Quarterly Reviews of Biophysics*, vol. 45, no. 02, pp. 209–255, 2012.

[89] J. R. Lakowicz, K. Ray, M. Chowdhury, H. Szmacinski, Y. Fu, J. Zhang, and K. Nowaczyk, “Plasmon-controlled fluorescence: a new paradigm in fluorescence spectroscopy,” *The Analyst*, vol. 133, no. 10, pp. 1308–1346, 2008.

[90] C. E. Aitken, R. A. Marshall, and J. D. Puglisi, “An oxygen scavenging system for improvement of dye stability in single-molecule fluorescence experiments,” *Biophysical Journal*, vol. 94, no. 5, pp. 1826–1835, 2008.

[91] I. Rasnik, S. A. McKinney, and T. Ha, “Nonblinking and long-lasting single-molecule fluorescence imaging.,” *Nature Methods*, vol. 3, no. 11, pp. 891–893, 2006.

[92] L. Novotny and B. Hecht, *Principles of Nano-Optics*. Cambridge U. Press, New York, 2006.

[93] S. Khatua, P. M. R. Paulo, H. Yuan, A. Gupta, P. Zijlstra, and M. Orrit, “Resonant plasmonic enhancement of single-molecule fluorescence by individual gold nanorods,” *ACS Nano*, vol. 8, no. 5, pp. 4440–4449, 2014.

[94] A. Rose, T. B. Hoang, F. McGuire, J. J. Mock, C. Ciracì, D. R. Smith, and M. H. Mikkelsen, “Control of Radiative Processes Using Tunable Plasmonic Nanopatch Antennas,” *Nano Letters*, vol. 14, pp. 4797–4802, 2014.

[95] C. Zhao, Y. Liu, J. Yang, and J. Zhang, “Single-molecule Detection and Radiation Control in Solutions at High Concentrations via a Heterogeneous Optical Slot Antenna,” *Nanoscale*, vol. 6, pp. 9103–9109, 2014.

[96] Y. Liu, L. Blanchfield, V. P.-Y. Ma, R. Andargachew, K. Galior, Z. Liu, B. Evavold, and K. Salaita, “DNA-based nanoparticle tension sensors reveal that T-cell receptors transmit defined pN forces to their antigens for enhanced fidelity.,” *Proceedings of the National Academy of Sciences*, vol. 113, no. 20, pp. 5610–5615, 2016.

[97] D. L. Mack, E. Corte, V. Giannini, P. Török, T. Roschuk, and S. A. Maier, “Decoupling absorption and emission processes in super-resolution localization of emitters in a plasmonic hotspot,” *Nature Communications*, vol. 8, pp. 14513–14522, 2017.

[98] K. L. Blythe and K. A. Willets, "Super-Resolution Imaging of Fluorophore-Labeled DNA Bound to Gold Nanoparticles: A Single Molecule, Single Particle Approach," *Journal of Physical Chemistry C*, vol. 120, no. 2, pp. 803–815, 2016.

[99] K. Lim, C. Ropp, S. Barik, J. T. Fourkas, B. Shapiro, and E. Waks, "Nanostructure-induced distortion in single-emitter microscopy," *Nano Letters*, vol. 16, no. 9, pp. 5415–5419, 2016.

[100] C. Ropp, Z. Cummins, S. Nah, J. T. Fourkas, B. Shapiro, and E. Waks, "Nanoscale probing of image-dipole interactions in a metallic nanostructure," *Nature Communications*, vol. 6, pp. 6558–6565, 2015.

[101] J. D. Flynn, B. L. Haas, and J. S. Biteen, "Plasmon-Enhanced Fluorescence from Single Proteins in Living Bacteria," *Journal of Physical Chemistry C*, vol. 120, no. 37, pp. 20512–20517, 2016.

[102] J. W. Lichtman and J.-A. Conchello, "Fluorescence microscopy," *Nature Methods*, vol. 2, no. 12, pp. 910–919, 2005.

[103] B. Huang, M. Bates, and X. Zhuang, "Super-resolution fluorescence microscopy," *Annual Review of Biochemistry*, vol. 78, pp. 993–1016, 2009.

[104] A. Pertsinidis, Y. Zhang, and S. Chu, "Subnanometre single-molecule localization, registration and distance measurements," *Nature*, vol. 466, no. 7306, pp. 647–651, 2010.

[105] F. Tam, G. P. Goodrich, B. R. Johnson, and N. J. Halas, "Plasmonic enhancement of molecular fluorescence.," *Nano Letters*, vol. 7, no. 2, pp. 496–501, 2007.

[106] A. M. Gabudean, M. Focsan, and S. Astilean, "Gold Nanorods Performing as Dual-Modal Nanoprobes via Metal-Enhanced Fluorescence (MEF) and Surface-Enhanced Raman Scattering (SERS)," *Journal of Physical Chemistry C*, vol. 116, no. 22, pp. 12240–12249, 2012.

[107] D. Darvill, A. Centeno, and F. Xie, "Plasmonic fluorescence enhancement by metal nanostructures: shaping the future of bionanotechnology.," *Physical Chemistry Chemical Physics*, vol. 15, no. 38, pp. 15709–15726, 2013.

[108] J. Olson, S. Dominguez-Medina, A. Hoggard, L.-Y. Wang, W.-S. Chang, and S. Link, "Optical characterization of single plasmonic nanoparticles," *Chemical Society Reviews*, vol. 44, pp. 40–57, 2015.

[109] A. Kinkhabwala, Z. Yu, S. Fan, Y. Avlasevich, K. Müllen, and W. E. Moerner, "Large single-molecule fluorescence enhancements produced by a bowtie nanoantenna," *Nature Photonics*, vol. 3, no. 11, pp. 654–657, 2009.

[110] R. Bardhan, N. K. Grady, J. R. Cole, A. Joshi, and N. J. Halas, "Fluorescence Enhancement by Au:Nanoshells and Nanorods," *ACS Nano*, vol. 3, no. 3, pp. 744–752, 2009.

[111] S. Baldelli, A. S. Eppler, E. Anderson, Y. R. Shen, and G. A. Somorjai, "Surface enhanced sum frequency generation of carbon monoxide adsorbed on platinum nanoparticle arrays," *Journal of Chemical Physics*, vol. 113, no. 2000, pp. 5432–5438, 2000.

[112] I. Zorić, M. Zäch, B. Kasemo, and C. Langhammer, "Gold, platinum, and aluminum nanodisk plasmons: Material independence, subradiance, and damping mechanisms," *ACS Nano*, vol. 5, no. 4, pp. 2535–2546, 2011.

[113] H. Cang, A. Labno, C. Lu, X. Yin, M. Liu, C. Gladden, Y. Liu, and X. Zhang, "Probing the electromagnetic field of a 15-nanometre hotspot by single molecule imaging," *Nature*, vol. 469, no. 7330, pp. 385–8, 2011.

[114] R. Chhabra, J. Sharma, H. Wang, S. Zou, S. Lin, H. Yan, S. Lindsay, and Y. Liu, "Distance-dependent interactions between gold nanoparticles and fluorescent molecules with DNA as tunable spacers," *Nanotechnology*, vol. 20, no. 48, pp. 485201–485210, 2009.

[115] C. Greulich, D. Braun, A. Peetsch, J. Diendorf, B. Siebers, M. Epple, and M. Köller, "The toxic effect of silver ions and silver nanoparticles towards bacteria and human cells occurs in the same concentration range," *RSC Advances*, vol. 2, no. 17, pp. 6981–6987, 2012.

[116] A. M. Alkilany and C. J. Murphy, "Toxicity and cellular uptake of gold nanoparticles: what we have learned so far?," *Journal of Nanoparticle Research*, vol. 12, no. 7, pp. 2313–2333, 2010.

[117] J. E. Donehue, B. L. Haas, E. Wertz, C. N. Talicska, and J. S. Biteen, "Plasmon-enhanced emission from single fluorescent proteins," *SPIE Proceedings*, vol. 8597, p. 85970J, 2013.

[118] P. Anger, P. Bharadwaj, and L. Novotny, "Enhancement and Quenching of Single-Molecule Fluorescence," *Physical Review Letters*, vol. 96, no. 11, p. 113002, 2006.

[119] J. S. Biteen, D. Pacifici, N. S. Lewis, and H. A. Atwater, "Enhanced radiative emission rate and quantum efficiency in coupled silicon nanocrystal-nanostructured gold emitters," *Nano Letters*, vol. 5, no. 9, pp. 1768–1773, 2005.

[120] O. Kulakovich, N. Strekal, A. Yaroshevich, S. Maskevich, S. Gaponenko, I. Nabiev, U. Woggon, and M. Artemyev, “Enhanced Luminescence of CdSe Quantum Dots on Gold Colloids,” *Nano Letters*, vol. 2, no. 12, pp. 1449–1452, 2002.

[121] G. Schneider, G. Decher, N. Nerambourg, R. Praho, M. H. V. Werts, and M. Blanchard-Desce, “Distance-dependent fluorescence quenching on gold nanoparticles ensheathed with layer-by-layer assembled polyelectrolytes,” *Nano letters*, vol. 6, no. 3, pp. 530–536, 2006.

[122] C. Wang, W. Zhu, Y. Lan, M. Zhang, T. Tian, H. Wang, and G. Li, “Facile fabrication of reactive plasmonic substrates for fluorescence enhancement via mussel-inspired chemistry,” *Journal of Physical Chemistry C*, vol. 118, no. 20, pp. 10754–10763, 2014.

[123] G. P. Acuna, M. Bucher, I. H. Stein, C. Steinhauer, A. Kuzyk, P. Holzmeister, R. Schreiber, A. Moroz, F. D. Stefani, T. Liedl, F. C. Simmel, and P. Tinnefeld, “Distance dependence of single-fluorophore quenching by gold nanoparticles studied on DNA origami,” *ACS Nano*, vol. 6, no. 4, pp. 3189–3195, 2012.

[124] P. Reineck, D. Gomez, S. H. Ng, M. Karg, T. Bell, P. Mulvaney, and U. Bach, “Distance and wavelength dependent quenching of molecular fluorescence by Au@SiO2 core-shell nanoparticles,” *ACS Nano*, vol. 7, pp. 6636–6648, 2013.

[125] S. Pal, P. Dutta, H. Wang, Z. Deng, S. Zou, H. Yan, and Y. Liu, “Quantum Efficiency Modification of Organic Fluorophores Using Gold Nanoparticles on DNA Origami Scaffolds,” *Journal of Physical Chemistry C*, vol. 117, pp. 12735–12744, 2013.

[126] J. Seelig, K. Leslie, A. Renn, S. Kühn, V. Jacobsen, M. van de Corput, C. Wyman, and V. Sandoghdar, “Nanoparticle-induced fluorescence lifetime modification as nanoscopic ruler: demonstration at the single molecule level.,” *Nano Letters*, vol. 7, no. 3, pp. 685–689, 2007.

[127] P. A. Chiarelli, “Polyelectrolyte spin-assembly,” *Langmuir*, vol. 18, no. 18, pp. 168–173, 2002.

[128] J. Huang, J. Park, W. Wang, C. J. Murphy, and D. G. Cahill, “Ultrafast Thermal Analysis of Surface Functionalized Gold Nanorods in Aqueous Solution,” *ACS Nano*, vol. 7, no. 1, pp. 589–597, 2013.

[129] J. S. Biteen, M. A. Thompson, N. K. Tselentis, G. R. Bowman, L. Shapiro, and W. E. Moerner, “Super-resolution imaging in live Caulobacter crescentus cells using photoswitchable EYFP.,” *Nature Methods*, vol. 5, no. 11, pp. 947–949, 2008.

[130] P. Johnson and R. Christy, "Optical Constants of the Noble Metals," *Physical Review B*, vol. 6, pp. 4370–4379, 1972.

[131] E. D. Palik, *Handbook of Optical Constants of Solids.* Academic Press: London, U.K., 1998.

[132] M. Hu, C. Novo, A. Funston, H. Wang, H. Staleva, S. Zou, P. Mulvaney, Y. Xia, and G. V. Hartland, "Dark-field microscopy studies of single metal nanoparticles: understanding the factors that influence the linewidth of the localized surface plasmon resonance," *Journal of Materials Chemistry*, vol. 18, no. 17, pp. 1949–1960, 2008.

[133] Y. Chen, K. Munechika, and D. S. Ginger, "Dependence of fluorescence intensity on the spectral overlap between fluorophores and plasmon resonant single silver nanoparticles," *Nano Letters*, vol. 7, no. 3, pp. 690–696, 2007.

[134] N. S. Abadeer, M. R. Brennan, W. L. Wilson, and C. J. Murphy, "Distance and Plasmon Wavelength Dependent Fluorescence of Molecules Bound to Silica-Coated Gold Nanorods," *ACS Nano*, vol. 8, no. 8, pp. 8392–8406, 2014.

[135] S. Kühn, U. Håkanson, L. Rogobete, and V. Sandoghdar, "Enhancement of single-molecule fluorescence using a gold nanoparticle as an optical nanoantenna," *Physical Review Letters*, vol. 97, no. 1, pp. 1–4, 2006.

[136] C. B. Müller, A. Loman, V. Pacheco, F. Koberling, D. Willbold, W. Richtering, and J. Enderlein, "Precise measurement of diffusion by multi-color dual-focus fluorescence correlation spectroscopy," *EPL (Europhysics Letters)*, vol. 83, no. 4, p. 46001, 2008.

[137] S. R. Meech, "Excited state reactions in fluorescent proteins," *Chemical Society Reviews*, vol. 38, no. 10, pp. 2922–2934, 2009.

[138] N. C. Shaner, R. E. Campbell, P. a. Steinbach, B. N. G. Giepmans, A. E. Palmer, and R. Y. Tsien, "Improved monomeric red, orange and yellow fluorescent proteins derived from Discosoma sp. red fluorescent protein," *Nature Biotechnology*, vol. 22, no. 12, pp. 1567–1572, 2004.

[139] B. Seefeldt, R. Kasper, T. Seidel, P. Tinnefeld, K.-J. Dietz, M. Heilemann, and M. Sauer, "Fluorescent proteins for single-molecule fluorescence applications," *Journal of Biophotonics*, vol. 1, no. 1, pp. 74–82, 2008.

[140] K. Xu, G. Zhong, and X. Zhuang, "Actin, spectrin, and associated proteins form a periodic cytoskeletal structure in axons.," *Science*, vol. 339, no. 6118, pp. 452–456, 2013.

[141] D. R. Whelan and T. D. M. Bell, "Super-resolution single-molecule localization microscopy: tricks of the trade," *Journal of Physical Chemistry Letters*, vol. 6, pp. 374–382, 2015.

[142] P. Dedecker, F. C. De Schryver, and J. Hofkens, "Fluorescent proteins: shine on, you crazy diamond," *Journal of the American Chemical Society*, vol. 135, no. 7, pp. 2387–2402, 2013.

[143] I. Gorelikov and N. Matsuura, "Single-step coating of mesoporous silica on cetyltrimethyl ammonium bromide-capped nanoparticles," *Nano letters*, vol. 8, no. 1, pp. 369–373, 2008.

[144] T. K. Sau and C. J. Murphy, "Room Temperature, High-Yield Synthesis of Multiple Shapes of Gold Nanoparticles in Aqueous Solution," *Journal of the American Chemical Society*, vol. 126, no. 28, pp. 8648–8649, 2004.

[145] M. Howarth, D. J.-f. Chinnapen, K. Gerrow, P. C. Dorrestein, M. R. Grandy, N. L. Kelleher, A. El-husseini, and A. Y. Ting, "A monovalent streptavidin with a single femtomolar biotin binding site," *Nature Methods*, vol. 3, no. 4, pp. 267–274, 2006.

[146] F. V. Subach, G. H. Patterson, S. Manley, J. M. Gillette, J. Lippincott-Schwartz, and V. V. Verkhusha, "Photoactivatable mCherry for high-resolution two-color fluorescence microscopy," *Nature Methods*, vol. 6, pp. 153–9, feb 2009.

[147] D. G. Gibson, L. Young, R.-y. Chuang, J. C. Venter, C. A. H. Iii, H. O. Smith, and N. America, "Enzymatic assembly of DNA molecules up to several hundred kilobases," *Nature Methods*, vol. 6, no. 5, pp. 343–347, 2009.

[148] G. H. Patterson and J. Lippincott-Schwartz, "A photoactivatable GFP for selective photolabeling of proteins and cells," *Science*, vol. 297, pp. 1873–7, sep 2002.

[149] M. Howarth and A. Ting, "Monovalent streptavidin expression and purification," *Protocol Exchange*, vol. 9, mar 2008.

[150] N. S. Abadeer, G. Fülöp, S. Chen, M. Käll, and C. J. Murphy, "Interactions of Bacterial Lipopolysaccharides with Gold Nanorod Surfaces Investigated by Refractometric Sensing," *ACS Applied Materials and Interfaces*, vol. 7, no. 44, pp. 24915–24925, 2015.

[151] L. Kisley, R. Brunetti, L. J. Tauzin, B. Shuang, X. Yi, A. W. Kirkeminde, D. A. Higgins, S. Weiss, and C. F. Landes, "Characterization of Porous Materials by Fluorescence Correlation Spectroscopy Super-resolution Optical Fluctuation Imaging," *ACS Nano*, vol. 9, no. 9, pp. 9158–9166, 2015.

[152] K. Aslan, M. Wu, J. R. Lakowicz, and C. D. Geddes, "Fluorescent core-shell Ag@SiO2 nanocomposites for metal-enhanced fluorescence and single nanoparticle sensing platforms," *Journal of the American Chemical Society*, vol. 129, no. 6, pp. 1524–1525, 2007.

[153] S. D. Standridge, G. C. Schatz, and J. T. Hupp, "Distance dependence of plasmon-enhanced photocurrent in dye-sensitized solar cells," *Journal of the American Chemical Society*, vol. 131, no. 24, pp. 8407–8409, 2009.

[154] E. Johlin, J. Solari, S. A. Mann, J. Wang, T. S. Shimizu, and E. C. Garnett, "Super-resolution imaging of light-matter interactions near single semiconductor nanowires," *Nature Communications*, vol. 7, pp. 13950–13955, 2016.

[155] S. van de Linde, A. Lschberger, T. Klein, M. Heidbreder, S. Wolter, M. Heilemann, and M. Sauer, "Direct stochastic optical reconstruction microscopy with standard fluorescent probes," *Nature Protocols*, vol. 6, no. 7, pp. 991–1009, 2011.

[156] J. Vogelsang, T. Cordes, C. Forthmann, C. Steinhauer, and P. Tinnefeld, "Controlling the fluorescence of ordinary oxazine dyes for single-molecule switching and superresolution microscopy.," *Proceedings of the National Academy of Sciences*, vol. 106, no. 20, pp. 8107–8112, 2009.

[157] K. L. Blythe, E. J. Titus, and K. A. Willets, "Triplet-state-mediated super-resolution imaging of fluorophore-labeled gold nanorods.," *ChemPhysChem*, vol. 15, no. 4, pp. 784–793, 2014.

[158] S. J. Hurst, A. K. R. Lytton-Jean, and C. A. Mirkin, "Maximizing DNA loading on a range of gold nanoparticle sizes.," *Analytical Chemistry*, vol. 78, no. 24, pp. 8313–8318, 2006.

[159] J.-h. Oh, D. H. Park, J. H. Joo, and J.-s. Lee, "Recent advances in chemical functionalization of nanoparticles with biomolecules for analytical applications," *Analytical and Bioanalytical Chemistry*, vol. 407, pp. 8627–8645, 2015.

[160] T. Taton, *Current Protocols in Nucleic Acid Chemistry.* John Wiley Sons, Inc., 2002.

[161] B. Huang, W. Wang, M. Bates, and X. Zhuang, "Three-dimensional super-resolution imaging by stochastic optical reconstruction microscopy.," *Science*, vol. 319, no. 5864, pp. 810–813, 2008.

[162] M. Ringler, A. Schwemer, M. Wunderlich, A. Nichtl, K. Kürzinger, T. Klar, and J. Feldmann, "Shaping Emission Spectra of Fluorescent Molecules with Single Plasmonic Nanoresonators," *Physical Review Letters*, vol. 100, p. 203002, may 2008.

[163] J. Record, M. T., S. J. Mazur, P. Melancon, J.-H. Roe, S. L. Shaner, and L. Unger, “Double helical DNA: conformations, physical properties, and interactions with ligands,” *Annual Review of Biochemistry*, vol. 50, pp. 997–1024, 1981.

[164] B. Shuang, D. Cooper, J. N. Taylor, L. Kisley, J. Chen, W. Wang, C. B. Li, T. Komatsuzaki, and C. F. Landes, “Fast Step Transition and State Identification (STaSI) for Discrete Single-Molecule Data Analysis,” *Journal of Physical Chemistry C*, vol. 5, pp. 3157–3161, 2014.

[165] A. Kinkhabwala, Z. Yu, S. Fan, Y. Avlasevich, K. Müllen, and W. E. Moerner, “Large single-molecule fluorescence enhancements produced by a bowtie nanoantenna,” *Nature Photonics*, vol. 3, no. 11, pp. 654–657, 2009.

[166] R. Chikkaraddy, B. D. Nijs, F. Benz, S. J. Barrow, O. A. Scherman, and P. Fox, “Single-molecule strong coupling at room temperature in plasmonic nanocavities,” *Nature*, vol. 535, no. 7610, pp. 127–130, 2016.

[167] K. G. Stamplecoskie and P. V. Kamat, “Synergistic Effects in the Coupling of Plasmon Resonance of Metal Nanoparticles with Excited Gold Clusters,” *The Journal of Physical Chemistry Letters*, vol. 6, pp. 1870–1875, 2015.